Analysis and optimization of thermoplastic fuselage struts under crashworthiness requirements

G. Rosado Bailón

Faculty of Aerospace Engineering
Delft University of Technology

Master of Science Thesis

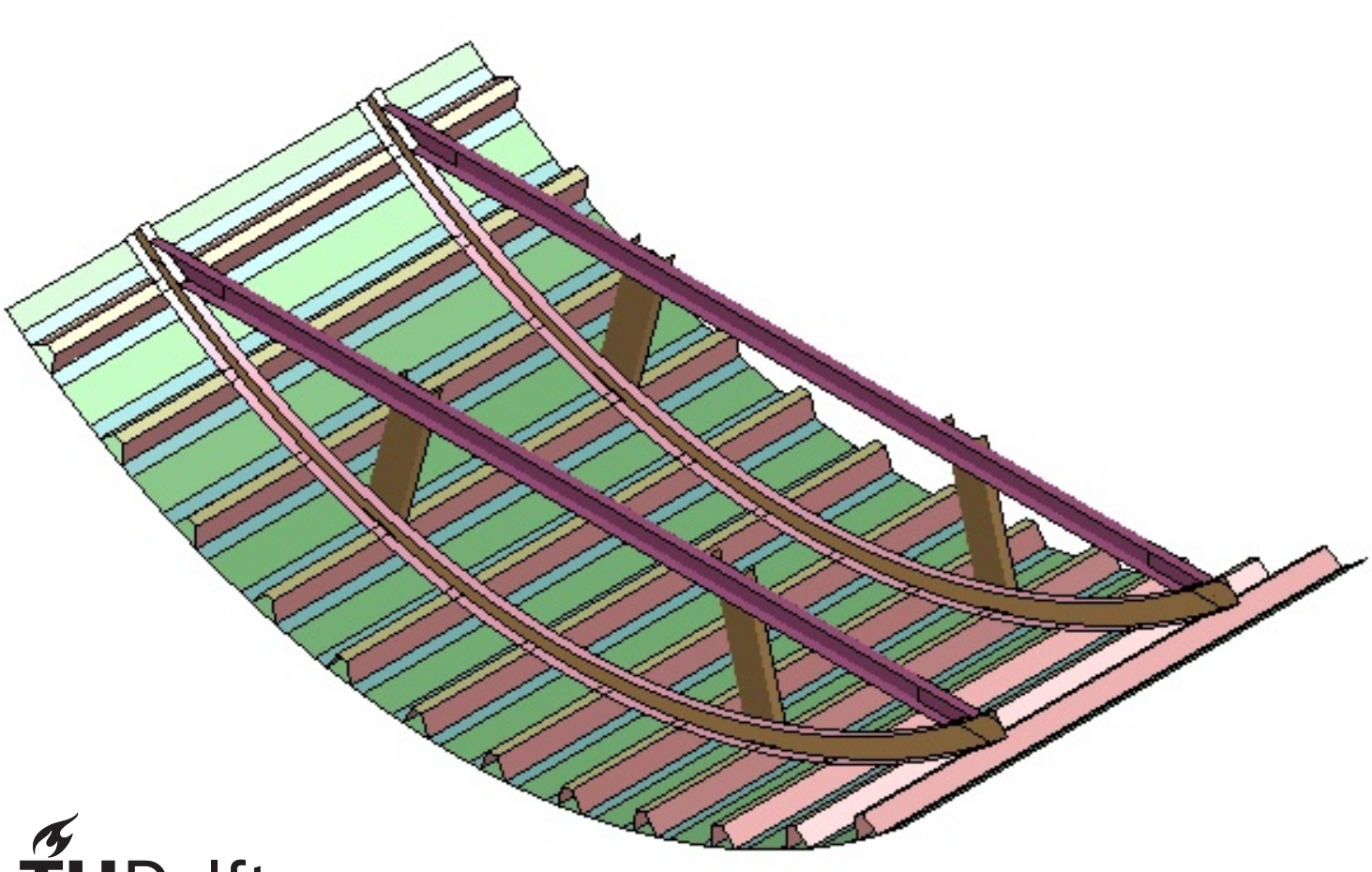

TU Delft

Analysis and optimization of thermoplastic fuselage struts under crashworthiness requirements

by

G. Rosado Bailón

to obtain the degree of Master of Science
at the Delft University of Technology,
to be defended publicly on Friday May 20^{th}, 2022 at 9:30 AM.

Student number:	5135990	
Project duration:	October 5^{th}, 2020 – May 20^{th}, 2022	
Graduation committee:	Prof. Dr. C. Bisagni,	TU Delft ASM-ASCM, Chair holder and supervisor
	Dr. S.R. Turteltaub,	TU Delft ASM-ASCM, Examiner
	Dr. C.D. Rans,	TU Delft ASM-SI&C, Examiner
	Dr. J. Paz Mendez,	TU Delft ASM-ASCM, Additional

This thesis is supported by Clean Sky 2 STUNNING project.

TU Delft

Clean Sky

Acknowledgements

Firstly, I want to thank my supervisor, professor Chiara Bisagni for this opportunity to collaborate with Fokker on the Clean Sky 2 STUNNING project. This topic has a lot of potential for future applications in aeronautics, I just could not resist jumping in and learning from it. It is an honor to work on the STUNNING fuselage model and I am grateful for my supervisor to trust me with this topic. I also want to thank Javier Paz Mendez, as together with professor Bisagni, they have guided me throughout this thesis and I want to thank them both for their patience, help, and feedback this past year. I shall too give special recognition to my colleagues from professor Bisagni's research group for their help and insights. In particular, I want to thank my former colleagues Victor Poorte and Yu Qian Tu. At the beginning of the thesis, when getting used to LS-DYNA's usage to model composite simulations, they both helped me solve the doubts I had when modeling the numerical analyses. I thank them for taking the time to help me whilst they had a lot of work of their own.

This may sound too generic, but I do want to thank everyone I have met at TU Delft since the beginning of my master's. I did not have a strong structures background when I started my master's, and my classmates, professors, and teaching assistants I have come across have made this thesis possible. In almost three years I have learned many new things, which has allowed me to work on a topic I enjoy like this one, I could not have taken this challenge without them otherwise. Here I also shall give a special thank you to the amazing friends I made from the ASM master. They have been my main support in my past two years here in the Netherlands, and despite not seeing each other as much since the beginning of the COVID-19 pandemic, we managed to keep in touch and support each other throughout the distance. My biggest gratitude to my friend Palak Singh for her special support throughout this thesis, the long calls, video chats, and the days spent at *cofee company* working on our respective theses. It has been hard to be as productive with a pandemic going on, so we managed to push each other to work more efficiently and take breaks when needed to make this process easier. In time, I have learned that despite all the challenges I have faced these past few years personally and professionally, taking a break is far more important than what I imagined at first. And this is in part thanks to my support system here in the Netherlands.

And last but not least, I want to thank my family and friends from back home as well for their unconditional love, patience, and understanding. This year brought upon us surgeries, losses of family members, and challenging situations that have made the task of working on the thesis much harder. It is because of my family and friends that I got through it, so they deserve all the recognition they can get. I want to thank in particular my parents for always believing in me and for helping me become an aerospace engineer, just like I always wanted. Everything I have studied, and everything I will do in my life professionally, I owe it to them. So thank you for making this possible, I love you dearly.

G. Rosado Bailón
Delft & Haarlem, May 2022

Contents

List of Figures

List of Tables

Nomenclature

Numeric and Latin alphabet

A_0	Plate cross-section initial area, prior to deformation
A350	Airbus aircraft model 350
ANN	Artificial Neuronal Networks
B737-200	Boeing aircraft model 737, series 200
B787	Boeing aircraft model 787
BPNN	Back-Propagation Neural Network
CFE	Crush Force Efficiency
CFRP	Carbon Fiber Reinforced Plastics
CLE	Crush Load Efficiency
CLPT	Classical Laminate Plate Theory
CNT	Carbon nano-tubes
CPACS	Common Parametric Aircraft Configuration Schema
CPU	Central Processing Unit
CZM	Cohesive Zone Method
E	Young's modulus (metals)
E_A	Longitudinal Young's modulus (local coordinates, composites)
EA	Total energy absorbed
EASA	European Union Aviation Safety Agency
E_B	Transverse Young's modulus (local coordinates, composites)
E-glass, E-GRFP	Glass Fiber Reinforced Plastic for initial Alkaline free Electrical applications
EGO	Efficient Global Optimization strategy
EPS, ERODS	Effective failure strain
E_x	Principal Young's modulus (global coordinates, composites)
E_y	Transverse Young's modulus (global coordinates, composites)
FAA	Federal Aviation Administration
FBRT	Reduction factor for tensile loading
FEA	Finite Element Analysis

FEM Finite Element Model

FFNN Feed-forward neural network

F_{mean} Mean or average axial crushing force

F_{peak} Peak or maximal axial crushing force

$F(x)$ Instantaneous crushing load

GA Genetic Algorithm

G_{AB}, G_{CA} Longitudinal Shear modulus (composites)

G_{BC} Transverse Shear modulus (composites)

GFRP Glass Fiber Reinforced Plastics

GMS Maximum shear strain

hpc High performance computing cluster

IIHS Insurance Institute for Highway Safety

L_0 Initial length of the plate in the loading direction

$L_{crushed}$ Crushed length

LHS Hypercube sampling point-selection method

LRS Limit of Reasonable Survivability

$mass_{abs}$ Absorbing mass or mass under deformation

MOPSO Multi-Objective Particle Swarm Optimisation

MPL Multi-layer perceptrons

MSE Mean squared error

NDT Non-Destructive Techniques

N_{plies} Number of plies in a plate/laminate

NSGA-II Elitist Non-Dominated Sorting Genetic Algorithm

ORNL Oak Ridge National Laboratory

PEEK Polyetherether ketone

PFL Percentage of plies to fail

POF Pareto Optimal Frontier or Pareto front

pX X^{th} ply orientation

R Hardening parameter

R^2 Coefficient of multiple determination

RBF NN Radial-based neural network

RMS Root mean squared error

S&G Sprague and Geers

S_C Shear strength

SC Special Condition

SE Stroke Efficiency

SEA Specific Energy Absorption

S-GRFP Glass Fiber Reinforced Plastic for Strength applications

SI International System of Units

SLIMC1 Longitudinal compression loading limit factor

SLIMC2 Transverse compression loading limit factor

SLIMS Shear loading limit factor

SLIMT1 Longitudinal tensile loading limit factor

SLIMT2 Transverse tensile loading limit factor

SOFT Softening reduction

SQP Sequential Quadratic Programming

SQRT PRESS Root metric of the residual prediction accuracy

t, T Thickness

TFAIL,TSIZE Element erosion time-step limit

t_{plate} Plate's total thickness

t_{ply} Ply thickness

UD Unidirectional (fibers)

x Stroke length

X_C Longitudinal compression strength

X_T Longitudinal tensile strength

Y_C Transverse compression strength

YCFAC Reduction factor for compression loading

Y_T Transverse tensile strength

Greek alphabet and symbols

Δ Difference or improvement

ε Strain

$\varepsilon_{11,C}$ Maximum longitudinal compression strain

$\varepsilon_{11,T}$ Maximum longitudinal tensile strain

$\varepsilon_{22,C}$ Maximum transverse compression strain

$\varepsilon_{22,T}$ Maximum transverse tensile strain

µGA Micro-Genetic Algorithm

ν Poisson's ratio (metals)

ν_{AB} Longitudinal Poisson's ratio (composites)

ν_{BA}	Transverse Poisson's ratio (composites)
ρ	Material's density
σ	Stress
σ_y	Yield stress

Abstract

The safety of a commercial aircraft is a factor to consider from the early stages of its design to guarantee that this one's structure can protect the occupants inside in a low-speed crash. In an aircraft's primary structure such as a fuselage, where the occupants and cargo should be protected, the design regulations imposed by the European Union Aviation Safety Agency (EASA) have been applied for decades to conventional metallic designs. These designs had aluminum as the main constituent for being a lightweight material. Nevertheless, this project improves a component's design from a fully thermoplastic fuselage. While two commercial aircraft (Airbus model 350 or A350, and Boeing model 787, or B787) have already implemented some composite parts in their design to aim for sustainable and lightweight components, thermosets were the composites used in primary structures mainly. Composite materials do not present the plasticity metals do, which means that the regulations from EASA can no longer apply in the A350 and B787 hybrid designs. With the introduction of composite materials in these aircraft, organizations like the Federal Aviation Administration (FAA) and EASA had to write some new guidelines for these aircraft structures. These enable the protection of the passengers and cargo from the loads exerted on the aircraft during a survivable crash. Therefore, the new regulations are the ones taken into account for this thesis project, since these can be applied to similar composite structural designs, such as the fully thermoplastic fuselage section, whose numerical model is inherited from the Clean Sky STUNNING project.

What is wanted for the fuselage section's crashworthiness is for its structure to absorb as much energy as possible from the crash. All while minimizing the peaks of force that this one experiences. That way, the loads that arrive at the cabin of the aircraft are reduced and the structure becomes safer for a low-speed crash of under 30 ft/s (about 10 m/s), meaning that the passengers inside have a higher chance of survival and it is less probable they suffer from severe injuries. That is the aim of this project while focusing only on the structure's behavior.

The struts of the fuselage (or energy absorbers) are the components whose design is modified to generate the desired design behavior in the fuselage section: higher energy absorption and lower peaks exerted in the structure. To do so, several numerical analyses are done in LS-DYNA, and each of them increases in difficulty in each stage of the research, until reaching the crushing of the STUNNING fuselage. The initial exercise consists of aluminum and composite plates, which introduce the formulation of the following crushing tube exercise. It is after the optimization of the tube's layup, that this one is introduced in the STUNNING fuselage energy absorbers. In the fuselage analysis, the struts (or energy absorbers) keep the square geometry cross-section from the tube exercise, as well as the optimized layup. However, these are changed in size. These change and their new layup further increase the crashworthiness and safety of both the struts and the entire fuselage section in ideal low-speed crash conditions. These ideal conditions include neglecting the payload mass of the passengers' cargo in the fuselage section, and not considering the upper part of the fuselage airframe that is missing in the section's model. That is why, after the fuselage design for the energy absorbers is improved and set as final in terms of crashworthiness, a more realistic setup is modeled with a simplified payload mass on top of the fuselage section. This payload mass simulates the mass of the six passengers' suitcases that fit into the fuselage's section. This change in conditions for the crushing analysis of the fuselage is enough to prove how different the structure behaves from the initial scenario, lowering the total energy absorbed and increasing the peak force. Due to this change in crash kinematics behavior, this project concludes that in future studies, the fuselage section should consider distancing the payload mass from the structure to avoid initial penetration in the nodes of the model. In addition to this, more accurate models including the missing upper part of the fuselage and the passengers' mass on the cabin floor should be studied. These could provide more representative results when predicting how good the fuselage is in terms of crashworthiness.

Chapter 1

Introduction

Air transport is about 50 times safer than automobile vehicle transportation due to its low rate of fatal accidents [1]. Despite this, whenever there is an aircraft crash, the media puts this one in the spotlight for days, and even weeks, which does not happen in car crashes. This might be because airplanes travel at faster speeds than automobiles, which makes the crash deadlier, and due to their higher capacity, more people are affected at once. However, there are some cases in which air crashes can be considered survivable, and aircraft must be designed to prevent their passengers or cargo to get strongly affected by these [2]. Therefore, the study on how primary parts of an aircraft behave upon crushing at low speeds, considered survivable, is required when designing a new plane concept like a hybrid metal-composite aircraft. In this project, the crushing behavior of the STUNNING fuselage section is studied in a survivable crash scenario. This fuselage section is inherited from the Clean Sky 2 STUNNING project and continues part of the fuselage's crashworthiness study from Poorte's thesis through LS-DYNA numerical analyses [3, 4, 5]. These analyses of vehicles' structures in crash applications have to meet certain conditions to evaluate how crashworthy these are.

The term crashworthiness (or having a crashworthy behavior) is the ability of a vehicle's structure to keep its occupants from getting severe injuries or death in crash conditions. In spite of focusing on the aeronautics sector in this thesis to evaluate the STUNNING fuselage behavior [3, 5], the crashworthiness requirements can be of relevance to any other kind of transport vehicle like a car, a train, or a bus. A fuselage structure can crash either on a rigid ground or a water surface. The last one, however, degrades the fuselage materials' properties considerably [6], which changes the crash behavior of the aircraft. This is particularly troubling for the STUNNING fuselage, which is mainly made of Toray Cetex TC1225 thermoplastic composite and can be easily affected by moisture. That is why coatings are usually used for these composites, to protect them from humidity exposure. Regarding the crushing conditions, aircraft passengers' injuries can be prevented through passive safety use to minimize the crushing loads reaching the cabin [7]. A structure can do that by absorbing the kinetic energy of the impact through deformation. The entire STUNNING fuselage section is not studied so the focus of this thesis resides on the analysis and improvement of its struts' design alone. Also known as energy absorbers. Because these are made from thermoplastic composites, the struts deform differently than other conventional designs. Hence, this topic evaluates how these make the primary structure behave under crash requirements.

The trend for the past few decades has been to use materials on aircraft (and other vehicles) that are more lightweight yet sustainable. The aircraft design of reference for the previous statement is what is called "the conventional design", which is made of metals. Usually, aluminum is the main component to guarantee the lightweight requirement to fly. To further minimize the weight while keeping the desired mechanical properties, composites are implemented. Composites are considered to be sustainable materials that provide great specific properties while reducing the weight of the structure, in comparison with the conventional design. Consequently, fuel consumption is reduced alongside emissions. So the outcome complies with the sustainable requirement and brings along other advantages when changing metallic to composite structures: higher tailorability and do not suffer from corrosion as aluminum does. The introduction of composites to the aeronautics sector is not recent though. Commercial aircraft like B787 and A350 have already introduced the concept of metallic-composite hybrid structures where composites are used in primary structures like the fuselage itself. However, no regulations for the crashworthiness of these composite structures exist yet

as they do for metals. Hence, there is the need to adapt the existing ones to the newest design features. The composites used in the B747 and A350 aircraft are made of carbon fibers with thermoset epoxy resin due to the high properties this combination offers. While these structures can be used as a reference for their composite crashworthiness conditions, this project's structure uses thermoplastic resins instead. These are used in the automotive industry and space but not yet in aeronautics, due to the different properties these provide with respect to thermosets. Thermoplastic resins have thermal sensitivity as a differential property, which changes their physical state with temperature, allowing them to work on higher temperature ranges than thermosets. That is why thermoplastic composites are also used as thermal resistance covers in space vehicles. Temperature sensitivity also allows for a faster and cheaper manufacturing process, the recyclability of this material, the lower molecular weight that helps to enhance impact toughness, and the possibility to reduce joint weight by using welding between thermoplastic matrices of the same type. These cannot happen in an epoxy composite, because thermosets cannot be melted or reshaped after curing [7]. They can only deteriorate with heat, so they need adhesive bonds or fasteners to assemble parts.

1.1 Goals and Methodology

The goal of this thesis is to generate a methodology that aids to find a strut configuration that improves the crashworthiness behavior of the fuselage from the Clean Sky 2 STUNNING project [3, 4, 5]. First, an analysis of the STUNNING fuselage crushing simulation is performed, and then the change of strut geometry, size, and stacking sequence will lead us to an optimal fuselage behavior for a survivable crash condition. Nonetheless, this project increases the structural complexity progressively, which is why the six core chapters are structured to show the work escalating from one chapter to the next until accomplishing the thesis goal.

At first, it is important to define what crashworthiness behavior means and what is wanted in a structure to have good crashworthy behavior. That is why Chapter 2 explains the state-of-the-art of the crashworthiness concept and its application to structures. More concretely, the chapter explains the regulations the aeronautics sector has for this term, and how composite structures are introduced into the field. Understanding this is important for the rest of the thesis, given that the STUNNING fuselage is primarily made of thermoplastic composite materials. Since this material has not been introduced in aircraft primary structures, this topic's novelty requires further knowledge on thermoplastic behavior under crash conditions. Hence, automotive thermoplastic structures are also presented for crashworthiness purposes in Chapter 2 to see which regulations they follow and how these composite structures behave in comparison with conventional metal structures.

Once the state-of-the-art is presented and it is stated what to look for in crushing analyses, the tool used to model these is LS-DYNA, which presents a more accurate crushing environment for these simulations than other software like Abaqus. Hence the complexity of the work escalates in each chapter, starting with simpler exercises to practice finite element modeling. Chapter 3 starts with basic tensile analyses for aluminum and composite plates. The exercise aims to use the finite element model in LS-DYNA and get familiar with the environment and its keywords since this one does not work as graphically intuitively as Abaqus and requires the support of its keyword manuals [8, 9]. This first exercise also introduces the composite modeling in the new software, which is applied to the following chapters. After the plates' tests, Chapter 4 introduces the composite crushing scenario by using a simple tube structure with a bevel on its top. This analysis introduces already a 3D model that does not require as much computation time as the fuselage, so it is good to learn how to set up and simulate crushing conditions. Only after this is modeled successfully and compared to models of reference [10, 11], the stacking sequence is optimized in Chapter 5 using LS-OPT. Despite being familiar with optimization algorithms, the graphical interface of LS-OPT links the optimization to the LS-DYNA analysis input file to generate sampled models from it, build a metamodel and generate optimized stacking sequences. While Chapter 5 presents a simple optimization for the tube for crashworthiness purposes without changing the number of plies, after several setbacks, this optimization procedure cannot be extrapolated to the fuselage due to this computational cost and the limited time available to complete the thesis. In the end, the optimized tube from Chapter 5 is introduced into the STUNNING fuselage by the end of Chapter 6 using square struts, and its resulting crashworthiness metrics are evaluated. As a consequence, the plan for the last chapter modifies the size of the struts to see which effect this has on the crashworthiness metrics of the fuselage for the best crushing struts cross-section. These are the energy absorbed, and the peak and

mean forces. Instead of using an optimization tool for this purpose, Chapter 7 presents a parametrical study that introduces new square strut sizes in twelve different LS-DYNA numerical simulations. Thankfully, this is possible because of all the skills learned in previous work from the analyses chapters (Chapter 3, Chapter 4 and Chapter 6), which have made it easier to understand the crushing of the fuselage, how the inherited STUNNING model has been made and how this one can be modified.

Figure 1.1 shows how the different chapters are linked to each other, being Chapter 2 the base of the entire project as it explains the basic concepts that are applied in other stages of the thesis. This one is only drawn at the beginning to symbolize the accumulative knowledge that increases in each chapter. Hence why Chapters 3 to 5 are consecutive, and so are Chapter 6 and Chapter 7 in parallel. Chapter 6 is not exactly the continuation of Chapter 5 since it is based on Poorte's work and conclusions [4].

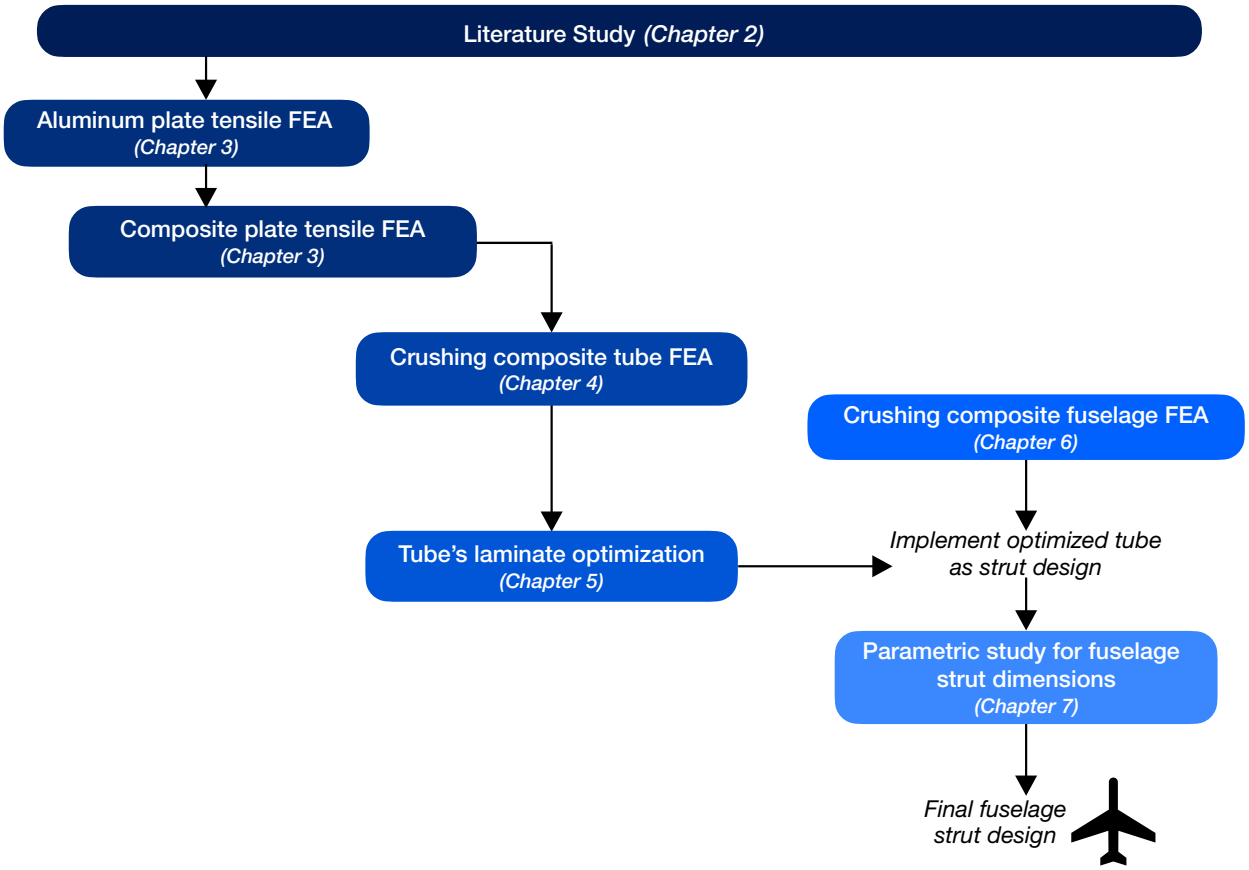

Figure 1.1: MSc thesis topic and its research methodology diagram.

Chapter 2

Literature Study

This chapter presents an introduction to the state of the art in structures' design and their optimization under crashworthiness requirements. To do so, this chapter is divided into four main sections. Section 2.1 describes in detail the concept of crashworthiness, the metrics to evaluate this on structures, and the regulations that both aeronautical and composite structures should follow to comply with it. Section 2.2 presents the finite element modeling as a means to use numerical simulations to study crashworthiness in structures. Then, Section 2.3 explains experimental setups that can validate numerical simulations in structures from different vehicles. Finally, Section 2.4 presents ways to improve and optimize the design of a structure of interest, including considerations, parameters, and difficulties to take into account when applying these changes. This is relevant to this thesis, as the same train of thought will be used when optimizing the fuselage struts in future chapters.

2.1 Crashworthiness

This section introduces the concept of crashworthiness and the most relevant parameters to study it. A broad definition of crashworthiness would be the following: "the term crashworthiness refers to the ability of a design and material to protect its passenger, cargo or/and valuable from injuries, damage or/and death crash incidence" (p.2, Isaac and Ezekwem [12]). This definition applies to all kinds of vehicles, and for all of them, the way to achieve a crashworthy behavior is for the structure to dissipate the kinetic impact energy through deformation or damage. This means that the selection of the structure's material is of relevance because it makes the energy absorption process more or less efficient [12]. While absorbing energy, the amount of energy that is experienced inside the vehicle is minimized by storing as much as possible in the structure, which delays the high crushing loads from reaching the cabin and cargo compartment. That lowers the acceleration peaks caused by the impact loads exerted on the structure, which minimizes the harm done to the occupants or cargo inside the vehicle [13]. Conventionally, vehicles have been using metals as structural materials due to their efficient mechanism to absorb energy through plastic deformation. However, the introduction of composite materials to structural applications requires further research on their energy absorption mechanism. Their brittle behavior leads them to absorb the energy differently, and in some cases, they need the aid of additional energy-absorbing structural components. When using these aids, like composite tubular parts on a car chassis, the composite structures improve their crashworthiness and can handle more damage than steel or aluminum metals [14].

Regardless of the materials used in a vehicle's structure, the indicators to assess its crashworthiness are the following: the total energy absorbed (EA), the peak or maximal axial crushing force (F_{peak}), the specific energy absorption (SEA), the mean or average axial crushing force (F_{mean}), the crushing load/force efficiency (CLE/CFE), the stroke efficiency (SE), the stroke length per unit mass, the energy absorbed per unit stroke length, and finally, the percentage of energy absorbed.

First, there is the EA by the vehicle's structure during impact [13, 15]. This indicator is the area of the resulting force-shortening graph considered in Equation (2.1), where $F(x)$ is the instantaneous crushing load and x is the stroke length [13, 15]. To maximize the EA, the force value should stabilize its value and not drop after the initial triggering deformation. That way, the area and integral value from above remains high and

the structure absorbs more energy. Otherwise, the structure would not be able to absorb as much and the loads reaching the occupants' area would be too high to consider a survivable crash[13, 14].

$$\mathrm{EA} = \int_0^x F(x)dx \tag{2.1}$$

Then, there is the F_{peak} from the structure's resulting force-displacement graph, which is the maximum force experienced during impact (see Equation (2.2)) [15, 16]. A low F_{peak} in a force-displacement graph leads to a reduction in the energy absorbed area below its curve. This force induces accelerations (or decelerations) to the structure, which are directly proportional to the F_{peak}. If the F_{peak} is too high, the accelerations induced can jeopardize the safety of the vehicle's occupants. Then they must be kept at human tolerance (below 20g) for the impact to be survivable [13, 14].

$$\mathrm{F_{peak}} = max((F(x)) \tag{2.2}$$

The SEA is defined as the ratio from Equation (2.3) [14, 15, 16]. The mass from Equation (2.3) refers to the structure's absorbing mass or the mass under deformation ($mass_{abs}$), but under no circumstance does it include the undeformed or total structure's mass.

$$\mathrm{SEA} = \frac{\mathrm{EA}}{\mathrm{mass_{abs}}} \tag{2.3}$$

The F_{mean} of the loads experienced upon impact in the force-displacement graph is calculated using Equation (2.4) [14, 15, 16].

$$\mathrm{F_{mean}} = \frac{1}{x}\int_0^x F(x)dx \tag{2.4}$$

The CLE or CFE is the ratio from Equation (2.5) [15, 16]. This ratio should tend to unity, as it measures how stable the crushing force is to maximize the EA [13, 15]. The higher the ratio, the more stable the crushing force is and the more energy is absorbed throughout the impact.

$$\mathrm{CLE} = \mathrm{CFE} = \frac{\mathrm{F_{mean}}}{\mathrm{F_{peak}}} \tag{2.5}$$

The SE is the ratio of the crushed length of the structure ($L_{crushed}$) over the entire length of this one (see L_{total} in Equation (2.6)). The ratio from Equation (2.6) should tend to unity for the whole length to contribute to the energy absorption of the structure [13, 15]).

$$\mathrm{SE} = \frac{\mathrm{L_{crushed}}}{\mathrm{L_{total}}} \tag{2.6}$$

The remaining parameters are the stroke length per unit mass, the energy absorbed per unit stroke length and the percentage of energy absorbed. All three indicators depend on the parameters above and their formulas. First, the stroke length per unit mass is the ratio between the crushed length and the total mass of the energy-absorbing structure. This parameter helps design longer crushing lengths while minimizing the mass of the structure [13]. The energy absorbed per unit stroke length ratio must be maximized to absorb as much energy as possible in a structure during the crash. And finally, the percentage of energy absorbed shows how effective the structure is in absorbing energy.

In conclusion, when designing a structure that has to behave a certain way during a survivable crash at low speeds and altitudes, the structural goal (as mentioned above) is to absorb as much energy as possible with a high SEA and CFE and a minimum mass involved [13, 14]. These requirements enhance the use of lightweight materials for crashworthiness purposes. However, the most common limitations in crashworthy structures nowadays are that they experience a very high F_{peak} and a low SE [13].

2.1.1 Aeronautical crashworthiness

For an aircraft, a survivable crash can only occur during the flight phases of take-off, climb, approach, and landing [17]. Other phases of a flight include high altitudes and the energy involved in the crash would be too much for occupants' bodies to handle, so it is unlikely that they would survive. Additionally, accidents with higher impact velocities are unlikely to happen, so studying them for crashworthiness purposes would

not increase significantly the survival of the occupants in other lower speed conditions [18]. To guarantee the survivability of the aircraft passengers, the structure of the vehicle is studied so that this one deforms in a safe way and without interfering much with the occupants' living space of the cabin during a crash. Hence, structural optimization for crashworthiness purposes is of importance for the occupant's safety, as the deformation must be controlled to guarantee survival in such cases.

All crash events in the aeronautics sector include vertical and horizontal velocities. Despite this, it is not necessary to study every impact scenario possible to study aircraft crashworthiness. Nonetheless, the vertical response of the aircraft to an impact is the main difference when comparing crashworthy responses between crashes. This means that when the first point of contact during impact occurs at the nosecone or tail of an aircraft, both vertical and longitudinal accelerations are induced. Despite this, the components of the aircraft show a larger design sensitivity in the vertical response of the impact, which is why the aeronautics sector assesses purely vertical crashes for crashworthiness purposes [18]. Hence, the vertical response for loads and induced accelerations is studied in this thesis, which looks like the vertical acceleration profile at the cabin from Figure 2.1.

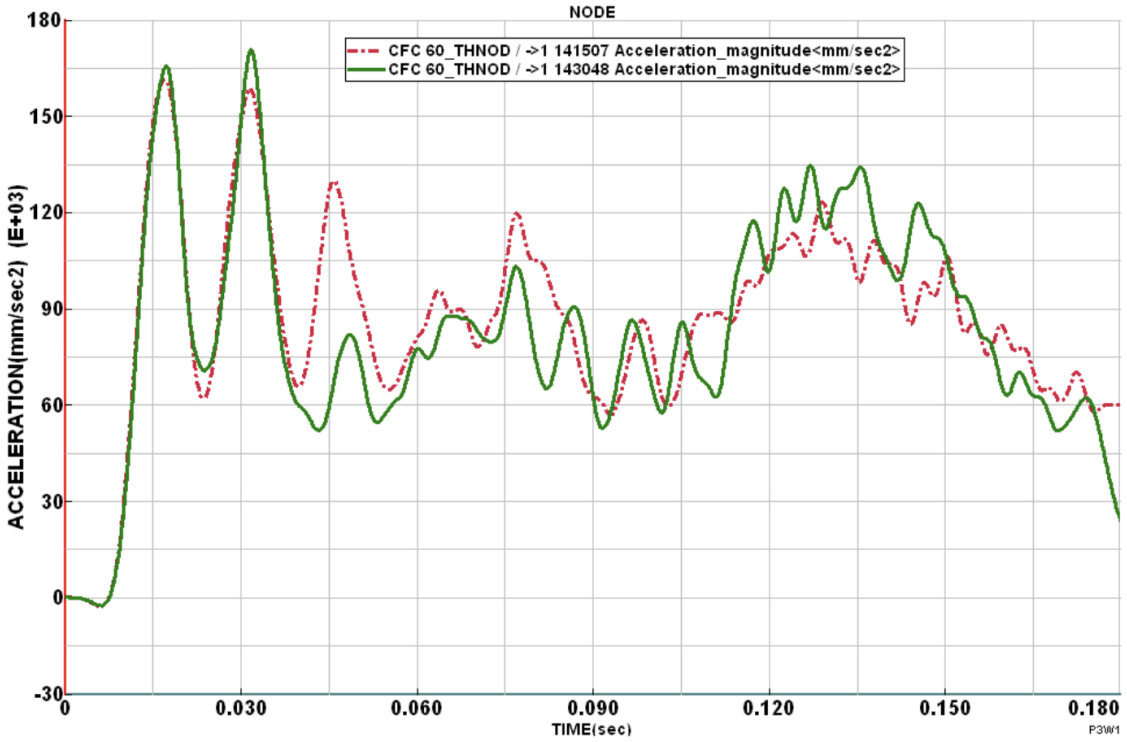

Figure 2.1: Acceleration profile resulting from the fuselage numerical model section seats. Figure taken from p.4 in Xue et al. [19].

Figure 2.1 shows several acceleration peaks throughout the impact process. These magnitudes of the peaks and their duration represent the loads experienced by the occupants of the aircraft. The downside of the bodily injury factors mentioned earlier is that they only measure whether the induced accelerations in the crash are within human tolerance or not, but they do not correspond straight away to the magnitude of the decelerations or their duration from the graph's response [18]. That is why further analysis of the acceleration response is required to assess survivability and structural damage.

Two main peaking areas are identified in Figure 2.1. The first peaking area is due to the bottom of the fuselage crashing on the ground for the first time. The way this first contact happens, there can be one clear peak in the response or several sub-peaks around it like in this case. After that, there is a gradual general decrease in the acceleration induced due to the deformation of the structure as a dissipating mechanism. Then, a second peaking area arises when the struts of the aircraft hit the ground and keep the frame from deforming further [19]. The desired acceleration response would bound both peaking areas to be lower and longer in duration

to delay the effects of the induced accelerations when reaching the cabin. Reddy et al. [13] attribute this delay to the crushing stroke being long to maximize structural's SE. This implies that crashworthiness improves as well as the survivable conditions for the occupants.

2.1.1.1 Structural parts of interest for crashworthiness

As mentioned in the previous section, the crashworthiness of an aircraft can be improved by studying its vertical crash conditions of this one. While the entire structure must be taken into account for the crash response, in this thesis the focus for assessment remains on the part of the structure that contacts the ground. Hence, the fuselage's sub-floor.

From the 1930s onwards, the fuselage sub-floor of aircraft and helicopters has been mainly made from aluminum alloys [6, 20]. This is because they are considered great energy absorbers for their "steady plastic deformation and low weight" (p.63, Reddy et al. [13]). Nonetheless, aluminum presents a big downside which is corrosion. So this has influenced the need to introduce composites to the aeronautics sector. Examples of this are the composite-dominated aircraft B787 Dreamliner and the metallic-composite hybrid aircraft A350, which is made of carbon fiber reinforced plastics (CFRP) with epoxy resin for the composite part [21]. In some other recent studies, thermoset sandwich constructions with E-glass/epoxy sheets and foam core are introduced to fuselages with a frangible outer shell in their lower section so the floor absorbs energy more efficiently [22]. The current trend is to have hybrid fuselages with more than one material in them and depending on the components' required performance. This has been hinted at by the introduction of composites into the A350 and B787 examples, but before getting into detail on which materials are changed in some components, it is important to mention which of the sub-floor components are of most importance when it comes to crashworthiness assessment. The most relevant structures in an aircraft for energy absorption purposes are the frame, the cabin's skin and floor, the stringers, the struts, and the cargo floor with its supports. Some of these parts, especially struts and cargo supports, can be graded and use multi-cell structures for foam and honeycomb fillings when made of CFRP with epoxy resins [13, 16]). For hybrid structures, sub-floor components like struts can be made of aluminum and still be reinforced with glass fiber reinforced plastic (GFRP) composites and a foam core [20]. However, the CFRP/epoxy composite is the most popular among composite aircraft components [23, 24], which may be due to the high specific properties and tailorability this one offers for the job [13]. Regardless of their material, the mentioned sub-floor components should contribute to energy absorption. This contribution can be checked for each component by partitioning the final percentage of the total by the fuselage.

Generally, the frame is the component that absorbs the largest amount of energy in a crash since the other components of interest only contribute in the early stages of impact until failure [19]. The frame is not only responsible for the energy absorption of the fuselage, but also for the mass retention together with the upper shell structures of the fuselage to limit post-crash deformation in the cabin [25]. When made of aluminum, the frame deforms plastically to dissipate the impact energy, but when having a CFRP structure, the brittle rupture of the material limits the energy absorption. This limitation is associated with the elastic energy stored in the frame up to failure [26]. After the frame, the cargo floor absorbs the largest amount of energy from the crash. The two components can absorb even more than 70% from the EA during impact when they are made of metal. Optimization of these two components alone can then improve the crashworthy capabilities of the fuselage. As mentioned, the supports of the cargo floor are also of importance, despite these not being energy absorbing components themselves. This is because their stiffness influences the first induced acceleration peak and the way the frame deforms [19]. The cabin's skin is the third component that absorbs most energy from a crash, followed by the stringers. If the skin deformation was too large or caused a cabin floor distortion, it could impede the occupants' evacuation when needed and their lives could be at risk. If the cabin floor was to be affected in any way, the seats in the cabin would not yield appropriately nor absorb energy from the impact as they are supposed to [19]. In conclusion, the skin and stringers, together with the frame, are responsible to make a robust fuselage to guarantee survivability in the upper section of the fuselage [18]. Finally, there are the struts, which do not absorb much energy by themselves but play an important role in the energy absorption process of the crash. They are the main limiting factor for the frame's deformation once they hit the ground and generate the second peak of acceleration (see Figure 2.1). When they do not let the frame deform further, they are not letting it absorb any more energy [19]. Struts' cross-section geometry and dimensions can also influence the EA for typical shell components, as is shown in future stages of this

thesis research. Adding corners on composite struts can reduce their EA due to possible fiber damage. Hence, circular and conical shells present better crashworthiness metrics, while hourglass cross-sectioned shells are very high in SEA [27].

In the next section, it will be clear how these structural parts and materials affect the regulations of crashworthiness that are to be applied to aircraft.

2.1.1.2 Crash requirements in aeronautics

This section focuses on the crash requirements that are applied to aircraft nowadays. This thesis studies the novel implementation of a thermoplastic composite in an aircraft. However, the current regulations for a large commercial aircraft only apply to conventional metallic fuselage designs in CS-25.561 and CS-25.562 (p.271-272 in EASA [2]). As a consequence, research is needed on how composite or hybrid aircraft are being certified for crashworthiness purposes. Neither hybrid aircraft like the A350 nor composite aircraft have official crashworthiness regulations like metallic aircraft do. Then, equivalent requirements are set to a specific aircraft model through special conditions (SC). These guarantee similar safety standards to an already certified aircraft of the same category, size, and configuration [21, 28]. Also known as similarity assessment, where novel design features of an aircraft are evaluated, and compared to the ones from a similar aircraft of reference that has been already certified. These new features can be a novel material like a thermoplastic composite, a reduction in the cargo floor space, or a new configuration in the relevant structural components of the fuselage [18].

According to Duven [21] there is the need to use similarity assessment because when changing a key design feature like the materials from the fuselage. The current regulations are not appropriate for the new aircraft because the crashworthiness behavior has changed, and so has its required safety level. For example, a composite aircraft can have poor crash-worthy behavior when applying conventional safety requirements from an aluminum aircraft. The requirements may be good for a certain design, but cannot guarantee these work for a completely different aircraft. This is why composite aircraft need to be compared among themselves to achieve a similar behavior to the conventional safety standards, but they will not get the same numerical restrictions because these do not work for them. The similarity is therefore only applicable to those aircraft that have similar SC and design features, as long as occupants' survivability is not jeopardized [29]. If the desired behavior is not achieved, additional energy absorption devices can be added to composite structures to dissipate the energy of the crash with a minimum mass penalty [21]. These devices and the airframe relevant structural parts have to ensure that energy is being absorbed through a controlled failure in the fuselage's sub-floor, which depends on many factors like material and structural configuration [18].

One of the main comparable features in a similarity assessment for crashworthiness analysis is the Limit of Reasonable Survivability (LRS). This parameter is the vertical impact velocity in which occupants' survival differs from the certified aircraft of reference when both of them are under the same conditions. That occurs when the new design shows structural disruption to the point where provisions for survival are not enough to guarantee this one. Of course, to compare this between aircraft, both fuselage sections of the study must be representative, loaded vertically, and allow a comparison for a range of impact conditions according to EASA [29] and Transport Aircraft Crashworthiness and Ditching Working Group [18]. In other words, LRS is the maximum capability of an aircraft design to comply with its crashworthiness criteria. Aircraft with less depth below the cabin may not have enough structural absorption to meet their requirements [18], and if that was the case CS-25.562 from EASA [2] is supposed to be used as guidance.

Transport Aircraft Crashworthiness and Ditching Working Group [18] proposed SC to FAA for structural goals in composite aircraft. These goals are to be reached through a new proposed airframe crashworthiness rule 25.XXX for the certification of these new designs. Rule 14 CFR 25.XXX gives two options for certification: the similarity assessment when similar comparable aircraft exist and have already been certified (14 CFR 25.XXX(c)), and an alternative to those novel designs that cannot use comparison to get crashworthiness certification (14 CFR 25.XXX(a)(b)).

Regulation 14 CFR 25.XXX(a)(b) for non-similarity specifies that fuselage must be designed to ensure occupant survivability during a survivable crash up to 30 ft/s, which rounds up to 10 m/s in the International

System of Units (SI). All while showing compliance with the four vertical impact criteria:

- Retention of items of mass.

  The occupants of the aircraft must be protected against the release of items of mass in the cabin that can be caused by the resulting structural deformation or loads experienced during the crash in the airframe or floor structures [21, 28, 29].

- Maintenance of acceptable loads and accelerations for the occupants.

  To keep these bounded, the structure must absorb energy in the sub-floor through progressive and controlled failure, especially if components suffer from compression, tension, and bending loads [26, 28]. Accelerations experienced in the cabin should agree with CS-25.562(b) from EASA [2]. Stiff structures can increase these loads easily but avoid intrusions to the cabin, while softer structures can lower the intensity of acceleration peaks and increase their duration [13].

- Maintenance of a survivable volume in occupants' areas during and after the crash.

  The fuselage deformation must not interfere with normal living space from the cabin to prevent injuries and aid the egress paths. This space is defined as the distance from the cabin ceiling to its floor that must not make the occupants be in contact with the structure to prevent serious injury [28]. Large geometrical deflections and non-linear material behavior need to be taken into account to prevent that.

- Maintenance of the emergency exit paths despite the damage to make evacuation possible.

  No structural deformation must interfere with the post-crash evacuation [21]. Floor warping shall be minimized but local failures are acceptable as long as the occupants can evacuate safely. As for the emergency exit, its door must open and its surrounding structure should not deform permanently to avoid a jamming situation. Therefore, a representative fuselage with doors can help study if this can be ensured. Otherwise, the structure's design must be conservative and make it all survive the maximum expected load of the area.

All the criteria from above can be applied to composite aircraft while keeping in mind that they can have mass penalization and that the fuselage must still be as lightweight as possible [13]. Also, the four main goals can be reached using passive safety measures and letting the structure absorb the energy of impact [17].

The compliance of criteria from rule 25.XXX(a)(b) can be assessed through numerical analysis supported by test evidence for validation, pure testing, design reviews, similarity assessment (14 CFR 25.XXX(c)) or a combination of any of these [18]. Structural design optimization methodology may be useful to design a proper model and analysis before the validation of this one with the testing data, which must cover from coupon level to large-scale components of the fuselage if proper analysis validation is wanted [17].

One of the most common techniques to study crashworthiness, not only in aircraft but in any other composite structure, is the numerical analysis validated by test results. When this methodology is chosen, the fuselage section must be representative enough to give the most valuable results possible, since aircraft loading, structural dynamic considerations, progressive failures, and local strain rates can change along the section [28].

2.1.2 Composite crashworthiness

Here, composites used in other structural applications apart from aeronautics are considered. In the aeronautics sector, the reference for crashworthiness standards was established on metallic aluminum structures, but composites have other strengths that are considered in other sectors for structural purposes. That is the case in the automotive sector, for example.

Starting in general terms, the crashworthiness assessment is approached differently in composites than in metals. Composites are anisotropic and have a quasi-brittle fracture and limited plasticity according to Di Palma et al. [17]. So these materials absorb energy elastically until failure through matrix cracking, delamination, fiber fracture, and crushing or fragmentation [30]. Due to their low density, they present a higher SEA than metals. Composites also control structural vibrations better and reduce noise according to Isaac and

Ezekwem [12]. Nonetheless, they perform worse at high temperatures and exposure to humidity, reducing tensile stress and fatigue strength [27].

A crashworthy behavior in composites strongly depends on SEA and EA, which are the most recurrently used assessment indicators for these materials. The desired behavior, however, for a structural application involves a high SEA, EA, and CFE while F_{peak} is kept low [12]. SEA decreases with temperature and varies with ply orientation, 45° being critical for energy absorption, which depends on the laminate design, temperature, structural geometry, and loading case [27]. Modifications on the laminate design need special attention when a specific mechanical behavior is wanted. The addition or depletion of a ply or even the change in the stacking sequence can change the failure mode and the energy absorption features of the structure [12, 28]. Typical composite components are shells, whose small thickness can be neglected, and therefore, can be assessed using the SEA metric indicator instead of the EA [27].

The crashworthiness behavior in shell composites is usually studied upon axial crash loads for higher efficiency, but structural failure is associated with bending very often. The axial loading causes the strain rate and the crushing speed to influence the material properties while bending increases EA when rectangular cross-sectioned specimens bend over their strong axes. In real crashes, a combination of both loading cases is common and the way shells fracture then affects the loading stability and the magnitude of the crash loads. Shells collapsing in a stable, controlled manner are better energy dissipators according to Mamalis et al. [27]. Regardless of the loading case, composite materials fail at a microscopic level before they show their fracture macroscopically. In the case of axial loading, transverse shearing and lamina bending crushing appear microscopically before they show the macroscopic modes of failure (I, II, III, and IV). The progressive one (Mode I) is the failure mode that absorbs most energy, according to Mamalis et al. [27].

When it comes to applications, there are different combinations of matrices and reinforcements that can do the job depending on the required performance for the structural part. Fiber reinforcements are popular as they give a great performance in vehicles. The most common ones are CFRP, GFRP, and aramid fibers. Yet they present differences in energy absorption performance, as CFRP absorbs more energy than GFRP and aramid fiber reinforcements according to Mamalis et al. [27]. The US Department of Transportation and FAA [28] mentions that these reinforcements use synthetic matrices like thermoset epoxy to obtain higher properties, and the reason aeronautics use CFRP is partly because it presents a higher SEA than a GFRP with the same matrix and fiber content. Nonetheless, GFRP is a cheaper material that works well in other industries like automotive. Alkaline free Electrical-GFRP (E-GFRP) and Strength-GFRP (S-GFRP) are then the variations of glass reinforcement that work best for energy absorption purposes, but these composites need to study well the fiber orientations of their stacking sequence because CFE, F_{mean} and F_{peak} depend strongly on it [12]. The different reinforcements also present differences in properties when changing shapes. For example, from Isaac and Ezekwem [12], GFRP hollow tubes are higher in SEA when their cross-section is a circle. For CFRP it happens the opposite: the circular hollow tubes have the lowest SEA and conical and squared tubes have a better performance.

So far, the mentioned reinforcements have been combined with a thermoset resin epoxy, which is widely used in structural applications that need high performance. Nevertheless, thermoplastic resins are making their way in some industries because of their high molecular weight and temperature sensitivity, which makes them more sustainable. These materials, although less popular, are already in use in the automotive industry as energy absorption devices. The most common thermoplastic resins used for the purpose are nylon (polyamide), polystyrene, polypropylene, polyethylene, polyetherether ketone (PEEK), and polyvinylchloride [12]. Actually, according to Mamalis et al. [27], PEEK in combination with carbon fibers provides a high SEA for energy absorption applications.

An application of a thermoplastic composite with glass fibers is presented in Kim et al. [31] for a car's front bumper beam. For this case, the design requirements for the structure state that the thermoplastic bumper can progressively deform but it must not make contact with any other components of the vehicle during and after the crash for safety reasons. This is to reduce the intrusion and the risk of injury inside the vehicle.

To study this kind of application for composites, numerical analysis supported by test results and purely testing are common. The analysis of composites is a bit complex, as it needs an extensive investigation of

the model's sensitivity to generate a model with the right parameters for mesh optimization or stress-strain element data [28]. Despite this, composite destructive tests are expensive and may have financial constraints to obtain accurate results, which is why failure analysis and numerical simulations are still the way to go. Mamalis et al. [27] present finite element modeling as a logical approach for numerical simulations to obtain energy absorption predictions.

2.2 Modelling and simulation

In large and complex structures, spending lots of time and resources on an experimental study for crashworthiness is too costly, which is partly why numerical simulations are an effective tool to predict the crashworthiness of these structures. Numerical simulations deepen in understanding of structural behaviors and ease the search for an optimal design [19]. These also save time, present more flexibility to change setups for every analysis, and allow the retrieving of data from more points than the ones used in an experimental setup. To use numerical analyses as an assessment tool, non-linear dynamic simulations need to be reproduced in software such as Abaqus or LS-DYNA, which are the most popular nowadays for crash studies [13, 32]. According to Kim et al. [31], Transport Aircraft Crashworthiness and Ditching Working Group [18] and Reddy et al. [13], impact simulations of the sort need to provide a reliable analysis by validating this with test evidence.

The methodology used in this thesis is the Finite Element Model (FEM) approach, which can handle the complexity of deformation mechanisms and the changing boundary conditions [13]. The FEM approach does not need experimental data to calibrate the elements introduced in the analysis because it takes mechanical properties from the design concept. The analysis is supposed to predict the kinematic response of the structural components upon impact, deformations, failures and strains and accelerations in critical interface locations [18]. For that, FEM offers very detailed geometries that give good failure predictions with the right material assigned from the libraries of the software code and fixes a mesh in the material to make it distort alongside the structure. Explicit codes allow studying element by element without the need to define a global stiffness matrix, which is preferable in structures that present large deformations, and the inertias cannot be disregarded [25]. Nevertheless, when searching for the optimal design, changes in the configuration of a structural element require extra analysis to verify that the crashworthiness parameters are improved [13].

2.2.1 Modelling of aeronautical structures

Transport Aircraft Crashworthiness and Ditching Working Group [18] present the main considerations when using a numerical analysis for the design of an aeronautical structure. The analysis for crashworthiness must include boundary conditions, external and internal loads, structural element types, assumptions, parameters and energy dissipation schemes, structural configuration, materials characteristics like failure, strain rate, stiffness, energy absorption, sustainability, and stacking sequence if applicable. In addition to that, deflections and deformations must be predicted in a range of payload configurations as long as they are certifiable. Each of the modeling parameters must be evaluated through sensitivity analysis to see how they affect the outcome. However, crash dynamics and energy absorption are hard to model while keeping a representative structure of study [28]. Each aircraft has a particular impact behavior, so approximations in the modeling can cause inaccuracies or uncertainties. These are then measured through, for example, Sprague and Geers (S&G) method, relative error and ISO/TS/18571 for Transport Aircraft Crashworthiness and Ditching Working Group [18], and sensitivity analysis for Vignjevic and Meo [6].

In the following sub-sections, examples from the literature are used to explain how modeling and analysis processes work for a finite element model.

2.2.1.1 Tools and software

Most of the examples that help to reproduce the modeling process use software codes like Abaqus, LS-DYNA, PAM-CRASH, and MSC Dytran. LS-DYNA is the one that will be used in this master thesis, so checking how these procedures for simulation characterization work is useful and explained in more detail in the following sections through examples. Despite this, it is worth mentioning that Schwinn [30] presents an alternative way to implement a finite element simulation for a vertical impact on a fuselage in AC-CRASH that reduces file

size, data processing errors, and redundancy. This program is not a graphical interface like the other codes, but it works through input files that define the aircraft model along with its geometry, structural layout, materials and characterization, structural elements, loads, mesh discretization, and solver control parameters. The tool to generate the files is the Common Parametric Aircraft Configuration Schema (CPACS), which needs additional tools like PROSHAPE, ANSYS, PAMCRASH to generate the model and introduce it in the end to the simulator AC-CRASH.

2.2.1.2 Structures' modelling

The numerical simulations considered in this and the following sections are either hybrid or thermoset composite structures applied to fuselage components for a vertical crash, as there will be an explanation of how the following scenarios are modeled for an impact simulation throughout this sub-section. Metallic aircraft components and primary structures are not presented, as they do not have relevance to this thesis topic.

Meng et al. [33] model and compare two aircraft designs: a conventional one (see Figure 2.2a) and a new design with honeycomb layers and a lower clip plate at the bottom of the fuselage (see Figure 2.2b). The focus on modeling will be placed on the common ground and differences in both designs but not on the modeling of the honeycomb as it is out of the scope of the thesis.

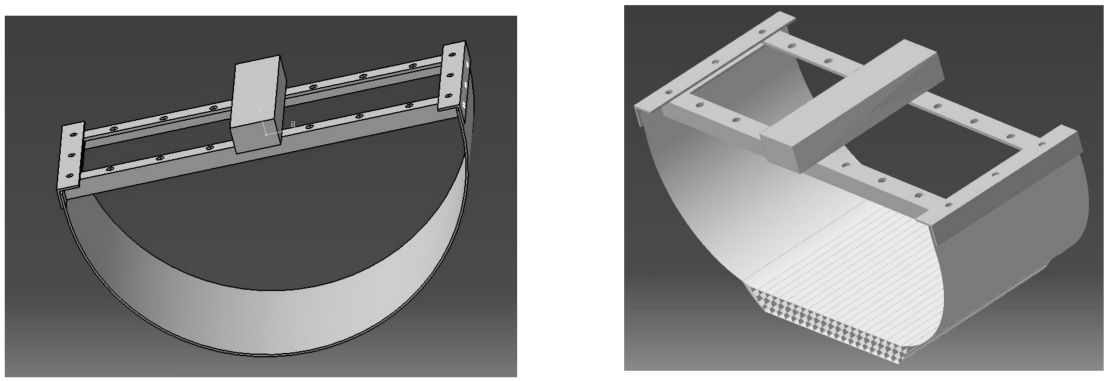

(a) Conventional fuselage design.

(b) Newly proposed fuselage design.

Figure 2.2: Conventional versus newly proposed designs. Figures from p.85-86 in Meng et al. [33].

Riccio et al. [24] present the modeling of the CFRP-epoxy floor support system in the fuselage's cargo area. The sub-component is delimited by a metallic frame as shown in Figure 2.3. Two equal specimens are submitted to different impact speeds to study both the linear elastic regime at low impact speeds and the dynamic behavior at larger speeds.

Schatrow and Waimer [26] models a two-bay thermoset CFRP fuselage vertical drop. The design considers the energy absorption concept through crash devices, all below the cabin floor. There is a crash device in the sub-cargo structure where kinetic energy is absorbed by tension failure, as bending loads induce tension loads to the cargo crossbeams. The second crash device is at the frame, where bending loading is expected. The last device is at the frame-cabin floor intersection to absorb again through tension. The stiffness of the cabin floor and the tension loads induce an oval-shaped deformation in the upper region of the cabin.

Heimbs et al. [34] models low levels of the testing pyramid explained in Transport Aircraft Crashworthiness and Ditching Working group [18]. The models cover coupon and structural element levels, in which quasi-static conditions are used to determine material characterization before studying the dynamic response. The coupon model is studied in a three-point bending load case and the element model is studied in a four-point bending load case. The latest case uses metallic caps at both ends of the frame to introduce the load.

Jackson [22] models a fuselage vertical free fall with thermoset sandwich construction for roll angle variations of 0° and 15°, as shown in Figure 2.4. The fuselage section sub-floor is made of foam blocks on Alkaline free Electrical glass (E-glass) and epoxy fabric sheets, and has an outer shell at the bottom [22].

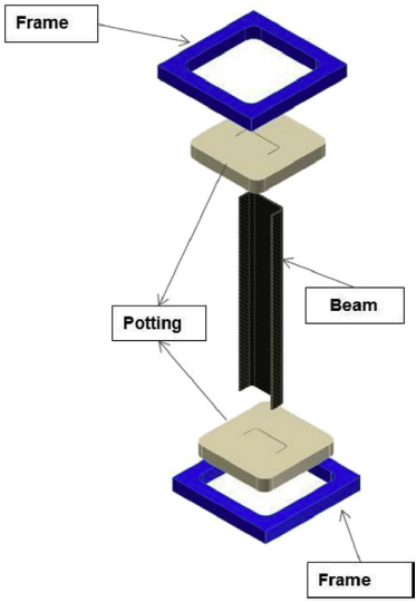

Figure 2.3: Set up of the sub-component of study. Figure from p.96 from Riccio et al. [24].

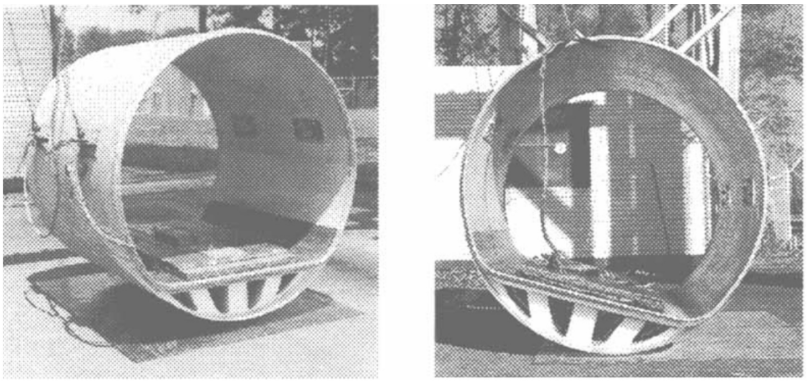

Figure 2.4: Fuselage section prior to 0° roll (left) and 15° roll (right) tests. Figure taken from p.111 in Jackson [22].

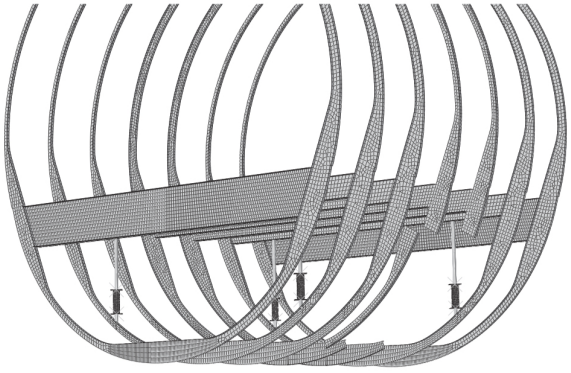

Figure 2.5: Main frames and hybrid strut configuration. Figure taken from p.433 in Paz Mendez et al. [20].

Paz Mendez et al. [20] develop a Boeing model 737 series 200 (B737-200 aircraft model) with the mainframe and strut configuration shown in Figure 2.5. Four thin-walled aluminum vertical struts are reinforced with

GFRP and a foam core. The struts have flat connectors at both ends and two cross-sections are considered: squared and circular geometries. Relevant structural parts of an aircraft and the items of mass of the cabin are also represented in the fuselage section of the study. Windows are also added to the model with simplified corners and associated frame stiffeners. Cut-outs and complex features as such are not added because they add cost more than value to the analysis. Symmetry conditions are set up at the top of the fuselage.

2.2.1.3 Material characterization

An important part of the modeling is that the materials are well defined and that clear failure criteria are set to give the expected results. The software codes have libraries to define each type of material, from metals to composites. Generally, purely elastic, or elastic-plastic material models are used to characterize soft materials like sandwich hybrid sheets and cores. This is the case for the metallic caps from Heimbs et al. [34] and the foam core of the sandwich constructed fuselage from Jackson [22], which use an elastic material model. For the sandwich E-glass/epoxy face sheets from Jackson's fuselage [22], the elastic-plastic material model is used for characterization.

The failure criteria attributed to the mentioned elastic material structure from Heimbs et al. [34] is Hashin's both at coupon and element levels of the structure. This last one includes the removal of the whole element once it fails in every ply. As for the elastic-plastic material structures, Jackson's sandwich elastic-plastic face sheets consider strain hardening to represent their E-glass and epoxy behavior better [22]. Hardening is also considered as a yield and failure criterion for the helicopter's sub-floor, which is considered isotropic in this case, has no strain-rate sensitivity in the material but has an equivalent plastic strain of 12% as failure criteria.

Composite materials from Riccio et al. [24] usually need both inter-laminar and intra-laminar damage models to define their behavior in the simulation. The intra-laminar damage consists of fiber breakage and matrix cracking, which are both evaluated by using Hashin's failure criteria. Inter-laminar damage, on the other hand, is simulated by the Cohesive Zone Method (CZM) (see Section 2 from Riccio et al. [24]). However, it is possible to define a composite material as elastic by using the finite element kinematics model approach. This is the case of Schatrow and Waimer's thermoset CFRP fuselage [26], which models the material of the shell elements as orthotropic and the beam ones as isotropic and does not include strain rate dependencies. The damage is assessed in the expected areas (or kinematic hinges) by using pure bending and Hashin criteria. The areas where damage is not expected use the same linear-elastic material formulation but no defined failure criteria.

2.2.1.4 Meshing

The mesh of the model to represent in a simulation can be done in the mentioned structural analysis programs, or imported from another one and then assign their element types. The mesh generation is an important part of the modeling because it can be generated by the trade-off between accuracy and computational cost [20]. The finer the mesh, the better results the simulation gives for the resultant structural deformations [26], but it takes much longer to compute. In each article, the discretization of the models is done similarly for the same purposes, but using different cell types per element. Generally, the areas that expect large deformations use Belytschko-Tsay shell elements for the mesh, which in other words, contribute to the structural energy absorption [26]. This is the case of the inner and outer composite face sheets in the upper section and floor from Jackson [22].

Figure 2.6: Post-test damage in circular (left) and squared (right) struts. Figures taken from p.441 in Paz Mendez et al. [20].

Some shell elements can use coarser mesh elements for simplification. This is the case of the three-point and four-point bending coupon modeling from Heimbs et al. fuselage [34], which does not consider delamination, so additionally, it can use just one integration point per ply. Paz Mendez et al. [20] discretize as shell elements as well the skins, floor, frames, and under-floor beams of the aircraft. Each of them with five integration points through the thickness. This is because shell elements represent better the behavior of the components and the plastic hinges' appearance during impact. As presented in Figure 2.6, hybrid struts of this study need fine meshes to show fold formation and analyze which strut geometry is best.

Sometimes, the supports from the shell elements are modeled as beam elements [35]. These expect some deformation or friction worth computing, because it is induced from the large deformations in the shell elements, but should not take as much computational time as the primary structural parts discretized. Other beam elements can be defined in stringers, sub-cargo, and seat struts because they do not contribute to the energy absorption directly, but deform as a consequence of the primary structures crushing. From Paz Mendez et al., the majority of the structure does not use beam elements as they would not show local buckling or crippling. Hence, beam elements are only used for the omega-shaped stringers to reduce computational cost.

The impactors or regions where little to no damage is expected use solid elements and a coarser mesh for simplification and saving computational costs. Examples of these solid elements can be the impact plates from Riccio et al. [24], the honeycomb dampers from Heimbs et al. fuselage [34], the metallic caps at the ends of four-point bending element frame [34], the foam cores from the upper section, floor and sub-floor of Jackson's fuselage [22]; and the impactor from Paz Mendez et al. [20], which uses solid elements with reduced integration.

As boundary conditions, most of the time the impact plates are the ones to move in the simulations for simplicity, so the body is encastered by its nodes at the bottom and the impactor top nodes have an assigned velocity downwards. This is the case of Riccio et al. [24] sub-floor crushing, and the model from Schatrow and Waimer tension absorption model [26], which includes gravity boundary conditions in its vertical direction as well, and symmetry to consider the front and back of the simulation model. The impactor moves also when the aircraft is rotated using a roll angle. In such case, it is the impactor the one that rotates 0° or 15° with an assigned initial velocity [22]. The velocity assigned refers to the vertical component to simulate a pure vertical crash.

Sometimes, however, the impactor is the one to remain fixed, and it is the structure that moves, which simulates the reality of an aircraft survivable crash. The honeycomb sub-floor model from Meng et al. does this, considering the impactor as a rigid plate with a sliding surface [33]. Regardless, of the setup for the crash, the contact condition is always set between the impactor and the aircraft structure for this last one to act in consequence of the crash. The contact condition from the impact ground to the skin of the fuselage is defined with a friction coefficient for the tangential contact [26]. Then, it is time to indicate LS-DYNA which element pushes which through a master-slave contact condition between the nodes or surfaces [8]. Jackson [22] fuselage conditions, for example, use a master-surface to slave-node contact for the interaction between the sub-floor and the impact ground.

2.2.1.5 Results and validation

After the crushing analyses are conducted, a validation with test evidence is possible occasionally, which is the case for most of the example analyses presented in this sub-section. Firstly, the results from the Meng et al. numerical analysis show that the structural deformation is captured adequately in it when compared to the tests recorded for both fuselage sub-floor designs. For the new design, all acceleration peaks are higher than the ones measured in the tests, which can come from honeycomb imperfections affecting the energy absorption, or due to the assumption that the modeled ground is more rigid than it is in real life. The roll angle is concluded to affect the new design's energy absorption capabilities, but this one is not too significant for such low angle rotations [33].

Riccio et al. measure accelerations and comparison to tests prove that fibers' compression damage is the mechanism that leads the structure to fail. The intra-laminar damage extends all over the sub-component

and delaminations are also found in the central area. Interfaces between 0° plies (aligned with the load) are the most susceptible to suffer from inter-laminar damage [24].

Tension crash absorbers from Schatrow and Waimer [26] allow simultaneous energy absorption in several crash devices at once, which absorb more impact energy and bound peak loads reaching the cabin.

Heimbs et al. [34] dynamic frame simulation results show that matrix cracking occurs due to tensile loads, which leads to stiffness degradation. The maximum displacement at failure is well predicted by the simulation despite using a more conservative approach than the tests by not considering strain-rate effects. Bending failure prediction has a good correlation with tests and proves that complete failure is avoided when the specimen slips from the supports with increasing displacement. Then, it can be concluded that physical mechanisms and maximum load levels studied during a composite's frame breakage are well predicted through simulations, so the models can be implemented in a global crash simulation. The remaining uncertainties are assumed to be caused by the test setup and not by the component itself.

To compare the simulation results from the tests in Jackson [22], the simulation for 0° roll angle had to modify pitch conditions to 1°. There is a correlation between the predicted acceleration in the simulation and the rear accelerometer data from the 0° test with the same pitch conditions. However, the simulation presented a lower acceleration peak and a faster energy dissipation rate when compared to the test. This last one is attributed to the model not allowing to set debonding between the face sheets and the foam from the sub-floor. For the 15° roll angle case, the simulation predicts a large spike of acceleration on the right side of the fuselage (closer to the floor). It was higher and longer than the one from the test data, which can be since the simulation does not consider a pre-damaged specimen as it happened for the tests. The left side has a much more accurate prediction. The disagreements between the simulations and tests for both roll angles may be attributed to the real scenario being much more complex than predicted with combined loads in bending and shear, so the earlier failures in testing are expected.

Finally, Paz Mendez et al. [20] model results show that frames would collide with the sub-floor beams and generate very high acceleration peaks in the cabin without the help of the strut reinforcements. Therefore, struts are needed to ensure human tolerance parameters. The struts delay the damage to the lower frame structure and take the bending deformation instead, so the accelerations reaching the cabin are lower because of the more controlled damage. The square cross-section strut from Figure 2.6 provides a better and softer dynamic response to impact due to their progressive folding.

2.2.2 Modelling of composite structures

Only a few cases are presented in this sub-section as a reference to model composite structures that are not within the aeronautics sector. Finite element modeling applies to composites of all sorts for their structural analysis, as it is a valid approach for their structural representation. Therefore, this sub-section presents three different numerical simulations performed in LS-DYNA where finite element methodology is applied to two thermoset composite crashed structures and a thermoplastic composite one.

2.2.2.1 Structures' modelling

Zhang et al. [16] present filled multi-cell thin-walled thermoset composite tubes that can be filled with honeycomb or foam per cell to have a lightweight absorbing structure. The bottom end of the tube is considered a fixed end. Tubular CFRP-epoxy composite energy absorber devices are modelled also in Boria and Belingardi [32]. The application of these energy absorber structures is in automotive, and circular and squared cross-sections are considered for the tubes. Different resistance, wall thickness, and fiber orientations are also considered in the model. To simulate a real condition, a linear trigger model has to be set at the top of the model through-thickness reduction to minimize the peak loads experienced by the structure.

The final design in Kim et al. [31] is a hybrid thermoplastic composite bumper beam made of unidirectional (UD) and woven fabric reinforcement layers. The mechanical properties of each composite type of reinforcement are retrieved analytically using the Classical Laminate Plate Theory (CLPT) for the UD composite (section 2.2 from Kim et al. [31]), and Finite Element Analysis (FEA) Abaqus code is used for the woven

composite part. The bumper beam is part of the front absorbing structure of a car and is divided into 3 parts. It has a C-shape cross-section as seen in Figure 2.7, so each flange, rib, and reinforcement is considered a separate part in the numerical study and optimization.

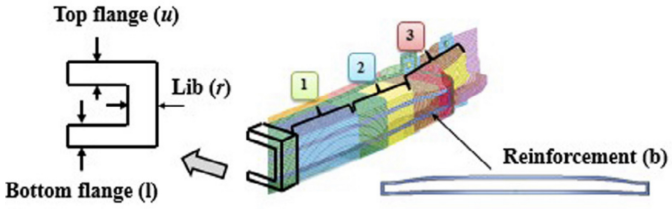

Figure 2.7: Beam elements partition. Figure taken from p.746 in Kim et al. [31].

2.2.2.2 Material characterization

The composite objects that are going to be crushed usually use linear-elastic strain-hardening material models in honeycomb fillings and tube walls [16], as well as in any composite sheet from hybrid sandwich structures. This is not the case for the impactors, which use the rigid material model from LS-DYNA to represent a strong block [16].

The failure criterion used in most of the composite simulation examples is the Tsai-Wu [31, 32], which enables validation afterward for the CFRP composite energy absorber. Additionally, the failure criteria make the computations of the simulation go much faster and avoid ductility in tubes [32]. To achieve a brittle composite behavior reproduction, the model changes the strength of the elements during collapse evolution. When an element fails in all its layers, it is deleted from the computation. When this happens, sharing nodes from the mesh leaves a reduced strength to the surrounding elements or "crash fronts". That is why sensitivity analysis is performed to understand the parameters that affect the material's failure, which is explained in p.352 from Boria and Belingardi [32].

2.2.2.3 Meshing

The meshing principle for composite structures follows the same train of thought as for the aeronautical structures section. The parts where damage and deformation are expected use Belytschko-Tsay shell elements [36], whilst solid elements are used in parts with no deformations expected whatsoever. Shell elements are used to model the buckling of multi-cell tubes with honeycomb filling. For the multi-cell tubes from Zhang et al., the change from honeycomb to foam fillings would need to be discretized using solid elements instead[16]. Belytschko-Tsay shell elements are also used for the bumper energy absorbing device from Kim et al. [31], but some energy-absorbing devices may need multi-layered shells like the tubes from Boria and Belingardi [32]. In this last case, the LAMSHT parameter in LS-DYNA introduces laminate theory to correct the assumption of a uniform constant shear strain through the thickness of the shell elements. Otherwise, there would be solid elements per layer that would add extra computation time.

With the mesh nodes' generation, boundary and contact conditions can be applied. Regardless of the filling material, the contact between this one and the tube's wall is simulated by choosing an automatic surface-to-surface contact. Each thin wall from the tube and honeycomb in itself has assigned an automatic single-surface contact for modeling [16]. This self-contact condition is also set for the friction between parts of the bumper tube's surface and to avoid element penetration [31]. Then, the contact between the impact surface and the nodes of the tubes uses the master surface-to-slave node contact setting [31].

When talking about element penetration, Kim et al. expose well have this penetration or interference with the structure itself is estimated. The distance between the mesh nodes from the bumper beam and the impact barrier is used to compute the level of intrusion and deflection in the vehicle's structure. All the surfaces of the beam and the rigid body at the back are considered as one contact group to improve the efficiency of the calculations in multiple contact impact analysis [31].

2.2.2.4 Results and validation

The results from the three modeling cases are validated using different techniques to double-check their results. The model from Zhang et al. uses theoretical predictions to validate the filled multi-cell structures by comparing the simulation mean force outcome with the analytical one from sections 3.2-3.3 in their article [16]. Each section defines the analytical prediction that each filling should meet for the F_{mean} crashworthiness metric. As for Boria and Belingardi and Kim et al., both finite element analyses' results use test data for validation [31, 32].

Boria and Belingardi's FEA is concluded to reproduce correctly the brittle crushing response of the composite tubes for axial compressive loading. Therefore the energy absorption capabilities of the structure are well estimated. Crushing features like average deceleration and final shortening prove that, with a difference of less than 10% with respect to test data [32].

As for Kim et al., their numerical setup of a Genetic Algorithm (GA) optimization coupled to the FEA iterates until GA provides the best type of fiber reinforcement for the bumper beam. The options consider carbon and glass fibers for both woven and UD plies [31]. The tests of reference, in this case, follow the Insurance Institute for Highway Safety (IIHS) protocol to measure the standard damage requirements for low-speed crashes on composites. The validation concludes that CLPT provides a good prediction of UD composites' mechanical properties. Additionally, the presence of CFRP in the UD layers improves the longitudinal tensile strength of the bumper beam energy absorber, while these would fracture even before woven layers do. It is found that transverse and shear modulus depends mostly on the thermoplastic matrix used on the bumper beam and that its performance with respect to its weight is improved thanks to the GA optimization [31].

2.3 Crash tests

Despite being an expensive and complex tool for certification in some structures, especially when using full-scale structures [17], crash tests are still used to validate numerical analysis (see Section 2.2). Usually, the more similar the simulation and test outcomes are, the more accurate the numerical model is considered [13]. However, a study on the outcome might be needed because there is always the possibility that the tests are not performed well or present outliers that need to be identified and processed before validation [13].

2.3.1 Aeronautical structures tests

In aeronautic structures, a representative fuselage section is dropped with proper boundary conditions, rigid drop surface, and cargo configuration stiffness [18]. This section does not usually include wings unless these are a high-wing configuration, which affects the crashworthiness of the structure. Since testing an entire fuselage is costly and not always possible, open fuselage sections are used with appropriate stiffness on both open ends as boundary conditions to simulate the entire fuselage behavior as accurately as possible.

Usually, crash tests for aeronautical structures are dropped purely vertically, as explained in Section 2.1.1. However, the setup can present changes in roll, pitch, and yaw angles when setting the test up. The variations in yaw angle do not contribute to the loading of the fuselage structure [18], but a small angle variation in either roll or pitch can introduce a horizontal velocity and change the behavior of the structure notoriously. In such cases, stabilization is needed to reprehend the pure vertical impact (see Figure 2.8).

During a test, instrumentation like high-speed camera videos and accelerometers are used to monitor if the survivable volume is maintained or if the acceleration peaks are within human tolerance when reaching the cabin to comply with the injury risk factors [18]. The accelerometers are widely used and placed in critical parts like the frame, stiffeners, or the sub-floor junctions (see example on Figure 2.9). Strain gauges can also be added to the sub-floor and cabin to monitor deformation and motion, respectively [18].

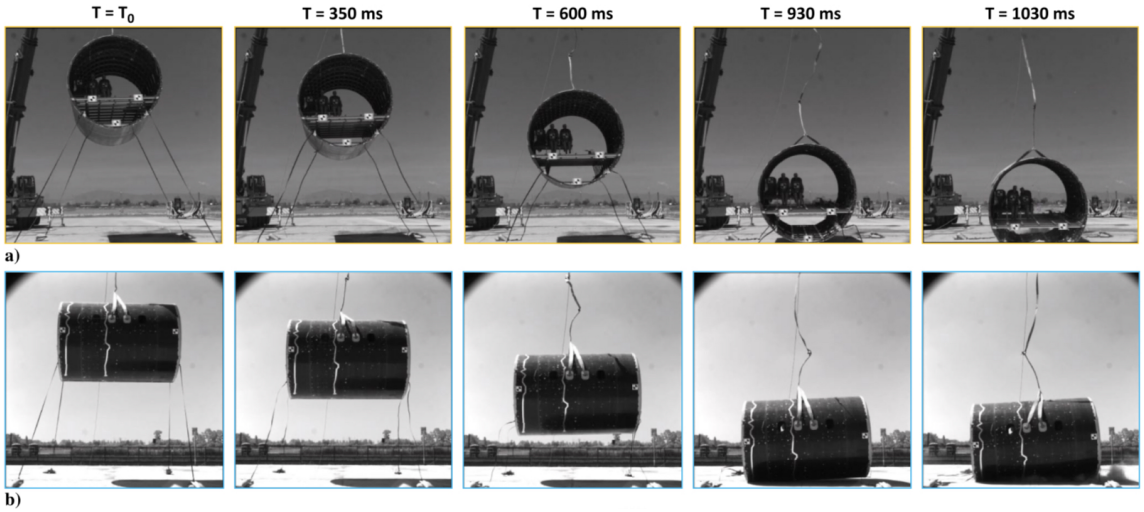

Figure 2.8: Drop test sequence from the front view (a) and lateral view (b). Figure taken from p.481 in Di Palma et al. [17].

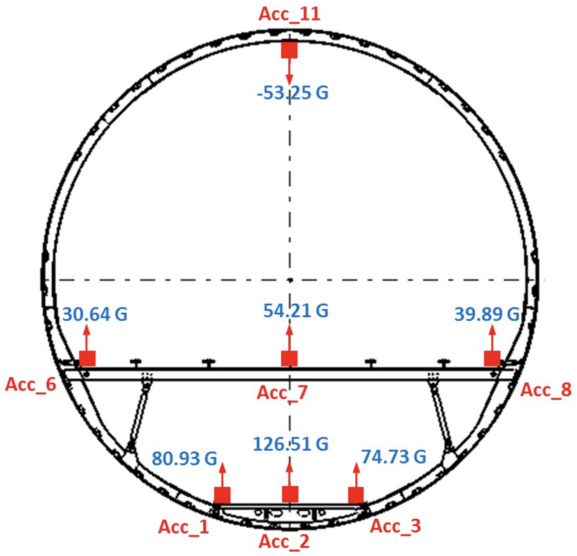

Figure 2.9: Accelerations registered from piezo-resistive accelerometers. Figure extracted from p.484 Di Palma et al. [17].

2.3.2 Composite structures tests

In composite structures, before the dynamic tests, quasi-static tests need to be performed to characterize the material in the linear elastic region. Most composite structures are heterogeneous, with different mixing ratios and reinforcement placement, as the material is designed altogether with the component design. This means that each composite can present different capabilities and properties in an impact. Hence, by exposing them to quasi-static compression tests for characterization, their material's constitutive laws are set for dynamic tests [32, 36]. Dynamic tests for composites can be done in a drop test machine, such as Bisagni's experimental investigation at Politecnico di Milano in 2009 for tubes made of different composite materials [37]. The tubes present a 45° chamfer at their top to cause high stresses and start the crushing at its tip, presenting then a stable and progressive deformation, despite these being dropped from a 6.5 m height to achieve the impact velocity of 10 m/s. The progressive deformation leads to a stable failure on the tube that can save the structure from catastrophic damage, large peaks of force and low mean crushing force [37]. The stable failure modes found in Bisagni's study, and therefore kept as a reference for the remaining part of the thesis, are the tearing, socking, splaying, and micro fragmentation modes (see Figure 2.10). The tearing mode simulates flower petals deformation, where an inside portion of the wall bends inwards but the outside one does it outwards. The socking mode presents several folds on the crushed structure, where the inner

and outer walls stick together. The splaying mode separates the individual tows of fibers from the composite and divides these further due to matrix cracking. And finally, the micro fragmentation failure mode turns the crushed area of the tubes into a dusty material [37].

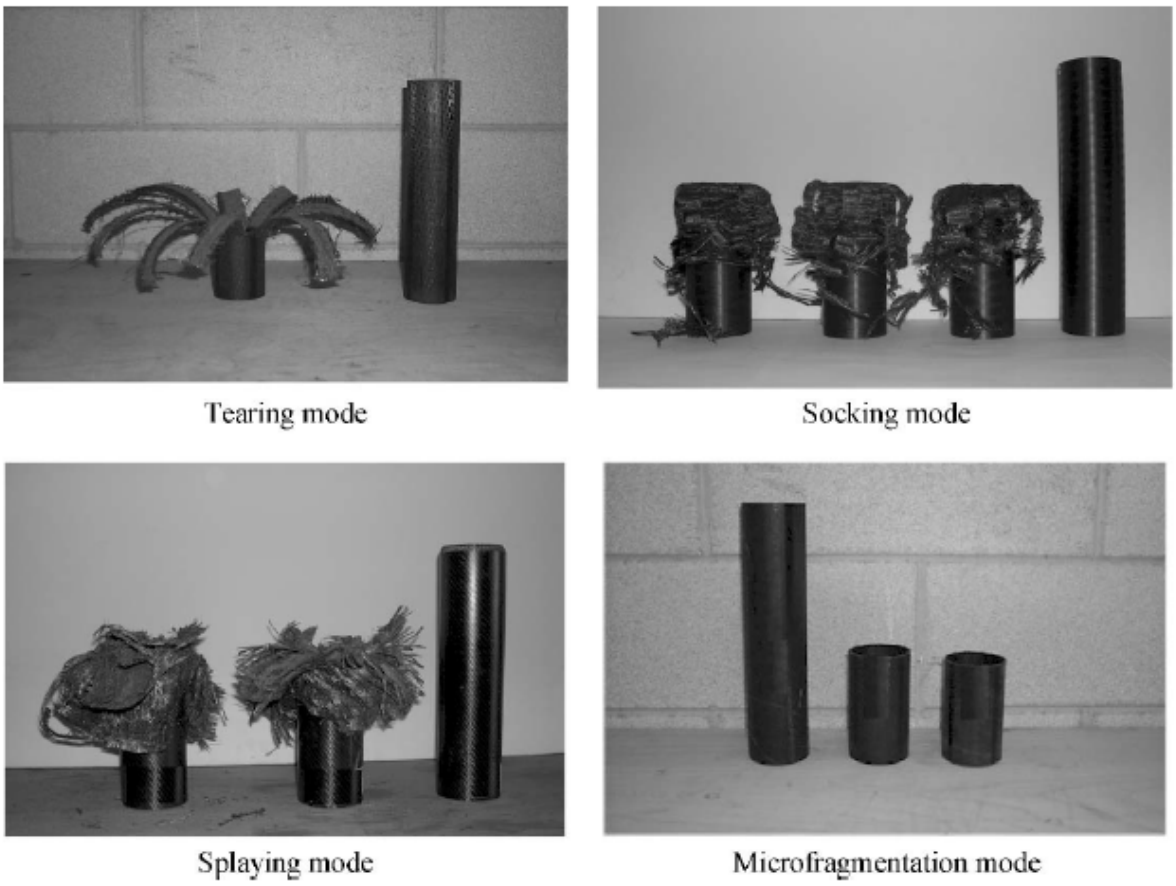

Figure 2.10: Composite tubes, stable failure modes upon crushing. Image taken from p.367 from Bisagni's experimental study at Politecnico di Milano [37].

It is common for composite components, however, to present defects that are not easily detectable and have repercussions on the test outcome if the manufacturing process has no monitoring to control the procedure [31]. The consequence of this is a disagreement with the numerical tests. Hence, the outcome checks. Non-Destructive Techniques (NDT) can be used to check the presence of defects and validate the test results. These techniques are useful to assess the crash fracture after the tests to search for debonding or cracks in composites [12]. However, incipient cracks are hard to find, so smart materials in smaller scales like a piezo-impedance in carbon nano-tubes (CNT) help with that as they are sensitive to deformation.

Upon the absence of defects on the composite structure, clamping conditions or bending over the weakest axis of your geometry can also affect composite crashworthiness [27]. The same monitoring used in aeronautic structures can verify in composites how much damage is caused to the composite structure and the source of it. A first example can be found in Bisagni's experimental investigation with composite tubes, whose tests are recorded using a 1000 fps high-speed camera to see the crushing evolution. Another example of the same instrumentation being applied to composites is using accelerometers of 200 g full-scale on six fabric tubes and three UD ones to study their crash resistance [36]. In this case, Bisagni et al. article explain that the registered acceleration values are filtered afterward using a CFC 180 filter at 180Hz, whose post-processing allows the calculation of crashworthiness assessment indicators: F_{peak}, F_{mean}, EA, SEA, CLE, SE, residual height and residual weight [36]. Bisagni's experimental work at Politecnico di Milano also uses this filtered post-processing from the incremental encoder and piezoelectric accelerometer retrieved data [37].

2.4 Design and optimization

Structural crashworthiness can be evaluated using the indicators from Section 2.1. These indicators can be improved by modifying components of the structure, whether it is by changing their geometry, size, material, or by simply adding components to the existent bunch. These changes can make the structure deform progressively and absorb more energy (providing better crashworthiness metrics) without the need to redesign it fully. There are many ways to do so, and this section presents some proposals from literature to improve the crashworthy behavior of aeronautical and composite structures. Each proposal includes, when available, the following: components to be optimized, the parameters involved in the optimization process and how this one is done, the sensitivity parameters of the study, and the difficulties or drawbacks that can be found in the process.

2.4.1 Design improvements in aeronautical structures

In aircraft, structural optimization focuses on improving the crushing capabilities of those components that contribute the most to their crashworthiness, which are mostly placed on the fuselage's sub-floor as mentioned in Section 2.1.1.1. Design improvements on these can consist of adding extra materials to damp the structural response, such as cargo area fillings to dissipate the impact energy [19]; or redesign the existent sub-floor through the implementation of optimization algorithms and metamodels even [38, 39, 40, 41].

When adding materials or components to aid with the energy absorption of the fuselage, the luggage from the cargo area, foam or honeycomb material blocks, tension absorbers, and a sine-wave beam are examples of what can be added to the structure to improve the crashworthiness capabilities of an aircraft sub-floor [19, 26, 33, 35, 42, 43].

With the sufficient amount of luggage in the cargo area, the deformation and damage of the structure at the bottom of the fuselage are still present but the luggage impedes this one to reach the cabin. Therefore, the luggage acts like an absorbing "filling material" or a damper [35]. The main disadvantage is that the minimum amount of luggage to perform well on impacts cannot be guaranteed on every commercial flight because it depends on the number of passengers on board, the amount of luggage they carry, or the type of aircraft used as a fleet. In small narrow-bodied aircraft, the luggage is loose in the cargo compartment, so the same effect may not take place [18].

When filling material blocks in the fuselage sub-floor like foam or honeycombs, the structure absorbs the energy and impedes the damage to reach the cabin, similarly to the luggage case. Hexagonal honeycomb and lower clip-plate devices change the bottom of the fuselage's cargo floor to absorb more impact energy [33]. The downside of this proposal is that the design of the lower clip-plate affects the fuselage's crash behavior. If the clip is either too thin or much more rigid than the honeycomb layered device, the impact forces are kept high and the fuselage does not meet the structural requirements from Section 2.1.1. Putting some foam filling in the cargo area, or between the cargo floor and the outer skin of the cargo area also increases the amount of energy absorbed by the structure [19, 42]. The fillings, however, take a lot of space from the sub-floor, so smaller crash devices are found to be a useful alternative. These devices can be tension absorbers to minimize the load magnitudes reaching the cabin, alongside its intrusion and risk of injuries [26]. Nonetheless, adding a crash device to the sub-floor does not exempt redesign in its surrounding structure for it to fit in with the aid of additional supports or a different positioning [43], like the sine-beam placement under the frame from Figure 2.11. Nonetheless, in some cases, the existing structural redesign can be done to compensate for the added mass from the fillings and crash devices.

Figure 2.11 shows that single shell structures' position reduces the damage in the frame and increases the SEA from the aluminum structure. Hence the skin and a plate placement above the sine-wave beam to improve its crushing force resistance, apart from maintaining the cargo volume capacity and leaving space for struts to limit the frame deformation. An extensive analysis is needed to find the best strut design for a given sub-floor configuration to withstand survivable impacts. The resulting strut design from Ren et al. analysis is a single shell without holes [43]. Xue et al. present that the first acceleration peak magnitude can be reduced by using foam filling and also, by reducing the thickness of the cargo floor supports [19]. Their thickness can be reduced in magnitude by weakening the struts or generating stiffer frame-strut intersections. Therefore, a

soft strut is wanted to allow deformation but it has to be stiff enough to limit structural interference to prevent further deformation for the primary airborne frame. Something similar happens to the cargo floor supports, which present asymmetric deformation when too weak, absent, or rigid. Weak or absent cargo supports lead to a bound first peak load while increasing the second one. And the other way around when the supports are too rigid or strong [19].

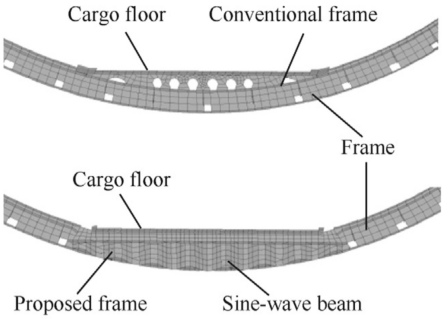

Figure 2.11: FEM of bottom structure: conventional VS proposed. Figure taken from p.405 in Ren et al. [43].

The redesign of the existent aeronautical structure can sometimes be more complex than repositioning or changing the thickness of a component by trying several values, which has implemented optimization algorithms very popular, especially when coupled with large numerical models. By implementing these, the computational cost can rise but the optimal solution can be reached more precisely. In some cases, the use of a singular algorithm is not worth it because of the computational cost this one implies, so the addition of a metamodel is done to train and generate a parallel structure that leads to a converged solution faster.

Woodson et al. work present an example of how the GA is used as a stand-alone optimization algorithm to get an optimal graphite-epoxy frame design. The GA does not require derivatives' evaluation, can study non-convex design spaces, and handle both continuous and discontinuous design variables, which is not possible in gradient algorithms [38, 44]. This makes the GA a suitable optimization algorithm for non-linear behaviors like crashes, despite it having a large computational cost [44, 45].

The basis of the GA is Darwin's principle on the survival of the fittest individual, whose characteristics are stored in chromosome strings. Each chromosome string is made of genes, which take the values of the stated design variables. If four genes are assigned to the first design variable and three for the second one, the chromosome string is seven genes long and represents an individual. Or a graphite-epoxy frame design in Wodson et al. [38]. The idea is that the design variables evolve from one generation to the next simulating biological processes of selection, reproduction crossover, and mutation [38, 44]. The last two with associated probabilities. Before the selection process, the fitness function maximizes the goal of the optimization and serves as a filter to get the fittest individuals selected for reproduction. Those who do not meet the requirements are usually constrained by adding to their fitness function a penalty, so they are disregarded as fit individuals in the selection process and do not pass on to the next generation. Reproduction crossover generates new individuals by exchanging information between the fittest chromosome strings. A no-twins rule is usually set to have unrepeated individuals within the same generation [38]. Finally, the mutation probability is relatively low to mimic the biological behavior of genetics, and its gene variations depend on the user's setup.

The end of the optimization takes place when reaching a maximum number of generations or when the same fittest individual has been chosen repeatedly for many iterations. The determination of how many iterations must be used for convergence purposes requires some analysis as well because when the GA converges, the changes between generations are less over time but the computational cost increases. Therefore, the optimal result must be found within a margin where the computational cost is not too high [38].

Wodson et al. particular case aim to maximize the EA of the graphite-epoxy frame design by using it as the algorithm's objective function [38]. This goal is to be reached upon a maximum load constraint, to bound the loads and accelerations within human tolerance. To compute the EA objective function, the algorithm needs the support of a numerical FEA to do so. In this case, a Vaslov-type curved bar element extended is used to

include the composite structure behavior in the algorithm (p.370 in Woodson et al. [38]).

The design variables considered are the stacking sequence of the composite frame and its cross-sectional dimensions. Both variables are discrete, which means that the EA function is non-linear and discontinuous on them [38]. The sequence variable is optimized first to get the desired selective ply-by-ply degradation model in the laminate. Then, the dimensions of the I-beam cross-section frame are optimized, using a weight penalty constraint for the chosen sequence when needed to avoid the combination from becoming an optimal solution [38]. This compensates for the limitation on ply orientations for the stacking sequence and size of each frame's branch, which can lead to a weight addition on the structure.

Kim et al. rotorcraft's fuel tank and Lanzi et al. helicopter sub-floor projects introduce the Artificial Neural Networks (ANN) metamodel coupling into the optimization process to improve the crashworthy design of their respective structures [39, 40]. ANN provides a global approximation to optimize any complex optimization problem, not only for structural purposes. These use their accumulative experience to solve optimization problems thanks to them performing parallel simple operations, sometimes called sub-systems from the network [40, 46]. ANN have a basic unit called a neuron, which receives an input and transforms this one into an output with the help of an assigned transfer function [47]. The neurons are present in all the layers that constitute a multi-layer perceptrons (MLP) network, which is the most common ANN to use with several hidden layers (see Figure 2.12). The input layer receives external inputs and transforms this through the neurons to send them to the adjacent hidden layers, which transform the weighted values from each neuron further to obtain the output values of the network [40]. To achieve this, ANN use first a finite training set of data, typically coming from a numerical FEA, where the input and output values of the network are known. Then the transfer functions and neuron weights are modified through an input-output mapping to match the known values and generate the ANN experience, making it capable of solving similar optimization problems afterward.

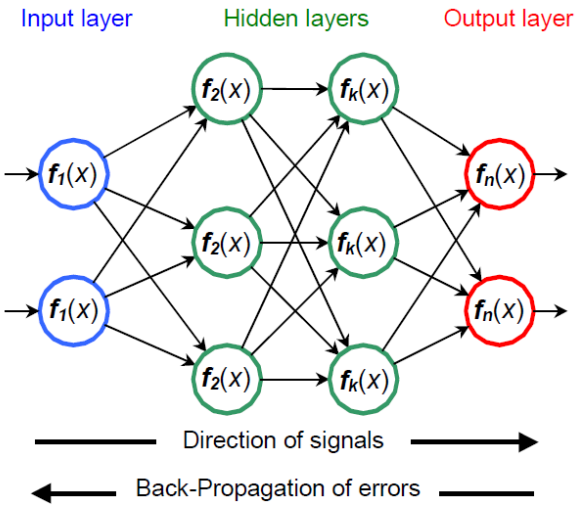

Figure 2.12: Structure of a BPNN. Figure from p.4 in Lanzi and Bisagni [47].

The way the training set operates throughout the network layers depends on the type of ANN used. For the rotorcraft's fuel tank and helicopter sub-floor optimization, their ANN use the back-propagation learning rule [39, 40, 41]. The typical architecture from a back-propagation neural network (BPNN) is shown in Figure 2.12. This learning condition uses the known output values to change the intermediate neural transfer functions and weights and minimize the root mean squared error (RMS) as it goes backward (p.97 Lanzi et al. [40]). Regarding the difficulties presented in BPNN, the training set has some difficulty when considering non-convex or irregular design spaces, and also considering equality or inequality constraints on the design variables of a crash optimization problem. To overcome this, hypercube sampling (LHS) is one of the methods used to allocate the training set design parameters randomly throughout the design domain, from where they change locations until reaching a homogeneous dispersion within it [40, 46]. In the case of the helicopter sub-floor sequential multiobjective optimization, the training set data points are changed in position throughout the design domain by making their distances as greater as possible [40, 41]. The called *efficient*

resilient back-propagation training BPNN method used on the rotorcraft's fuel tank is, does the homogenization by assuming that all neurons use a Sigmoid function to exchange the data between layers [39].

The application of BPNN into the rotorcraft's fuel tank optimization aims to minimize the weight of this one while maximizing the EA. In this case, the topology of the structure is changed to achieve the optimization goals, so the shape of the tank is the optimization objective. The improvement in EA should reduce the stress values exerted on the tank due to the crash conditions, and these stress values vary depending on the design variables, which are the inclination angle of the tank's bottom surface and the fitting interval of its top surface [39]. The results of the optimization indicate that the tank's initial weight is reduced in the final optimal shape, along with the fitting interval in the upper surface of the tank and the consequent calculated optimization angle for the bottom inclination. The decrease in the fitting interval is responsible to reduce the impact load influence through the upper central region reinforcement in the tank, which means that the structure absorbs energy better than before.

Bisagni et al. proposed to globally optimize the aluminum helicopter's sub-floor in size and topology with a combination of ANN and either gradient Sequential Quadratic Programming (SQP) or the probabilistic GA optimization algorithms [41]. Both algorithms are suitable for non-linear optimizations, but while the GA allows to formulate every problem as unconstrained and add a penalty instead, the SQP algorithm has a different approach to working with the constraints. SQP formulates quadratic sub-problems based on a Lagrangian approximation function, which simplifies the constraints during the optimization process. The non-linear constraints are linearized, and the bound constraints are expressed as inequalities [41]. The results from both algorithms being implemented on ANN show very similar results, making them both reliable enough to proceed with the size and topology optimization [40].

Lanzi et al. article presents that the helicopter's sub-floor is assumed to be a simplified additive model divided into components to study its crash performance [40]. The parts considered are the intersection elements of the sub-floor, the keel beam elements, and the lateral panels (see Figure 2.13). These last ones' contribution to crashworthiness, however, is considered negligible when compared to the keel beam elements. The remaining parts (intersection and keel beam) are studied separately and added afterward as a whole [40]. All the input data to the BPNN come from the finite element analyses of the parts separately using the commercial code of PAMCRASH, and assuming a constant impact velocity of 7 m/s.

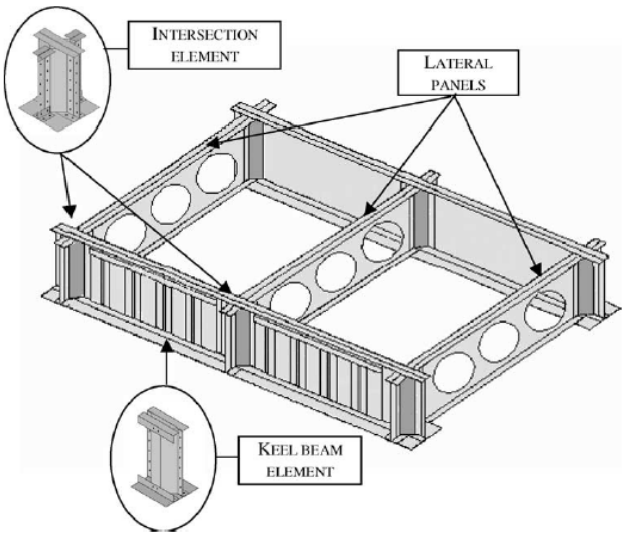

Figure 2.13: Helicopter sub-floor, differentiated parts. Figure from p.103 in Lanzi et al. [40].

The intersection elements from Figure 2.13 use the BPNN and GA algorithm to obtain as outputs the load-time curve, and the maximum and mean forces of the different designs [40]. The design variables for these elements are the angular elements' thickness and position, the number of vertical rivets, and other panels' thicknesses from each intersection. For the longitudinal keel beam elements, only three design variables

are considered: the thickness of the webs and the width and length of the trapezoidal boxes [40]. With the minimal mass and maximum EA in mind as an aim to optimize the parts' design, the total forces of the subfloor are found to be well approximated with the sum of the forces returned in each component optimization. The load-time curve's behavior is analog to the addition of the forces, but the validation must be done with a complete numerical simulation.

2.4.2 Design improvements in composites

This section presents several ways to improve crashworthiness behavior in composites by enhancing the energy absorption capability of the structure. In the case of composites, however, their brittle nature, reinforcement, and construction play an important role in crushing. Isaac and Ezekwem talk about the influence of the cutting angles in the SEA of CFRP thermoset composites [12]. In tubular designs, circular cross-sections usually get a higher SEA. Nonetheless, its diameter must increase and its wall thickness must reduce to absorb more impact energy.

Boria and Belingardi state in p.345 that woven fabric in-plane symmetry is usually preferred to withstand better impact loads, despite being a bit less efficient than UD fiber reinforcement [32]. Additionally, when using a woven fabric, a small increase in the thickness can also help enhance the energy absorbed. Regarding the composite construction, sandwich panels and corrugated sandwich structures enhance EA and give higher strength to the component than regular composites. Isaac and Ezekwem warn about the tube's thickness affecting the SEA and CFE as well. The smaller the thickness, the lower these metrics are [12]. Therefore, Isaac and Ezekwem propose nanoparticle reinforcement as an energy absorption enhancer in fibrous materials. The advantage is that these provide biodegradable behavior, low density, high specific stiffness, and mechanical strength [12]. Graded composites, fillings, and multi-cell composites are some of the alternatives to composite construction change. The grading of a composite can be an axial change in thickness that reduces the peak loads exerted on the structure, which is applied to a tube along its thickness [12]. Isaac and Ezekwem work on graded tubes along with their thickness and conclude that the use of fillings like foam or honeycomb can also increase the SEA of the structure. Due to graded composites still being under development, Isaac and Ezekwem and Zhang et al. use multi-cell composite structures as another way to improve their crashworthiness capabilities [12, 16]. Isaac and Ezekwem use graphite in multi-cell composite parts for automotive applications, which increases their performance in energy absorption [12]. Zhang et al., however, insist on the use of fillings for the tube's cross-section cells to present more folds in the surrounding walls upon deformation. That way, the folding wavelength is reduced and causes the outwards buckling to increase the time that the structure is absorbing energy (section 4.1 in Zhang et al. [16]). At this point, an optimization algorithm is implemented to find the best filling distribution on the multi-cell tubular structure. The multiobjective particle swarm optimization (MOPSO) is chosen for the purpose, as it is fast converging and efficient. The objectives of the algorithm enclose a minimization in mass and F_{peak}, and a maximization of SEA. The design variables introduced to accomplish these are the tube's wall thickness T, the honeycomb filling wall thickness (t), and the foam density (ρ). The outcome of the optimization algorithm considers honeycomb as the better filling for a higher SEA.

The application of optimization algorithms in composites is very common for structural purposes, as seen in the previous sub-section for aeronautical structures, and many of them are destined for topology optimization [48]. The hybrid thermoplastic composite bumper beam from Kim et al. uses a variation of the GA for its global optimization, called the micro-genetic algorithm (μGA). This variation has a faster-accelerated convergence and distinguishes better what is the global optimal solution for the structure [31]. The objective function of the hybrid GFRP/CFRP bumper beam weight is to be minimized while keeping the intrusions and deflections bound to human tolerance as constraints. Both intrusions and deflections depend on the discrete design variables, which are the thickness of each part of the bumper beam from Figure 2.7: the thickness of the rib, the top and bottom flanges for the three parts of the beam, plus the thickness of the beam reinforcement. That makes chromosomes of ten genes long, with a thickness value in each of them. The chromosome or individual is evaluated and selected just like in the GA explained in Section 2.4.1. The only difference is that μGA considers a smaller population to operate the fittest principle of survival and the first generation is chosen randomly. That may cause the algorithm to take longer to converge, as random smaller populations may not have given the best children in crossover nor produce big changes in mutation. Therefore, crossover reproduction and mutation are in a loop until they provide an acceptable outcome for convergence [31]. The

downside of the chosen algorithm is that its similarity to the original GA makes it also depend on the FEA outcome to get the fitness values computed every loop. Hence, the computational cost is high.

Chapter 3

Preliminary analyses: Coupon tensile finite element analyses

The goal of this chapter is to get familiar with the numerical software of LS-DYNA. To do that, a simple tensile analysis is performed in LS-DYNA to learn how to formulate a simple finite element analysis for aluminum and composite plates. The aluminum plate is used evaluated first, as its material characterization in LS-DYNA is less complex than for composites. After that, the composite plate serves as a transition between the aluminum tensile analysis and future crushing analyses of this thesis.

3.1 Common setup for the tensile analyses

The tensile analysis exerted on the isotropic aluminum and the anisotropic composite plates, which share the same dimensions, elements' formulation, and boundary conditions. The dimensions of the specimens are 200 mm x 70 mm x 1.3 mm, following the ASTM standards' designation D3039-08 [49]. To model these specimens in LS-DYNA, the mesh can be assumed to be two-dimensional, and then assign a very small thickness to the elements on the mesh. Regarding the elements of the mesh, these are modeled using a 2D Belytschko-Tsay shells formulation, which is the default and advised formulation for these types of elements in LS-DYNA. Their orientations are aligned with the tensile load applied on the X-axis, as shown in Figure 3.1, and their normals face the positive Z-axis.

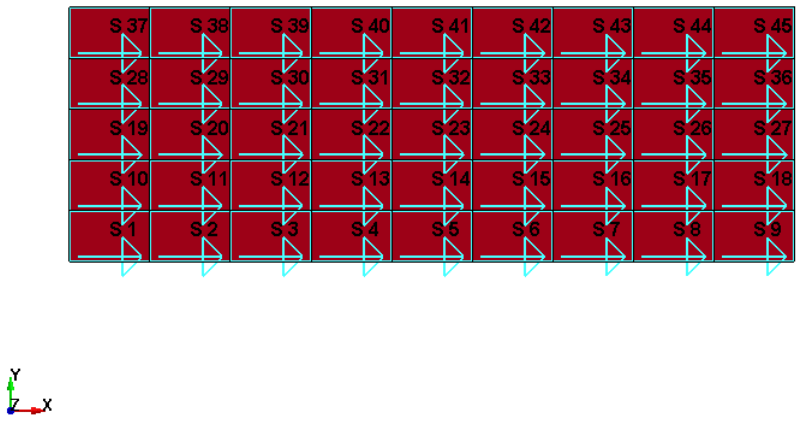

Figure 3.1: Specimen(s) elements' orientations aligned with the applied tensile load in the positive X-axis.

As mentioned before, the boundary conditions are common to both specimens. The rest is particular for each case of study. Taking as reference the specimen from Figure 3.2, the left end with nodes 1-51 has a fixed boundary condition applied to it. That boundary condition uses the LS-DYNA keyword *BOUNDARY_SPC_SET* in which a set of nodes 1-51 are deprived of their degrees of freedom, both for translation and rotation movements. On the right edge from Figure 3.2 specimen, two boundary conditions are applied. The

first condition defines a displacement for the nodes 10-60 to introduce a controlled tensile loading through a displacement curve in the X-axis. Apart from that, to limit the displacement solely to the X-axis, an additional *BOUNDARY_SPC_SET* keyword is added as a boundary condition to limit the degrees of freedom in all rotations and translations in the global Y and Z axes.

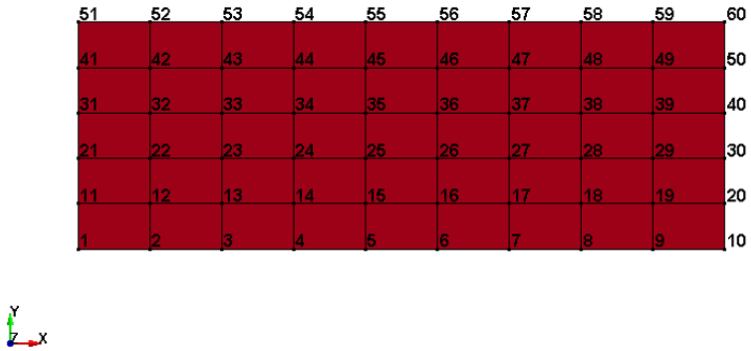

Figure 3.2: Specimen(s) assigned nodes.

3.2 Aluminum coupon tensile analysis

This section explains the particular case of study for the aluminum plate preliminary tensile analysis. The different material setup, results, and post-processing are discussed in the following sub-sections.

3.2.1 Material of the coupon

The material of the plate is in this case the aluminum alloy AA6101-T6 [50]. This material is modeled for the tensile analysis using the *MATERIAL_ELASTIC* keyword in LS-DYNA to evaluate the elastic region of the loading. In this case, the AA6101-T6 properties relevant to the material's keyword from LS-DYNA are the ones shown in Table 3.1.

Elastic property	Value	Units
Density (ρ)	$2.7 \cdot 10^{-6}$	kg/mm^3
Young's modulus (E)	70	GPa
Poisson ratio (ν)	0.33	-

Table 3.1: Elastic properties of the aluminum alloy AA6101-T6 used in the tensile analysis [50].

3.2.2 Results and post-processing

The results from the tensile simulation are reviewed in this section so it is possible to know whether or not the analysis has been modeled correctly. To do that, the resulting force-displacement graph from LS-DYNA results must be turned into a stress-strain curve so that the Young's modulus can be calculated from it. That way, if the modulus calculated is close to the one shown in Table 3.1, the model has been designed correctly and provides the right results. There are two ways to calculate the Young's modulus in this case, using a global or a local approach.

3.2.2.1 Global approach

The global approach starts by generating the force-displacement in LS-DYNA. The displacement is registered in the X-axis as indicated in the analysis setup keywords, while the force is obtained by adding the registered values from each node on the loaded side (nodes 10-60). The resulting graph is shown in Figure 3.3.

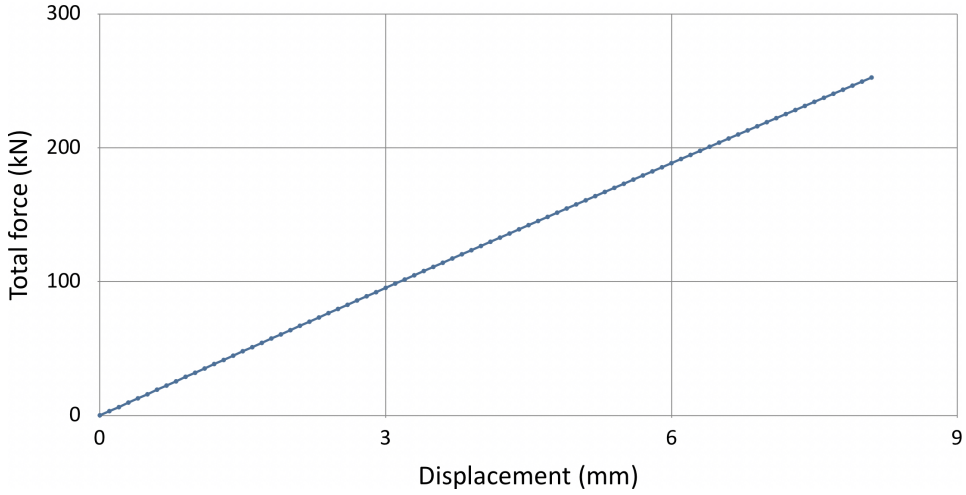

Figure 3.3: Force-displacement graph resulting from the tensile analysis in the aluminum plate.

The force data from Figure 3.3 is used along with the plate's cross-section initial area (A_0) to calculate the stress (σ) using Equation (3.2) and Equation (3.1), respectively. The displacement of nodes 10-60 and the initial plate length ($L_0 = 200\,mm$) are used to calculate the strain (ε) using Equation (3.3). The resulting stress-strain curve is shown in Figure 3.4.

$$\sigma = \frac{\text{Force}}{A_0} \tag{3.1}$$

$$A_0 = \text{width} \cdot \text{thickness} = 70\,mm \cdot 1.3\,mm = 91\,mm^2 \tag{3.2}$$

$$\varepsilon = \frac{\text{Displacement}}{L_0} \tag{3.3}$$

The slope of the linear graph from Figure 3.4 is calculated using a calculation sheet from Numbers software. The resulting slope corresponds to the calculated Young's modulus and validated the simulation. Figure 3.4 presents the resulting modulus of 68.50 GPa, which is quite close to the 70 GPa set in Table 3.1, with a 2.15% of relative error between them. The relative error is concluded as small enough to consider the analysis well conducted.

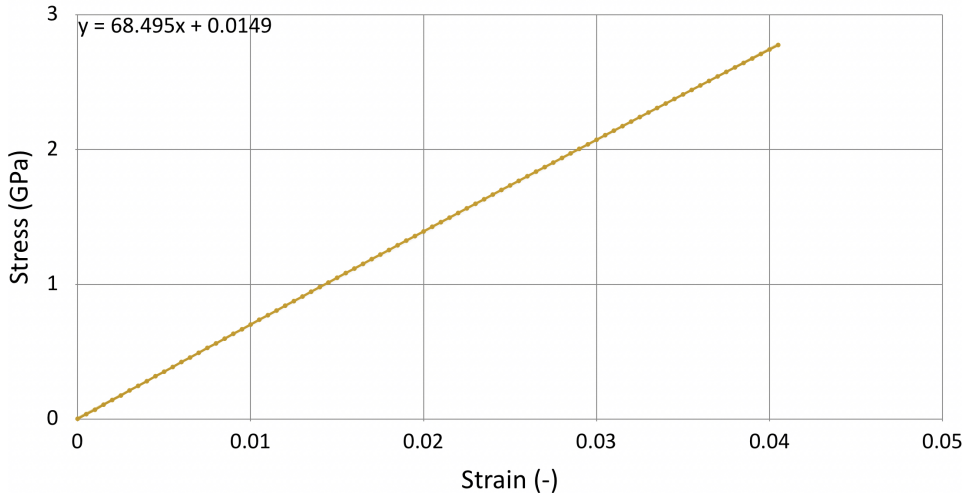

Figure 3.4: Stress-strain curve transformed from the aluminum plate's force-displacement graph.

3.2.2.2 Local approach

The local approach consists of taking the stress and strain values from the middle of the aluminum plate. The keyword *DATABASE_ELOUT* in LS-DYNA allows the program to register these from the central element of the specimen (element 23 from Figure 3.1). The stress and strain values taken from element 23 of the plate build the stress-strain curve from Figure 3.5.

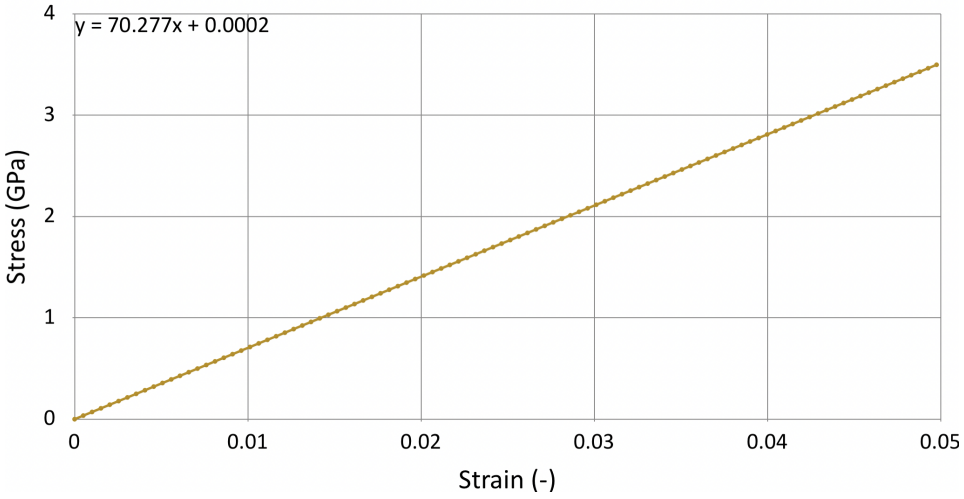

Figure 3.5: Tensile stress-strain curve resulting from element 23 of the aluminum plate.

Figure 3.5 also shows the equation of the curve, whose slope refers to the resulting Young's modulus of 70.28 GPa from the simulation. The relative error is again computed with respect to the input value from Table 3.1, resulting in a 0.4% relative error. This value is once even lower than the one gotten when using a global approach validation. Hence, the simulation is considered well set up and conducted.

3.3 Composite plate tensile analysis

In this section, three different composite plates will undergo tensile analysis. Their setup differs from the isotropic plate only when defining a stacking sequence in each plate, and the material model used to define the composite IM7/8552 properties [10]. The plate is defined using the keyword *PART_COMPOSITE* in LS-DYNA, where the stacking sequences are indicated per case of study [8]:

$$\text{Longitudinal layup: } [0_4]_s$$
$$\text{Transverse layup: } [90_4]_s$$
$$\text{Quasi-isotropic layup: } [0, 90, \pm 45]_s$$

Each layup represents the composite plate's plies' orientations in degrees. Each ply has assigned an arbitrary thickness (t_{ply}), based on the total plate thickness of 1.3 mm (t_{plate}) and the total number of plies in the plate (N_{plies}):

$$t_{ply} = \frac{t_{plate}}{N_{plies}} = \frac{1.3\,\text{mm}}{8\,\text{layers}} = 0.1625\,\text{mm} \tag{3.4}$$

MAT_058_LAMINATED_COMPOSITE is the chosen material model to represent the composite IM7/8552 properties [9, 10]. The properties introduced in the composite material model are shown in Table 3.2 [10]. The rest of the properties to define the loading response of the plate are presented separately in Table 3.3, which includes features such as unitless factors that limit the load after a peak force, regardless of the nature of the loading (tension in this case) [9].

Property	Value	Units
Density (ρ)	$1.58 \cdot 10^{-6}$	kg/mm^3
Longitudinal Young's modulus (E_A)	165	GPa
Transverse Young's modulus (E_B)	9	GPa
Transverse Poisson's Ratio (ν_{BA})	0.0185	-
Longitudinal Shear modulus (G_{AB}, G_{CA})	5.6	GPa
Transverse Shear modulus (G_{BC})	2.8	GPa
Maximum longitudinal tensile strain ($\varepsilon_{11,T}$)	0.01551	mm/mm
Maximum longitudinal compression strain ($\varepsilon_{11,C}$)	0.011	mm/mm
Maximum transverse tensile strain ($\varepsilon_{22,T}$)	0.0081	mm/mm
Maximum transverse compression strain ($\varepsilon_{22,C}$)	0.032	mm/mm
Maximum shear strain (GMS)	0.05	mm/mm
Longitudinal tensile strength (X_T)	2.56	GPa
Longitudinal compression strength (X_C)	1.59	GPa
Transverse tensile strength (Y_T)	0.073	GPa
Transverse compression strength (Y_C)	0.185	GPa
Shear strength (S_C)	0.09	GPa

Table 3.2: Properties of the IM7/8552 composite introduced in LS-DYNA *MAT_058_LAMINATED_COMPOSITE* material model [9, 10].

Property	Value	Units
Longitudinal tensile loading limit factor (SLIMT1)	0.01	GPa/GPa
Longitudinal compression loading limit factor (SLIMC1)	0.375	GPa/GPa
Transverse tensile loading limit factor (SLIMT2)	0.1	GPa/GPa
Transverse compression loading limit factor (SLIMC2)	1	GPa/GPa
Shear loading limit factor (SLIMS)	1	GPa/GPa
Softening (SOFT)	0.57	-

Table 3.3: Additional properties to tune the loading responses in LS-DYNA *MAT_058_LAMINATED_COMPOSITE* material model [9].

The overall goal for this anisotropic plate simulation is to validate this one by calculating the elastic modulus of the two local axes, which require the activation of *NEIPS* variables #10 and #11 in *DATABASE* keyword to get the local strain values. *DATABASE_ELOUT* keyword is also used to get the stresses of the specimen to build the stress-strain curve and calculate the modulus from it. The longitudinal layup is used to calculate the Young's modulus correspondent to the global X-axis in the direction of the fibers, while the transverse one calculates the modulus for the global Y-axis. The quasi-isotropic layup is added to verify the properties using the locally probed stress and strain values from LS-DYNA.

A local approach is used, resembling the isotropic procedure, as it gives a smaller relative error, providing more accurate results and saving intermediate steps.

3.3.1 Results and post-processing: Plate with longitudinal layup

This sub-section presents the results obtained for the composite coupon tensile analysis using the $[0_4]_s$ layup, whose plies' orientations align with the mesh elements' orientation and the load applied. This means that the fibers and load are coincident with the global X-axis.

To get the Young's modulus from the X-axis, the stress and strain values are taken from the central element of the composite specimen (shell element 23). The linear part of the graph is shown in Figure 3.6, which gives the principal Young's modulus in global coordinates (E_x) through its slope. This procedure is repeated from the local approach taken in the isotropic plate.

As shown in the equation from Figure 3.6, the calculated modulus from the graph's slope is 164.38 GPa. Keeping in mind the value of reference of 165 GPa from Table 3.2, the relative error between the computed and

the theoretical value is 0.38%. For such a low value, the simulation setup is considered correct and provides accurate results with a relative error below 1%.

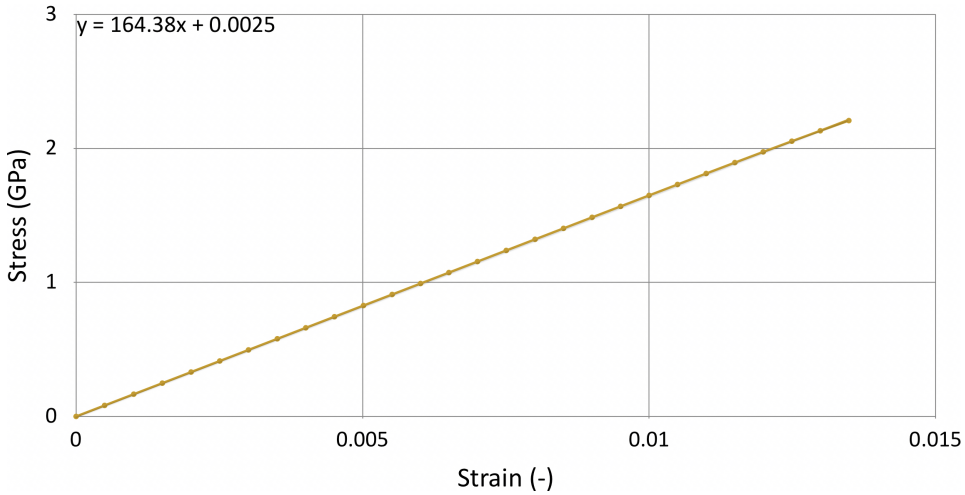

Figure 3.6: Linear part of the stress-strain curve. Values taken from shell element 23 in the X-axis of the composite $[0_4]_s$ plate.

3.3.2 Results and post-processing: Plate with transverse layup

This sub-section presents the resulting transverse modulus of the composite plate by using a tensile analysis applied to a $[90_4]_s$ composite. In this, case the plies' orientations are all perpendicular to the load and mesh elements' orientation, so the transverse modulus in the global Y-axis is to be validated.

In order to get the Young's modulus from the Y-axis, the stress and strain values are also taken from the central element of the composite specimen (shell element 23), just like in the previous case with a longitudinal layup. With the taken values, the stress-strain curve is generated. The linear part of the graph is shown in Figure 3.7, which gives the transverse Young's modulus in global coordinates (E_y) through its slope. This procedure is the same as followed in the isotropic plate's local approach and the longitudinal layup.

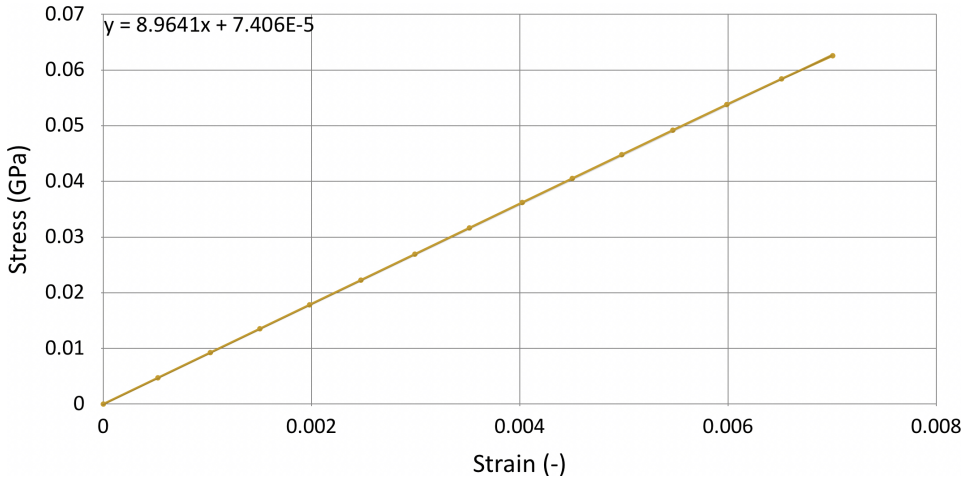

Figure 3.7: Linear part of the stress-strain curve. Values taken from shell element 23 in the Y-axis of the composite $[90_4]_s$ plate.

The resulting slope from Figure 3.7 gives a calculated transverse modulus of 8.96 GPa in the Y-axis. This value with respect to the theoretical 9 GPa from Table 3.2, gives a relative error of 0.4%. This makes the simulation correct as it presents accurate results.

3.3.3 Results and post-processing: Plate with quasi-isotropic layup

This sub-section presents the resulting modulus from the $[0, 90, \pm 45]_s$ composite plate's tensile analysis. Given the fact that the plies' orientations change in every ply, the stress and strain values taken are local and depend on each ply orientation (see Figure 3.8). All the probed values from this section are taken from the central shell element 23.

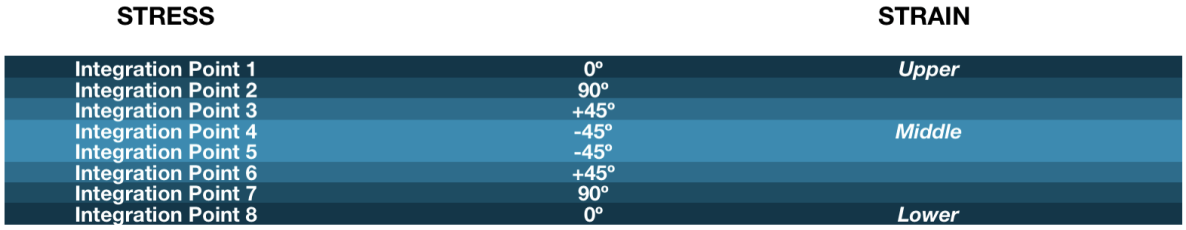

Figure 3.8: Scheme of quasi-isotropic composite plate, its integration points and strain plies. Scheme is not to scale.

Taking as reference Figure 3.8, each ply has one integration point, from which the stress values in the global X and Y axes are taken. In this local approach, the plies 0° and 90° are used as their principal local axes are coincident with the global X and Y axes, respectively. The strain values are registered for the upper, medium and lower plies of the plate, whose orientations are 0° and -45° due to layup's symmetry (see Figure 3.8). According to LS-DYNA registered values, the linear part of the principal stresses is equal for the plies with the same orientation, which also happens for the strains. Both the stress and strain values are taken using the *ELOUT* keyword. To generate the stress and strain curve for the global X-axis of the composite plate, the principal stress of the 0° ply is taken for Integration Point 1. The reason behind this resides in the principal axis of the 0° ply to coincide with the global X-axis of the plate. Following this trail of thought, the principal strain of the same ply is equal to its global X-strain and generates the linear part of Figure 3.9's graph. The E_x of the composite plate is taken from the curve's slope: 163.98 GPa. The relative error between the calculated slope and the value of reference (165 GPa) is of 0.62%. This matches the accuracy of the validated values for the previous sub-sections for the fully longitudinal and fully transversal composite plate orientations, making the simulation setup correct.

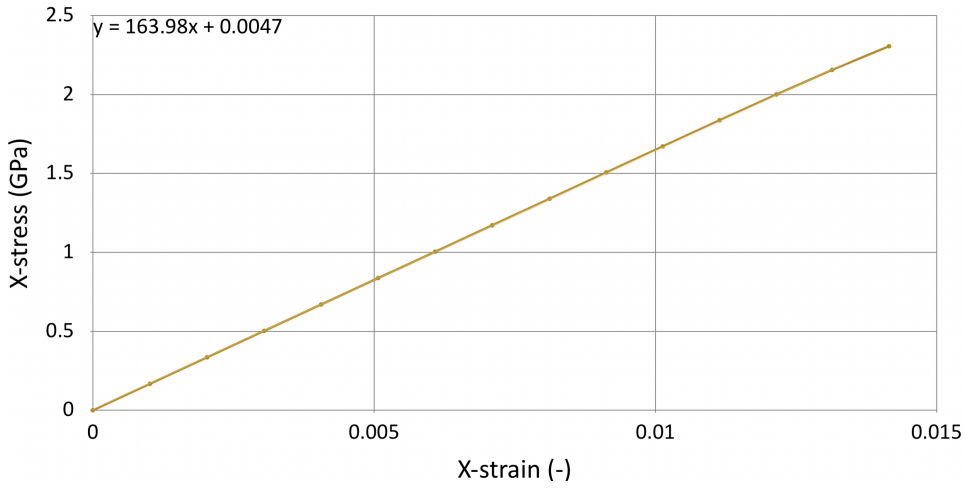

Figure 3.9: Stress-strain graph resulting from the probed values in the global X-axis of the composite's 0° ply.

To find E_y, the stress-strain curve generated in Figure 3.10 takes the principal stress of the 90° ply (Integration Point 2 or 7 from Figure 3.8), which aligns with the global Y-axis. The principal strain values from the second ply should be taken to validate the global transverse modulus. However, the strains, as mentioned earlier, are not registered for the second ply (see Figure 3.8), which leads to the hypothesis that the transverse strain (global Y-axis) from the first 0° ply should suffice for the modulus validation.

Seeing Figure 3.10, for a very small strain change in the X-axis of the graph, the maximum slope obtained

is 8.13 GPa. Keeping in mind that the reference value for the transverse modulus is 9 GPa, the resulting relative error is 9.64%. This error is too high when compared to the previous modulus validations and uniform layups. Therefore, the hypothesis that the Y-strain of the 0° can be used to validate the transverse modulus of the composite plate is proved wrong.

Thanks to the accuracy of the longitudinal modulus validation, the simulation is proved to be correctly set up. Nonetheless, one alternative to validate the modulus can require using the transverse Poisson ratio with the registered strains for the first ply. Otherwise, the composite modeling should be changed so the composite plate is modeled using several shell elements through its thickness instead of one. That way, the integration points for the 90° would provide the exact strain in the global Y-axis and validate the transverse modulus more accurately. This is not done, as this composite modeling formulation is more complex and out of the scope of this thesis. In future chapters, the composite tubes and struts are modeled using the simple single shell formulation from this chapter.

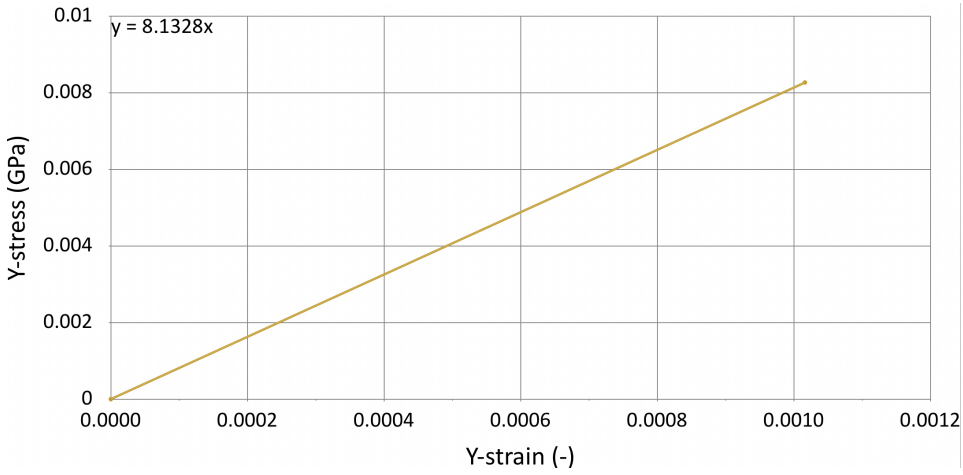

Figure 3.10: Stress-strain graph resulting from the probed values in the global Y-axis of the composite's 90° and 0° plies, respectively.

3.4 Computation time

The studied analyses in this chapter present a very simple setup, as explained in previous sections. When using the aluminum plate setup in LS-DYNA, there are no complex keyword cards, as even the material model requires only three elastic properties. This makes the simulation run fast in under a minute time. This is not the case for the composite plate analyses, since these present a more complex part definition and material model. The plate is defined as a composite part in LS-DYNA, in which every ply placement, orientation, and thickness is defined [8]. The material model is assigned to the composite part using material model *MAT_058_LAMINATED_COMPOSITE*. This material card adds complexity to the model by having additional inputs such as maximum stress and strains per failure in a simple linear elastic problem (see Table 3.2 and Table 3.3). When running the simulation, the computation time increases with respect to the aluminum plate and lasts between 4 and 8 minutes.

Chapter 4

Numerical crushing analysis of a square tube

This chapter presents the first non-linear crushing analysis of the thesis for a square tube. The following analysis is important as it gives the data of reference for future chapters. Chapter 5 uses this data of reference to check how the tube's crashworthiness properties change during its layup optimization. If these improve enough, the optimized crushing tube can go into a fuselage as a crash absorber in Chapter 7.

4.1 Numerical model

The crushing model generated in LS-DYNA uses as validation data the Charniaev et al. tube's crushing model and the published experimental data from tests 46B and 47B in the Oak Ridge National Laboratory's (ORNL) online's database [10, 51].

4.1.1 Description of the crushing tube

The crushing tube model has three differentiated parts, as shown in Figure 4.1. The first part differentiated is the main tube core (colored in red), which is a squared cross-section carbon composite structure of 50 mm x 50 mm, with round fillets of 6.4 mm radius, a length of 200 mm, and a total laminate thickness of 2.16 mm. This tube with layup $[0_2, \pm 45_2, 90_2]_s$ has a ply thickness of 0.135 mm and a mass of 0.13 kg, which is supposed to absorb the crash energy as it deforms and fails progressively during impact. The second part differentiated in blue within the model is the bevel, which shares the cross-section and layup (without symmetry) of the tube. In this case, the bevel has a length of 3.5 mm (one element [10]) and half the thickness of the tube due to the non-symmetry of the layup to simulate a structural trigger [10]. The purpose of the bevel is to initiate a stable progressive crushing of the structure from a controlled high-stress location [10, 37]. Finally, the third differentiated part of the crushing model is the green impactor. This part consists on a centered rigid plate of 100 mm x 100 mm x 5 mm that smashes the structure to simulate the impact onto the tube. The center of the impactor's plate coincides with the tube's.

Each part of the model has an associated material. The impactor has a rigid material model with the elastic properties of a Grade 316 carbon and low-alloy cast steel at 200ºC [52]. The material properties of the steel impactor are collected in Table 4.1. As for the tube and bevel parts, both share the same IM7/8552 unidirectional reinforced carbon fiber composite material from Chapter 3 composite plate. Hence, the material properties of the material have already been presented in Table 3.2.

Property	Value	Units
ρ	$7.9 \cdot 10^{-6}$	kg/mm^3
E	193	GPa
ν	0.25	-

Table 4.1: Grade 316 carbon and low-alloy steel impactor properties for a material exposed to 200ºC [52].

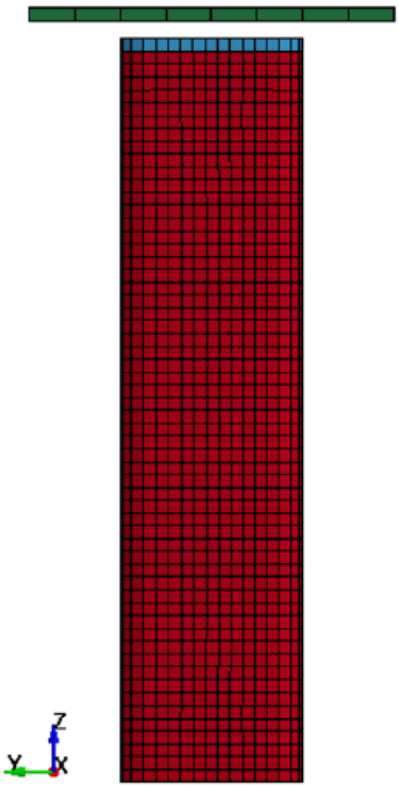

Figure 4.1: CFRP tube crushing analysis setup for tests 46B and 47B. Front view from LS-PrePost.

4.1.2 Boundary and contact conditions

There are 3 boundaries and 3 other contact conditions imposed in the model from Figure 4.1. The first boundary condition consists of one prescribed movement applied at the top of the impactor, which moves the plate downwards on the Z-axis at a constant speed. While the ORNL database shows that this speed is set to 6 m/s in experiments 46B and 47B [51], Cherniaev et al. prove that 5.5 m/s presents a better correlation with the test results for the first 15-20 ms of simulation time. Hence, the constant speed curve defined in the *BOUNDARY_PRESCRIBED_MOTION_RIGID* keyword uses the 5.5 m/s. Additionally, the boundary condition *BOUNDARY_SPC_SET* keyword is set to ensure that the rigid plate only moves along the Z-axis by restricting rotation and translation degrees of freedom for the X and Y axes. The last boundary condition also uses *BOUNDARY_SPC_SET* keyword to fix the tube at its bottom both for translation and rotation axes. That way, the tube is kept in place and does not move while the impactor is crushing it.

To define the contact conditions, the tube and the bevel are considered as a whole set, which shares the nodes at their interface since their mesh elements are the same size. That way, the self-contact of the set upon crashing is well represented and prevents the elements to cross each other freely. This contact condition is done with the *CONTACT_AUTOMATIC_SINGLE_SURFACE* keyword. Besides this, the *CONTACT_AUTOMATIC_SURFACE_TO_SURFACE_ID* condition is set to establish the contact the impactor exerts onto the tube and bevel collective by pushing these downwards [10, 11]. Both mentioned contact conditions use non-zero static friction coefficient and viscous damping coefficient in percent of critical of 0.2 and 40, respectively. Finally, to register the surface to surface contact reaction forces, the *CONTACT_FORCE_TRANSDUCER_PENALTY* keyword is used. Nonetheless, this last keyword does not have a physical meaning for the model, so no coefficients must be specified as this contact condition only registers the force values of the impactor generated onto the structure. From these registered values, the master forces generated by the impactor plate are used in the post-processing of the analysis.

4.1.3 Material models

There are two materials to model in LS-DYNA for this exercise: the IM7/8552 unidirectional reinforced carbon fiber composite from the tube and bevel, and the rigid steel material for the loading plate. The steel impactor is modeled using the material card *MAT_RIGID* with the properties from Table 4.1. The composite material, however, has two possible material cards to model the properties from Table 3.2 [9, 10, 11]:

MAT_054_ENHANCED_COMPOSITE_DAMAGE
MAT_058_LAMINATED_COMPOSITE_FABRIC

Both material models are used in the crushing tube analysis to conclude which one represents best the behavior that is expected from the composite material [10, 11]. *MAT_054* and *MAT_058* present stress-strain curves that converge at a finite stable value, regardless of how softened these are before or after the peak of stress (see Figure 4.2). In Figure 4.2, the material model *MAT_262* is also present. However, this one is not used in this exercise as it does not present a stable crushing behavior. After the peak of stress, the curve degrades with the tube to represent a continuum damage model [9, 10], which is a more complex approach than the one required for this thesis.

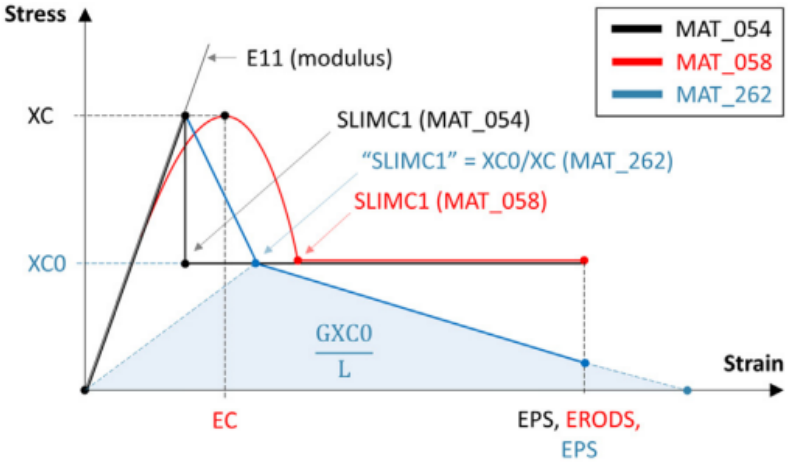

Figure 4.2: Stress-strain curve for material models 054, 058 and 262. The caption corresponds to Figure 1 from Cherniaev et al., p.350 [10].

Regarding the chosen material models, *MAT_054* is the most common model used in composite crushing simulations as it can represent orthotropic and unidirectional shell structures [9]. This model can activate laminated shell theory to correct the uniform constant shear strain throughout the composite's thickness and assumes a simple linear elastic stress-strain response on the composite's ply level until the first one fails at the stress peak. This linearity is presented in Figure 4.2 and it does not include any softening before or after the peak of stress. *MAT_054* model has as inputs basic properties of the IM7/8552 composite, such as the ones portrayed in Table 3.2, which include longitudinal, transverse, and normal Young's modulus, Poisson ratios, shear modulus, compressive and tension strengths, and the material's density. However, the material card also includes parameters to define the damage zone (non-elastic linear behavior) of the stress-strain curve from Figure 4.2. First of all, the failure criteria followed in this material model is the Chang-Chang stress criterion, which requires as input the indices of the longitudinal and transverse stresses in tension and compression to identify the failure of the plies. Additionally, reduction factors for tension and compression (FBRT,YCFAC) are included to represent how the strength of the composite diminishes in the fiber direction after the first ply fails. The damage definition is also supported by non-physical parameters such as erosion, controlling crash front softening, and material characterization after failure parameters [9, 10]. These parameters can eliminate elements when their time step is smaller than a given value (TFAIL), define the effective failure strain (EPS) and the softening reduction factor for the material strength upon crushing (SOFT), say what percentage of plies must fail to consider the crash front initiation (PFL); stating the factors of the minimum stress limit after a maximum stress peak in tension (SLIMTx), compression (SLIMCx) and shear (SLIMS) for fiber (x=1) and matrix (x=2) directions. The mentioned non-physical parameters' initial values are taken from Cherniaev et al. project to match the conditions of ORNL tests 46B and 47B (see Table 4.2) [10, 51].

MAT_058 material model can model solids, but it is also suitable for shell composite elements with unidirectional layers, complete laminates and woven fabrics [9, 10]. The difference with *MAT_054* material model is that *MAT_058* is capable of modeling, for a simplified laminate, the damage mechanics after its stress peak from Figure 4.2. This is done by using non-linear softenings around the stress peak and implementing Hashin's failure criteria to the composite ply-level [10, 53]. In the material card from LS-DYNA, *MAT_058* still requires the same general properties from Table 3.2 as inputs, but it also requires damage evolution parameters, whose formulation in its material card presents a smooth increase in damage and prevents the immediate drop of stresses after failure initiation [10, 53]. This damage evolution is also determined through non-physical properties, which are mostly coincident with the ones from *MAT_054* [9]. The difference resides in the change of names. *MAT_054*'s TFAIL is called TSIZE in *MAT_058*, but it has the same goal and value as Table 4.2. A similar thing happens to *MAT_054*'s EPS, which is called ERODS in *MAT_058*, but in this case, the value is negative. The remaining factors to determine the softening or minimum stress after the peak (SOFT, SLIMT1-2, SLIMC1-2, and SLIMS) are called the same and share values with Table 4.2.

Property	**Value**	**Units**
TFAIL	10^{-7}	s
EPS	0.55	mm/mm
SOFT	0.57	-
PFL	100	-
SLIMT1	0.01	GPa/GPa
SLIMC1	1	GPa/GPa
SLIMT2	0.1	GPa/GPa
SLIMC2	1	GPa/GPa
SLIMS	1	GPa/GPa
FBRT	0	-
YCFAC	2	-

Table 4.2: LS-DYNA non-physical parameters for *MAT_054_ENHANCED_COMPOSITE_DAMAGE* model to define damage upon tube's crushing. Initial values taken from Cherniaev et al., p.352 [10].

Some of the parameters determining the damage outcome in Figure 4.2's stress-strain curve, can be further tuned from the recommended values from Cherniaev et al. This is the case of SLIMC1 and SOFT, which are chosen to further adjust the stress-strain response of the crushing tube to ORNL's tests 46B and 47B [9, 10, 11]. The reason these are chosen is first, to smooth the transition from the stress peak into the damage zone, second, because the tube composite's fiber direction for the 0° laminate aligns with the compression load applied to it, and lastly because the IM7/8552 is assumed to have a relatively large content in fibers that determine the tube's properties. Hence, SLIMC1 in the fiber direction is chosen as a more determining factor than SLIMC2 for the matrix direction, and SOFT represents better the non-linear behavior of a crushed structure. After the tuning of these non-physical parameters, both material models will be evaluated with the final tuned values to determine which one is worth using in terms of reliability to the real crushing scenario, and the computational cost.

4.1.4 Elements' type

As explained in Chapter 2, numerical simulations usually use solid elements in the mesh of impactors and crushing plates that remain undeformed, and shell elements are used for parts that expect deformations. This principle is therefore followed in this analysis, where the impactor plate is a solid rigid plate, and the tube and bevel parts are modeled as Belytschko-Tsay shell elements.

The rigid plate uses an arbitrary coarse number of elements in its mesh to reduce the computational cost, in addition to this one not presenting any deformation upon crushing [10]. There are a total of 64 squared elements in the plate, so their dimensions are 12.5 mm x 12.5 mm. As for the tube and bevel, both meshes have square elements of 3.5 mm per side [10, 11], so the common nodes can be shared in the bevel and tube's interface. All tube and bevel shell elements are oriented upwards in the Z-axis so that they are aligned with the compression load. That orientation is considered the 0° of the layup for reference, as mentioned in the

previous sub-section, which determines the non-physical parameters to be tuned.

4.1.5 Validation

As mentioned earlier in this section, the simulation model follows Cherniaev et al. indications to match the ORNL tests 46B and 47B setups [10, 11, 51]. This is done because the resulting experimental data from 46B and 47B tests are used as validation for this chapter's tube crushing analysis. To validate these, the first 15 ms of simulation after the crash initiation is evaluated. The time step chosen for sampling and registering data must be big enough to save computation time and avoid over-sampling, but small enough so intermediate data that can be of relevance is not neglected. Hence, the intermediate time step for the analysis and data sampling is 0.2 ms.

4.2 Results and post-processing

The results from crushing tube analysis require post-processing to transform the force-displacement graph into crashworthiness properties, just like it was introduced in Chapter 2.

The keywords *DATABASE_RCFORC* and *DATABASE_NODOUT* are used in LS-DYNA to get the force and displacement ASCII data generated in the tube upon crushing. The keyword *DATABASE_RCFORC* is the responsible one to getting the forces and displacements from the impactor plate registered due to the *CONTACT_FORCE_TRANSDUCER_PENALTY* condition. With this data, the force-displacement graph is generated and filtered with a SAE filter and a cut-off frequency of 1000 Hz to match the data of reference from Cherniaev et al. and ORNL tests 46B and 47B [10, 11, 51]. From the force-displacement graph, three crashworthiness metrics are used to evaluate the tube's crushing model: the peak and mean force values, and the energy absorbed by the tube (see Chapter 2). These are indicated in Figure 4.3.

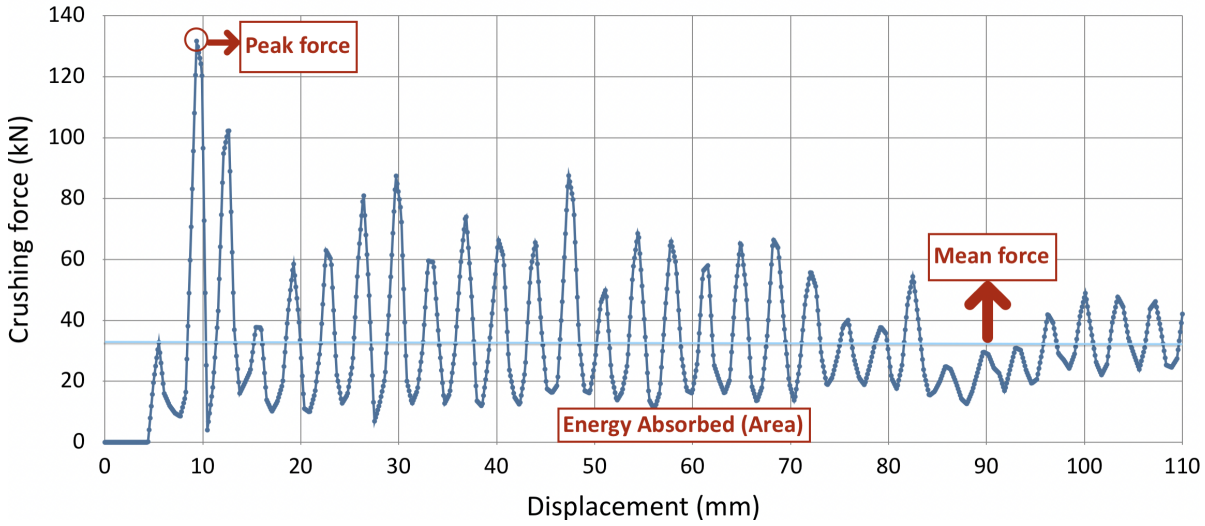

Figure 4.3: Crashworthiness metrics to evaluate tube's crushing response.

The resulting force-displacement graph from each crushing tube analysis is plotted with respect to the ORNL tests 46B and 47B for validation. Additionally, the retrieved crashworthiness metrics are compared using tables to calculate how close the analysis is to the experiments when tuning the parameters SOFT and SLIMC1 [11, 51]. After the tuning, also called sensitivity analysis, the final values are introduced in both material models to compare them under the same conditions. The sensitivity analysis is first done solely using the material model *MAT_054* for its simplicity and reduced computational costs [9].

4.2.1 Sensitivity analysis results using the enhanced damage composite material model

As mentioned, the crushing tube model uses LS-DYNA's material card *MAT_054* with non-physical parameters values of SLIMC1 = 1 and SOFT = 0.57 [10]. These must be tuned because by changing their values, the

softening in the force-displacement graph varies. For example, the lower their values are, the less softening is applied to the response, and the higher will be the load oscillations in the force-displacement graph.

SLIMC1 parameter is tuned first to avoid its unity value to lead to an unstable crushing of the tube. The range of SLIMC1 must be comprised between 0 and 1. Therefore, values of 0.25, 0.5, 0.75, and 1 are used per analysis. The value of 0 presents the same effect as the unity, so it is not included in the tuning process. The generated force-displacement graph per SLIMC1 analysis and ORNL tests results [51] is bound to a displacement below 90 mm in the X-axis (see Figure 4.4). This value is also limiting in the force-displacement graph of the numerical simulations, which is close to the total displacement generated in the 15 s after crash initiation.

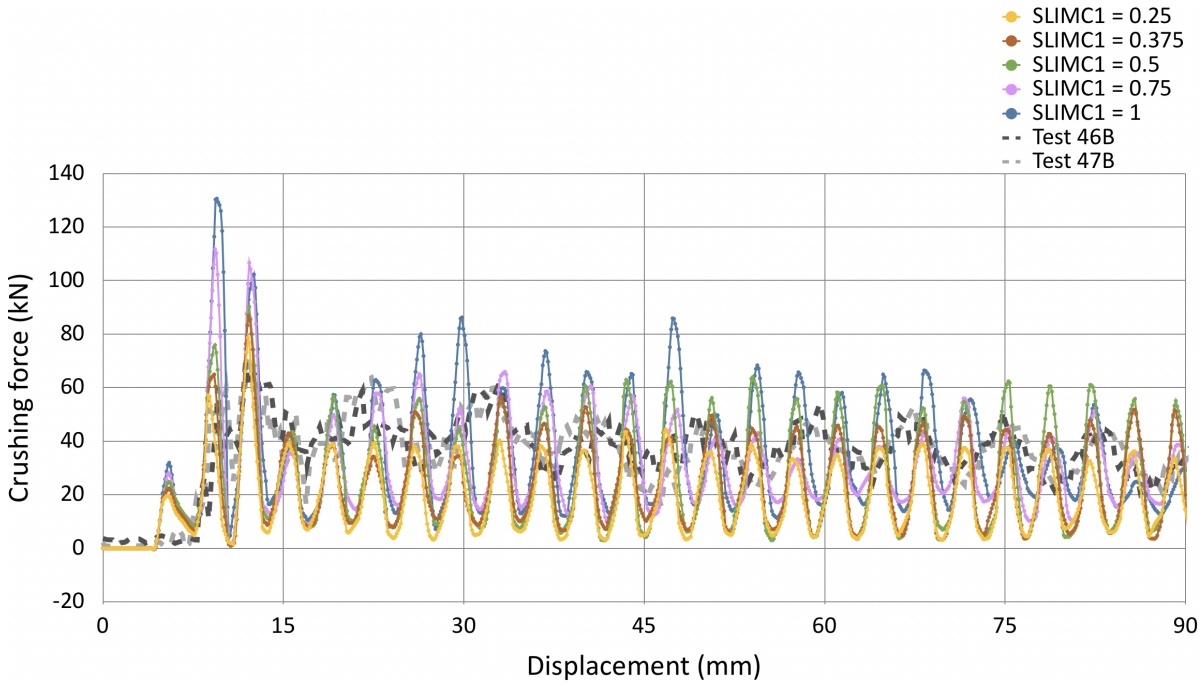

Figure 4.4: Crushing tube analyses force-displacement graph using a fixed SOFT=0.57 and variant values of SLIMC1.

#Analysis or #Test	**F_{peak}** (kN)		**F_{mean}** (kN)		**EA (J)**	
	Value	|Error (%)|	Value	|Error (%)|	Value	|Error (%)|
SLIMC1 = 0.25	78.67	11.57	19.08	50.25	2028.82	32.82
SLIMC1 = 0.375	86.55	22.75	23.60	38.47	2520.21	16.55
SLIMC1 = 0.50	90.22	27.95	26.47	30.99	2815.10	6.78
SLIMC1 = 0.75	111.62	58.30	28.92	24.60	3074.94	1.82
SLIMC1 = 1	130.59	85.21	33.55	12.53	3584.99	18.71
Test 46B	69.31	-	38.57	-	-	-
Test 47B	71.71	-	38.13	-	-	-
Average tests	70.51	-	38.35	-	3020	-

Table 4.3: Results from the first stage of the sensitivity analysis: variant values of SLIMC1 with a fixed SOFT = 0.57.

Figure 4.4 shows that the peak force increases with the SLIMC1 value, which means that lower values of SLIMC1 adapt better to the test results 46B and 47B [10, 11, 51]. Taking a closer look at curves from analyses SLIMC1 = 0.25 and SLIMC1 = 0.5, it is possible to see how the first value presents a lower force peak but presents lower stabilized oscillations when compared with the tests. For SLIMC1 = 0.5, the resulting curve does the opposite: it presents a larger peak of force, which is unwanted upon crushing but has a better representation of the stabilized part of the crash by presenting oscillations of the same magnitude (or higher) with respect to the tests. In both cases, the drawbacks are of big importance, so a trade-off is made by choosing an intermediate SLIMC1 value between the two curves: 0.375. Figure 4.4 shows how this one presents a

lower peak than for SLIMC1 = 0.5, and better matching oscillations after the peak force. The argumentation of the chosen SLIMC1 value is backed up by the crashworthiness metrics (F_{peak}, F_{mean} and EA) presented and evaluated in Table 4.3, which includes the tests values as well. Since experiments 46B and 47B have the same setup, their average values are taken as the reference for this sensitivity analysis to tune SLIMC1 and SOFT parameters.

Table 4.3 proves that simulations with higher SLIMC1 values have a better mean force and energy correlation in their results, which is translated into higher stabilized oscillations after the peak force in Figure 4.4. However, these also present a much larger peak force, which is undesired for crashworthiness and does not match the results from tests 46B and 47B [51]. With the SOFT parameter left to tune, these peaks can further increase, which is why the intermediate value of SLIMC1 = 0.375 is confirmed to be the most adequate one amongst the lowest SLIMC1 studied values.

The tuning of the SOFT non-physical parameter is done by fixing the SLIMC1 parameter to 0.375. The values for the SOFT parameter are also bounded between 0 and 1, where higher values provide smoother crushing responses. Therefore, the additional values studied to tune the SOFT parameter are higher than the initially set 0.57 [10]: 0.8 and 1. The force-displacement responses per analysis using the different SOFT parameters and the tests of reference can be found in Figure 4.5 [51].

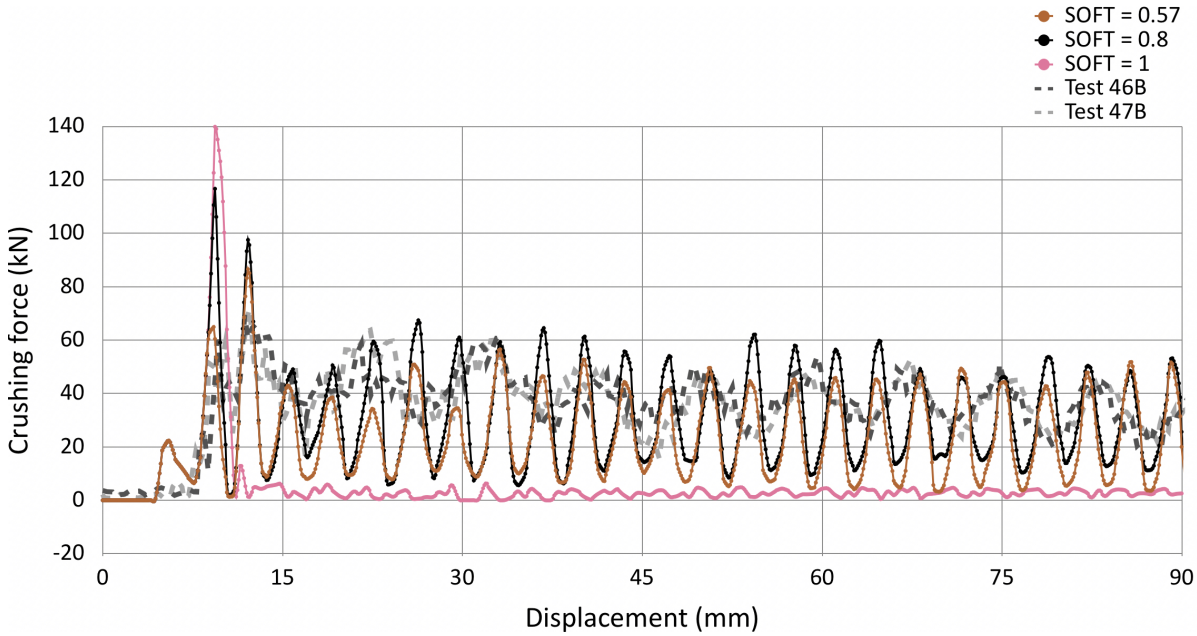

Figure 4.5: Crushing tube analyses force-displacement graph using a fixed SLIMC1 = 0.375 and variant values of SOFT.

#Analysis or #Test	**F_{peak} (kN)**		**F_{mean} (kN)**		**EA (J)**	
	Value	|Error (%)|	Value	|Error (%)|	Value	|Error (%)|
SOFT = 0.57	86.55	22.75	23.60	38.47	2520.21	16.55
SOFT = 0.8	116.67	65.46	29.97	21.86	3201.36	6.01
SOFT = 1	139.89	98.39	5.02	86.91	536.25	82.24
Test 46B	69.31	-	38.57	-	-	-
Test 47B	71.71	-	38.13	-	-	-
Average tests	70.51	-	38.35	-	3020	-

Table 4.4: Results from the second stage of the sensitivity analysis: variant values of SOFT with a fixed SLIMC1 = 0.375.

Figure 4.5 shows that the unit value of the SOFT parameter presents the largest peak of force, and then induces a set of very small oscillations. Even below simulations with SOFT parameters 0.57 and 0.8, and the tests 46B and 47B. This shows that the softening of the simulation is far too high, which produces an inconsistent be-

havior as shown. Therefore, the unity value is disregarded in the selection. The remaining simulations using SOFT 0.57 and 0.8 present more consistency, as the oscillations after the force peak are about the same size in each case. From there, despite having a larger force peak, the simulation using SOFT = 0.8 represents better the crushing of the tube from the tests due to its larger oscillations' magnitude. This implies a better mean force and EA correlation, which is confirmed with the values from Table 4.4.

Table 4.4 shows that the SOFT value of 0.8 is indeed the analysis with better overall correlations for the crashworthiness metrics from tests 46B and 47B. It has a lower peak force than the unit, but a better mean force and EA correlation than the 0.57 softening. Therefore, the final SLIMC1 and SOFT tuned values are collected in Table 4.5 for future analyses.

Material card parameter	Tuned value
SLIMC1	0.375
SOFT	0.8

Table 4.5: Final selected values from the SLIMC1 and SOFT sensitivity analyses.

4.2.2 Comparison of material models

The final tuned values from the sensitivity analyses (see Table 4.5) are introduced into both material models *MAT_054* and *MAT_058* as explained at the beginning of the chapter. That way, both material models are compared under the same numerical conditions to determine which one represents better the crushing of the tube. The procedure resembles the one from the sensitivity analyses and uses tests 46B and 47B as reference [10, 11, 51].

The force-displacement curves resulting from both material models are shown in Figure 4.6 to evaluate the crashworthiness metrics of peak and mean forces, and EA. These values are also collected in Table 4.6.

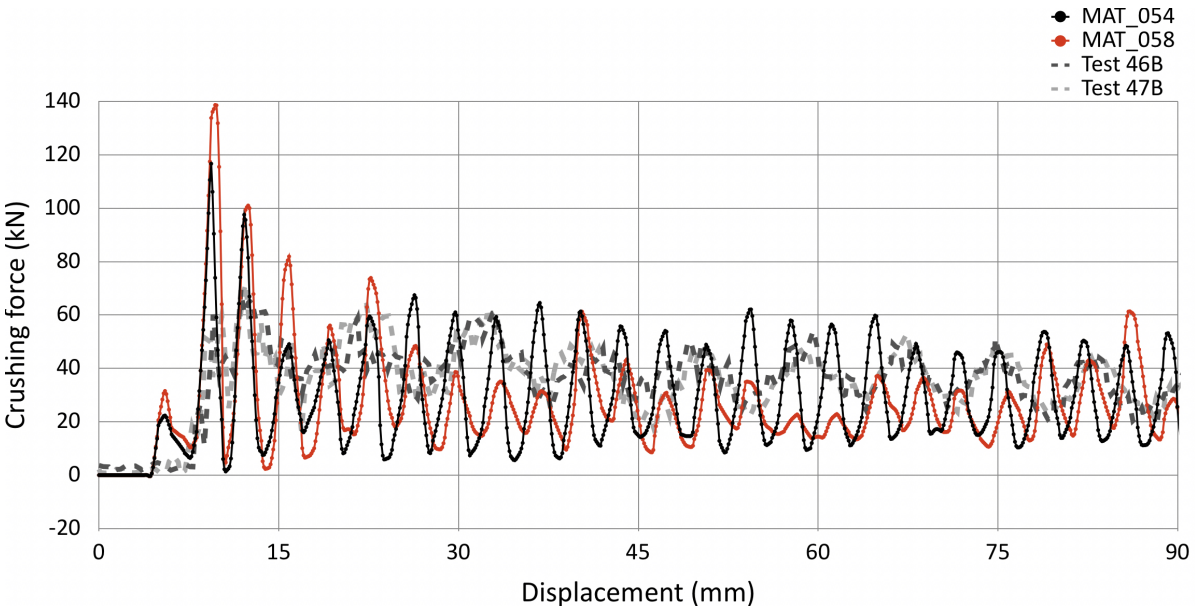

Figure 4.6: Crushing tube analyses force-displacement graph using material cards *MAT_054* and *MAT_058*.

Figure 4.6 and Table 4.6 prove that *MAT_058* overpredicts the peak force of the numerical simulation. Additionally, the estimated EA and mean force are lower than the ones represented in the analyses using material model *MAT_054*, and the computational costs are higher. Therefore, *MAT_054* is chosen as the material to better represent the crushing of the tube and save computational costs. This material will be used in future chapters for the tube's optimization in Chapter 5, and its implementation into a fuselage in Chapter 7. When doing so, the final results from this chapter's baseline analysis (collected in Table 4.7 for further clarity) are used as reference.

#Analysis or #Test	F_{peak} (kN)		F_{mean} (kN)		EA (J)	
	Value	|Error (%)|	Value	|Error (%)|	Value	|Error (%)|
MAT_054	116.67	65.46	29.97	21.86	3201.36	6.01
MAT_058	138.64	96.62	27.91	27.23	2982.65	1.24
Test 46B	69.31	-	38.57	-	-	-
Test 47B	71.71	-	38.13	-	-	-
Average tests	70.51	-	38.35	-	3020	-

Table 4.6: Results from the same crushing tube analyses using material cards *MAT_054* and *MAT_058*.

Layup	Material	F_{peak} (kN)	F_{mean} (kN)	EA (J)
$[0_2, \pm 45_2, 90_2]_s$	IM7/8552	116.67	29.97	3201.36

Table 4.7: Crashworthiness metrics resulting from the baseline tube analysis, with tuned SLIMC1 = 0.375, SOFT = 0.8 and material model *MAT_054*.

4.3 Computation time

The crushing tube analyses presented above contain a slightly more complex setup than the composite plates simulations from Chapter 3, as it uses three-dimensional composite parts and a rigid plate as an impactor. This, together with *MAT_054_ENHANCED_COMPOSITE_DAMAGE* material model and the defined tube and bevel's layup, lead to the sensitivity analysis simulations taking about 30 minutes of computation time. Nonetheless, after tuning the parameters of the sensitivity analysis, the same analysis using material *MAT_058_LAMINATED_COMPOSITE_FABRIC* model, takes 10 more minutes of computation time. This, together with the difference in results this one presents when using pre and post-peak softening, disregard the analysis as the baseline result of reference for the next chapter.

Chapter 5

Design optimization of the square tube

In this section, the tube model from Chapter 4 is introduced in LS-OPT's optimization software to find an optimal layup that improves the crashworthiness metrics resulting from Table 4.7 [54]. The crashworthiness metrics studied are the peak and mean forces and the EA; which depend on the layup of the tube and its bevel. The number of plies per laminate is unchanged throughout the optimization process.

The layup ply orientation optimization can be done using directly an optimization algorithm encoded, but LS-OPT's interface offers alternatives that accelerate the process and saves computational costs. First, LS-OPT can interact with LS-DYNA during the sampling of possible optimal solutions. This LSTC software interaction is an advantage, given that LS-DYNA cannot be parametrized in Python as other FEA codes, such as Abaqus. Additionally, the whole optimization process can be automated through a graphic interface with many setup features to choose from. This saves time in the optimization setup and provides a more intuitive usage which prevents the user to interfere while the optimization is going on. Finally, LS-OPT allows metamodel optimization methods, which sample the model to generate fitted surface responses and calculate possible optimal solutions through it. This approach has been proven to be effective in aerospace applications with non-gradient algorithms like GA [40, 41, 55, 56], which capture better the non-linearity of a crash event [54]. Nonetheless, LS-OPT can have its limitations in terms of setup [54].

A multi-objective metamodel optimization approach is used to optimize more than one crashworthiness metric by changing the tube's layup from Chapter 4. LS-OPT allows so while considering all objectives equally important [54], and generating a Pareto frontier from the resulting optimal models. A Pareto frontier is a set from the resulting layup designs that maximize or minimize the optimization objectives accordingly with equal importance. This is favorable, since giving priority to one of the objectives over the others would not be justified and the optimization of one of the objectives can worsen the other crashworthiness metrics. The ply orientations of the tube's laminate are the design variables of the optimization process, which characterize the entire model, leading to a global domain optimization approach. The global domain approach provides optimal solutions with responses given by the entirety of the model, instead of focusing on a local sub-region or domain. LS-OPT provides three strategies to implement the global domain multi-objective optimization, called single iteration, sequential, and efficient global optimization (EGO) [54, 56]. The single iteration strategy allows metamodel optimization but needs a lot of points to solve the exercise in one iteration, meaning that it is a computationally expensive strategy. The sequential strategy with no domain reduction allows metamodel optimization and a global approach, but requires fewer sampled points per iteration and improves the solution accumulatively as iterations go by. Hence, a precise metamodel surface is important for this one to work. Finally, the EGO is still under development and quite limited in LS-OPT, not allowing a multi-objective optimization setup and working only on a Kriging's metamodel fitting [54].

5.1 Setup of the optimization

LS-OPT optimization setup is done through the graphic interface's diagram from Figure 5.1. The diagram changes depending on the chosen strategy. As mentioned above, due to the single iteration strategy being computationally expensive, and the EGO being ruled out, the sequential strategy with no domain reduction is the only eligible choice [54]. With its consequent diagram (see Figure 5.1), it is possible to compare potential

metamodels that are suitable for global multi-objective optimization.

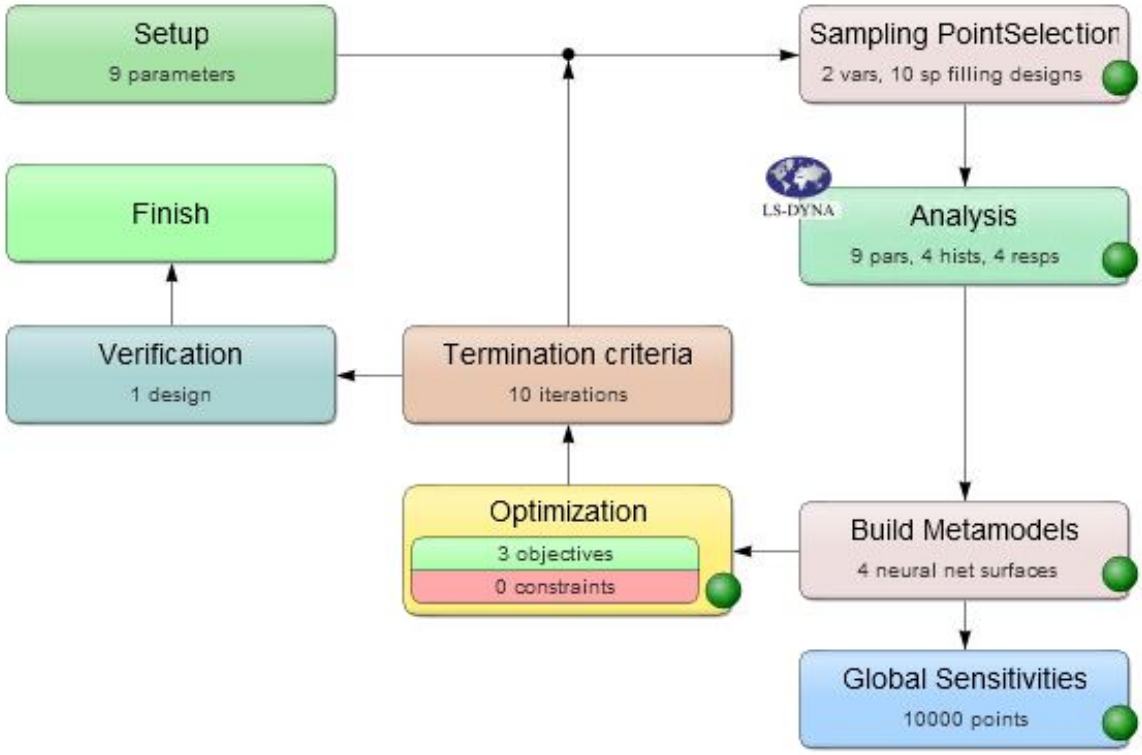

Figure 5.1: Sequential diagram (closed-loop) of optimization setup in LS-OPT.

With Figure 5.1 as the diagram of reference, each block (or module) of the diagram needs some inputs to define the design variables, optimization metamodel, sampling strategy, optimization objectives, optimization algorithm, and termination criteria to finish the optimization process [54]. First, the *Setup* block is where the design variables are introduced. To define these, the curse of dimensionality must be taken into account, which means that the more active parameters LS-OPT have as inputs in this block, the more time LS-OPT requires to sample and optimize these. Therefore, the number of plies orientations to optimize are reduced by considering the following stacking sequence and performance "rules of thumb" [57]:

- The tube's laminate should remain symmetric to eliminate unwanted bending coupling and simplify the crushing scenario.
- Both tube and bevel's stacking sequence should be balanced to eliminate shearing coupling. Hence, for every positive ply orientation, there will be a negative one. This does not apply to 0 and 90-degree ply orientations.
- At least a 10% of the plies in the laminate cover the principal ply orientations: 0,± 45, and 90 degrees. That way, the laminate can protect the tube and bevel from secondary load cases that may arise during the crushing.
- There should not be more than four to six consecutive plies of the same orientation in the laminate. That way, the stack of plies never exceeds 0.54-0.81 mm of thickness, and the discontinuities avoid premature failure of the laminate.
- A set of ± 45 degrees outer plies is used to increase damage resistance and limit the fiber splitting caused by low-speed survivable impacts. Therefore, this improves the crashworthiness behavior of the tube's layup.

With the mentioned "rules of thumb", the layup is partially defined to meet these, leaving plies' orientations *p4, p5, p6* and *p7* as design variables.

$$[\pm 45, 0, p4, p5, p6, p7, 90]_s$$

From the *p4, p5, p6* and *p7* design variables stated above, the parameters *p4* and *p6* are set as active variables, while *p5* and *p7* depend on them. This is done in order to comply with the balanced layup design rule and accelerate the optimization process convergence. Table 5.1 collects all the design variables' characteristics defined in the *Setup* block (see diagram Figure 5.1).

Variable name	Symbol	Type of variable	Active or dependent	Potential values	Sampling type	Units
4_{th} ply orientation	*p4*	Discrete	Active	$0, \pm 15, \pm 30, \pm 45, \pm 60, \pm 75, 90$	Continuous	Degrees (°)
5_{th} ply orientation	*p5*		Dependent	$-p4$	-	
6_{th} ply orientation	*p6*		Active	$0, \pm 15, \pm 30, \pm 45, \pm 60, \pm 75, 90$	Continuous	
7_{th} ply orientation	*p7*		Dependent	$-p6$	-	

Table 5.1: Parameters defined for the optimization of the tube in LS-OPT [54].

Based on the information from Table 5.1, the final parametrized stacking sequence of the tube is the following. The bevel's layup is the same without the symmetric laminate.

$$[\pm 45, 0, p4, -p4, p6, -p6, 90]_s$$

The Stage module from the diagram, renamed as *Analysis* in Figure 5.1, is the one that connects LS-OPT to LS-DYNA's model to perform the sampling and construction of the different metamodel surfaces. This module is also responsible to register historical data and responses from LS-DYNA's analysis that define the optimization objectives and post-processing graphs. The *Optimization* block is responsible for defining the three optimization objectives from the analysis responses. The three objectives are maximized. Nevertheless, the peak force objective is minimized by changing its response sign in LS-OPT, leaving the objectives as listed below:

1.- EA (Maximized)

2.- Peak force (Minimized)

3.- Mean force (Maximized)

The *Optimization* block is also responsible to define the constraints and the optimization algorithm. No constraints are defined in the LS-OPT diagram from Figure 5.1 since these are applied afterward manually, once the optimization is finished and provides a set of potential optimal solutions. The following constraints filter undesired solutions to narrow the search for the optimum: the EA and mean force values must be higher than the results presented in Table 4.7, while the peak force must be lower than the reported value in the table. Regarding the optimization algorithm, a hybrid GA for multi-objective optimization is available in LS-OPT, called Elitist Non-Dominated Sorting Genetic Algorithm or NSGA-II [54, 55]. This algorithm presents a Pareto front of the optimal solutions set [54, 55]. As a consequence of the chosen algorithm, the *Termination criteria* module defines when the optimization should end. In this project, the end of the optimization is defined through tolerances instead of establishing a maximum number of generations. That way, the final solutions are better predicted, and the optimization is more efficient by saving computational time when it is not required and avoiding sudden interruptions at a randomly chosen generation. Consequently, only one verification run is set in the final module from Figure 5.1 [54].

5.2 Metamodel comparison

In this section, the *Sampling PointSelection* module from Figure 5.1's diagram is explained to determine the metamodels available for a sequential strategy and suitable for this tube's layup optimization [54]. A few metamodels are set into the optimization process and compared to do the final selection.

5.2.1 Pre-selection

LS-OPT presents a limited set of metamodels that work on an accurate global optimization and provide reliable solutions. As discussed earlier, global optimizations seem to work best and save computational costs when using a sequential strategy. According to the software's manual [54], the surrogate models that work best with the chosen strategy are neural networks and Kriging, which have been already implemented in the optimization of components in the aerospace sector [40, 41, 55]. LS-OPT offers two neural network metamodels, the feed-forward neural network (FFNN) [40, 41], which has been explained in Chapter 2 while using a back-propagation strategy for the optimization of a helicopter's sub-floor. The second neural network offered by LS-OPT is the radial-based neural network (RBF NN) [54]. This last one is the recommended metamodel selection for the sequential strategy setup in LS-OPT. According to the software's manual, the recommended setups represent the most efficient combinations of the metamodel, point selection criteria, transfer and correlation functions, regression algorithms trend models, and even topology selection criteria for the optimization.

Both available neural networks are compared despite the program's recommendations since FFNN is used more than the radial based one for the way the training set defines the network and builds an accurate response surface with respect to the original design [40, 41]. Additionally, LS-OPT's manual states that RBF NN does not represent well non-linear phenomena like a crash [54]. The comparison among the three potential metamodels for the multi-objective optimization is briefed in Table 5.2.

Metamodel	Advantages	Disadvantages
Feed-forward neural network (FFNN)	• Smaller fitting error (RMS). • Cross-validation techniques can be used to assess the predictive capabilities of the metamodel. • Good in global approximations as it updates itself. • Better than RBF NN in smooth problems.	• Generally larger predictions error than RBF NN. • Expensive to construct (requires big training sets of data). • Time consuming.
Radial-based function neural network (RBF NN)	• High prediction accuracy, even when using cross-validation. • Cheap and fast due to linear nature. • Extra responses do not add much calculation time.	• Linear nature may not represent crash phenomena correctly.
Kriging	• Generally accurate (exact solution at the sampling points).	• LS-OPT implementation is still under construction. • Sensitive to noise for interpolated data in-between sampling points. • Fitting problems with non-smooth surface responses. • Time consuming. • Does not use cross-validation in metamodel's assessment.

Table 5.2: Advantages and disadvantages of the metamodels' and their setup possibilities in LS-OPT [54].

According to Table 5.2, the neural networks' disadvantages depend on the problem they are applied to. In the case of a crash, the model's behavior is expected to be non-linear and provide non-smooth responses. Thus, to verify which metamodel adapts better to the given case, these are tried out in different optimizations to evaluate which surrogate model provides better-predicted results. Regarding Kriging's metamodel, its setup limitations in LS-OPT are still nowadays its biggest setback. Its usage is to this day implemented in LS-OPT to use the EGO strategy, which might be why in sequential strategies, Kriging is still very limited and cannot be tested in optimization with the same setup as the neural networks' [54]. Kriging also presents an undesired sensitivity to noise, and LS-OPT does not use cross-validation either to assess this metamodel's accuracy, which risks the metamodel being less accurate than the neural networks in certain conditions. Conclusively,

solely the neural network metamodels are set up in the optimization for comparison.

5.2.1.1 Setup

The setup features required for the chosen neural networks are about how these sample points build the network, which transfer functions this one has, and its topology selection criteria metrics to measure how accurate the network is to the actual model's response [54]. These features are shared in both metamodels, but in the case of the feed-forward neural network, the metamodel requires an extra setup feature for the network's regression algorithm. The regression algorithm is responsible one to extrapolating the non-linear problem into a linear one to get an optimal solution through it [54]. This is not needed for the radial-based neural network as this one has a linear first-order nature. The total of four setup features used in these metamodels can be set by the user by selecting one of the options LS-OPT offers in each case. Nonetheless, the program is set to use a recommended combination of these to set the metamodels optimally without the intervention of the user [54]. In this chapter, the recommended combinations are used for simplicity, which is listed in Table 5.3 for each metamodel.

Metamodel	**Setup feature**			
	Point selection method	**Transfer function**	**Topology selection criteria**	**Regression algorithm**
FFNN	Space filling for Pareto front (1^{st} iteration uses D-optimal). Include points from previous iterations.	Sigmoid (in) Linear (out)	Mean average type (uses MSE cross-validation).	Lavenberg-Marquardt. Active metamodel with parallel/series builder.
RBF NN		Hardy's Multi-Quadratics	Leave-one-out (general cross-validation).	-

Table 5.3: Neural network setup features, following recommendations from LS-OPT manual [54].

For the setup of the feed-forward neural network, the point selection method is the space-filling for the Pareto front, which is a recommended setup from LS-OPT for multi-objective optimizations with sequential strategy. Space-filling point selection technique maximizes the distance between sampled points within the design to cover as much ground as possible and build the metamodel accordingly. Due to the sequential strategy used, each iteration includes the Pareto Optimal Frontier (POF) points from the previous ones. This fact helps achieve an optimal solution by the end of the optimization. Nonetheless, the first iteration cannot include points from an earlier iteration as these do not exist. Therefore, the first iteration uses the D-optimal point selection method to generate the first set of points randomly, which is updated (and corrected) later on in the sequential process [54]. Regarding the transfer function of the feed-forward neural network metamodel, this one uses Sigmoid and Linear functions to activate the intermediate layers and output layer, respectively (p.570 in [54]). The intermediate layers are activated using the Sigmoid function on the input data, while the output layer is activated using a Linear transfer function from the calculated intermediate data. The topology selection criteria of the Mean Squared Error (MSE) and cross-validation to evaluate the feed-forward network metamodel. And finally, the regression algorithm used in this metamodel is the second-order Lavenberg-Marquardt, which is the fastest algorithm to train up to hundreds of adjustable weights (sets of data) in its network (p.571 in LS-OPT 7.0 manual [54]).

As for the radial-based neural network, the differentiated setup features are the transfer function per layer and the topology selection criteria. The selected transfer function to activate intermediate layers in the radial-based neural network is Hardy's Multi-Quadratics function (p.573 in LS-OPT 7.0 manual [54]). The output layer in this case is not required due to this metamodel's linear nature. Finally, the topology selection criteria used in the radial-based network is the Leave-One-Out measurement, as listed in Table 5.3. The measurement assesses the network's appropriateness (p.569 in LS-OPT 7.0 manual [54]) and uses cross-validation repeatedly to evaluate the data distribution and disregard small portions of this one if needed. This criteria is expensive to apply but is advised to use additionally to the standard metrics used by LS-OPT to evaluate the network (p.570 in LS-OPT 7.0 manual [54]). The following section presents these standard evaluation metrics in Table 5.4.

5.2.2 Model accuracy

Both metamodels are set up in separate optimization procedures. This is done in the *PointSelection* module from Figure 5.1, as mentioned in previous sections and using the features in Table 5.3. After each optimization, the metrics that evaluate how close the metamodel's surface is from the one from the original design responses are provided in LS-OPT [54]. In other words, these metrics provide the error approximations of the metamodel and allow the comparison between the two optimization setups. There are two standard metrics to evaluate the feed-forward neural network metamodel in LS-OPT, which are also used for the radial-based one (see Table 5.4). These are the RMS and the coefficient of multiple determination (R^2). RMS measures the normalized root of the MSE to compare data sets' accuracy, regardless of how many construction points the neural network is built upon. For higher accuracy, the normalized root is preferred to be low. The R^2 coefficient represents the variability in model responses provided by the metamodel, which should be close to the unit to cover as much area of the design response as possible and improve the prediction of an optimal solution. Therefore, whenever the area of the design response is too large to be covered by the setup metamodel, R^2 is consequently low. There is an additional metric to evaluate the radial-based neural network metamodel, which is the root metric of the residual prediction accuracy (SQRT PRESS). The residual prediction accuracy is the sum of all prediction errors from the metamodel's design points, according to p.559 in LS-OPT 7.0 manual [54]. As shown in Table 5.4, both RMS and SQRT PRESS metrics use the relative error percentage to show how accurate or different these are with respect to the perfect model. The perfect model is considered to be the one where the optimizations' predicted and computed designs coincide.

Metamodel	**F_{peak}**			**F_{mean}**			**EA**		
	RMS (kN)	R^2 (-)	SQRT PRESS (kN)	RMS (kN)	R^2 (-)	SQRT PRESS (kN)	RMS (J)	R^2 (-)	SQRT PRESS (J)
FFNN	3.29 (3.22%)	0.939	-	1.36 (4.62%)	0.764	-	125 (4.54%)	0.896	-
RBF NN	3.15 (3.08%)	0.945	5.01 (4.91%)	1.23 (4.18%)	0.778	1.79 (6.11%)	133 (4.85%)	0.878	197 (7.15%)

Table 5.4: Metamodel error approximation values using cross-validation for both neural networks.

Table 5.4 presents similar evaluation metrics between both surrogate models. An example of this would be the R^2 values, which are lower than 0.95 (the desired value for this coefficient) for both metamodels in all three objective metrics. Despite these coefficient values being lower, both metamodel metrics are considered acceptable because cross-validation techniques are involved in their evaluation and setup. The main differences between both metamodels reside in the feed-forward neural network showing a better fit for the energy absorption response, while the radial-based network shows slightly better metrics for the peak and mean force responses. These changes are not significantly high, which is why both neural networks' optimal responses are studied to get the one with the best prediction. The chosen result is assumed to imply that its metamodel setup is the most suitable one for this tube crashworthiness optimization.

5.2.3 Optimal design using feed-forward neural networks

The optimization using the feed-forward neural network metamodel presents the setup features presented in the previous sections (see Table 5.3). The resulting layup designs from the optimization's last iteration, which is considered the most accurate given the sequential strategy setup, are presented in Table 5.5. In Table 5.5, the values of the three optimization objectives are based on LS-OPT metamodel's predictions, and from these, the presented designs that further improve the tube's crashworthiness metrics in Table 4.7 are selected as optimum solutions. These selected solutions are presented in Table 5.6, which present their predicted metrics obtained in LS-OPT's optimization, and the computed values obtained from LS-DYNA's tube analyses using such layup. The comparison between these values is made to see how accurate the predictions have been in the optimization process, considering the computed metrics as the values of reference.

Layup	$\mathbf{F_{peak}}$ (kN)	$\mathbf{F_{mean}}$ (kN)	**EA (J)**
$[\pm 45, 0, \mp 75_2, 90]_s$	77.13	25.61	2037.96
$[\pm 45, 0, \mp 75, 90_3]_s$	77.40	26.15	2050.07
$[\pm 45, 0, \mp 60, 90_2]_s$	77.98	25.09	2108.79
$[\pm 45, 0, \mp 45, \mp 75, 90]_s$	84.76	27.69	2125.63
$[\pm 45, 0, \mp 75, \pm 75, 90]_s$	79.26	26.21	2169.63
$[\pm 45, 0, \pm 60, \mp 60, 90]_s$	88.50	27.17	2185.18
$[\pm 45, 0, \mp 60_2, 90]_s$	83.05	27.03	2238.23
$[\pm 45, 0, \mp 75, \mp 60, 90]_s$	82.95	26.66	2328.86
$[\pm 45, 0, \mp 45, \mp 60, 90]_s$	88.74	28.57	2359.41
$[\pm 45, 0, \mp 75, \pm 60, 90]_s$	83.34	26.73	2382.18
$[\pm 45, 0, \mp 45, 90_3]_s$	81.94	24.50	2511.44
$[\pm 45, 0, \mp 60, \pm 45, 90]_s$	93.40	28.99	2516.45
$[\pm 45, 0, \mp 60, \mp 45, 90]_s$	90.25	28.61	2547.65
$[\pm 45, 0, \mp 45, \pm 45, 90]_s$	99.64	30.26	2574.69
$[\pm 45, 0, \mp 45_2, 90]_s$	94.65	29.71	2635.45
$[\pm 45, 0, \mp 75, \mp 45, 90]_s$	91.30	28.60	2668.29
$[\pm 45, 0, \mp 75, \pm 45, 90]_s$	91.01	28.33	2694.86
$[\pm 45, 0, \mp 30, \pm 75, 90]_s$	97.85	28.52	2774.45
$[\pm 45, 0, \mp 60, \mp 30, 90]_s$	99.88	30.58	2883.92
$[\pm 45, 0, \mp 30, 90_3]_s$	94.17	26.27	2914.66
$[\pm 45, 0, \mp 60, \pm 30, 90]_s$	104.54	31.59	2947.56
$[\pm 45, 0, \mp 75, \mp 30, 90]_s$	102.02	31.32	3011.93
$[\pm 45, 0, \mp 75, \pm 30, 90]_s$	102.11	31.20	3063.41
$[\pm 45, 0, \mp 60, \mp 15, 90]_s$	109.99	32.47	3179.86
$[\pm 45, 0, \mp 75, \mp 15, 90]_s$	112.26	33.90	3289.48
$[\pm 45, 0, \mp 75, \pm 15, 90]_s$	112.63	34.05	3344.22
$[\pm 45, 0, \mp 75, 0_2, 90]_s$	116.83	35.09	3421.51

Table 5.5: Resulting designs from LS-OPT's metamodel optimization using feed forward neural network.

Layup	$\mathbf{F_{peak}}$			$\mathbf{F_{mean}}$			**EA**		
	LS-DYNA value (kN)	LS-OPT value (kN)	|Error| (%)	LS-DYNA value (kN)	LS-OPT value (kN)	|Error| (%)	LS-DYNA value (J)	LS-OPT value (J)	|Error| (%)
$[\pm 45, 0, \mp 75, \mp 15, 90]_s$	116.49	112.26	3.63	31.98	33.90	6.01	3457.20	3289.48	4.85
$[\pm 45, 0, \mp 75, \pm 15, 90]_s$	112.89	112.63	0.24	32.88	34.05	3.55	3477.24	3344.22	3.83

Table 5.6: Selected results from the feed forward neural network optimization and their computed and predicted crashworthiness metrics.

A final optimum design must be chosen from the selected ones in Table 5.6. This is relevant to comparing the metamodel optimization results in the following sections. To choose the optimum design from Table 5.6, the totality of designs resulting from the optimization are plotted in Figure 5.2 and Figure 5.3. The baseline analysis is also plotted as a reference. The selected designs (drawn in green) are numbered for further clarity and to match these to their respective layup designs. The design numbered as 1 in Figure 5.2 and Figure 5.3 has $[\pm 45, 0, \mp 75, \mp 15, 90]_s$ as layup, while design number 2's layup is $[\pm 45, 0, \mp 75, \pm 15, 90]_s$. Both Figure 5.2 and Figure 5.3 show the trade-off between the optimization objectives predicted in LS-OPT using a Pareto front. Figure 5.2 present the trade-off between the tube's energy absorption and its peak force upon crushing. In this graph, both selected designs from Table 5.6 are drawn in green and present a higher energy absorption in comparison to their peak force, meaning that they are placed above the Pareto front. In Figure 5.3, the trade-off between the tube's peak and mean forces upon crushing is shown, and in this case, the optimal solutions must be below the Pareto front. That way, the crashworthiness requirements of maximizing the mean force while minimizing the peak force would be met. Nonetheless, this is not the case for the designs in Table 5.6. Therefore, the design that is closest to the Pareto front barrier is then selected as the final optimum design,

as it is the closest to meet both Pareto front conditions. That final design is selected design number 2 with layup $[\pm 45, 0, \mp 75, \pm 15, 90]_s$. This design is also proven in Table 5.6 to be the best one predicted out of the two possibilities.

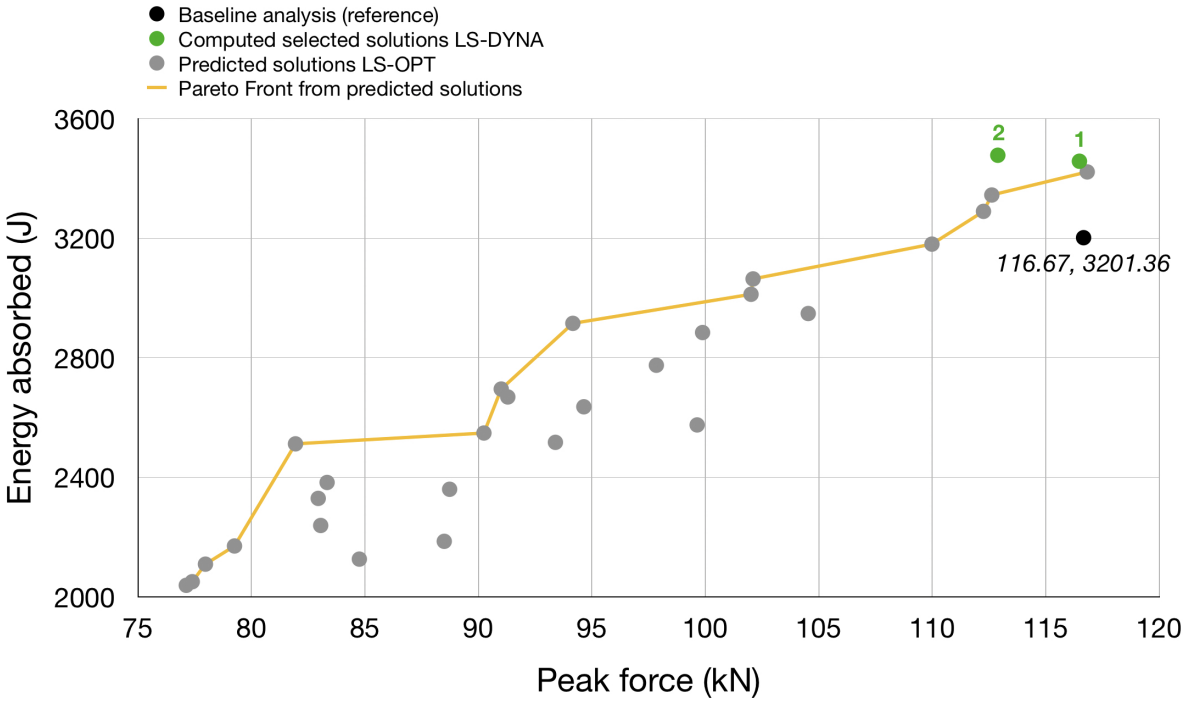

Figure 5.2: EA versus F_{peak} optimization objectives using a feed forward neural network metamodel. The predicted design solutions from LS-OPT build a Pareto front, while including the baseline analysis for reference and the selected solutions computed in LS-DYNA.

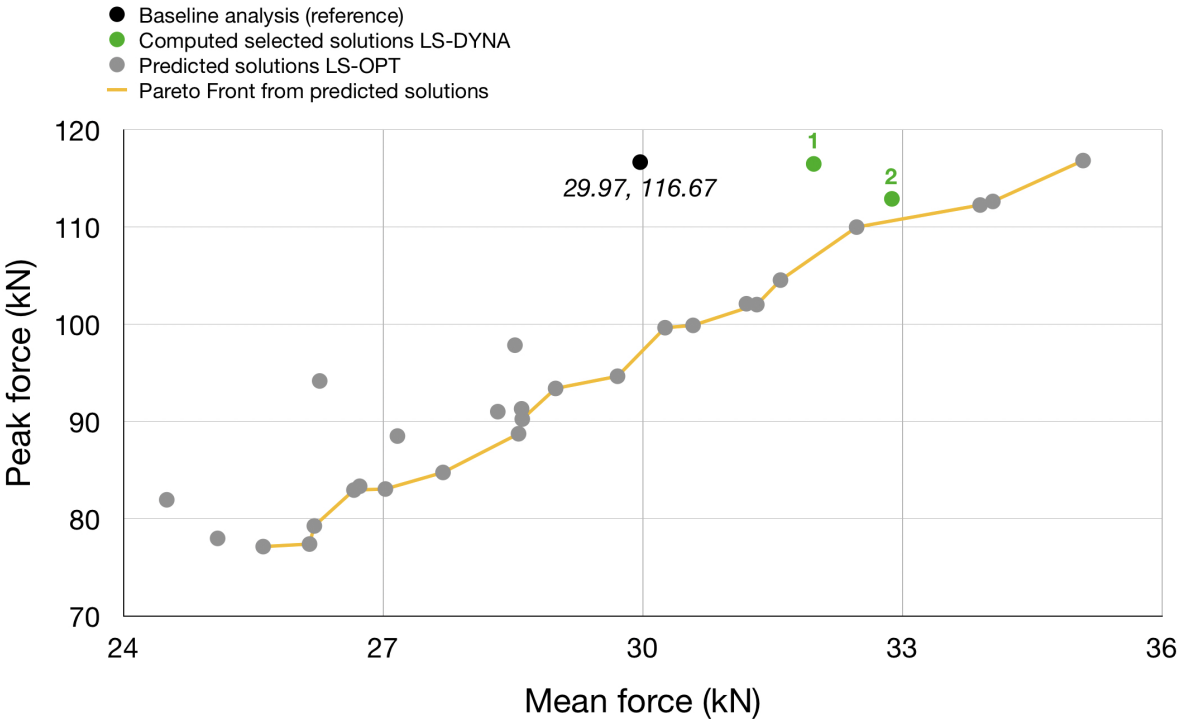

Figure 5.3: F_{peak} versus F_{mean} optimization objectives using a feed forward neural network metamodel. The predicted design solutions from LS-OPT build a Pareto front, while including the baseline analysis for reference and the selected solutions computed in LS-DYNA.

5.2.4 Optimal design using radial based neural networks

The resulting tube layup designs from the radial-based metamodel optimization are listed in Table 5.7. In this case, the metamodel's implementation of the multi-objective GA has made LS-OPT find a larger amount of potential optimum designs for the tube. Despite this, the constraints are still applied manually to select the most eligible designs from Table 5.7 and sent to LS-DYNA to get the crashworthiness metrics values of reference. Hence, the procedure to select one optimum design from this optimization coincides with the one executed in the previous section, for the feed-forward neural network optimization.

Layup	$\mathbf{F_{peak}}$ (kN)	$\mathbf{F_{mean}}$ (kN)	**EA** (J)
$[\pm 45, 0, \mp 60, \mp 75, 90]_s$	75.03	25.94	1999.99
$[\pm 45, 0, \mp 45, \mp 75, 90]_s$	77.75	26.93	2054.46
$[\pm 45, 0, \mp 75_2, 90]_s$	77.73	25.87	2113.01
$[\pm 45, 0, \mp 75, 90_3]_s$	81.17	26.49	2127.76
$[\pm 45, 0, \mp 60, \pm 75, 90]_s$	76.71	25.03	2137.98
$[\pm 45, 0, \mp 60_2, 90]_s$	78.73	26.39	2183.57
$[\pm 45, 0, \mp 75, \pm 75, 90]_s$	77.67	25.51	2233.94
$[\pm 45, 0, \mp 45, \mp 60, 90]_s$	81.95	27.07	2241.06
$[\pm 45, 0, \mp 30, \mp 75, 90]_s$	85.11	28.58	2246.93
$[\pm 45, 0, \mp 75, \mp 60, 90]_s$	81.78	26.65	2320.86
$[\pm 45, 0, \mp 75, \pm 60, 90]_s$	79.88	26.00	2417.05
$[\pm 45, 0, \mp 15, \mp 75, 90]_s$	93.82	30.24	2469.34
$[\pm 45, 0, \mp 60, \mp 45, 90]_s$	87.71	28.03	2478.66
$[\pm 45, 0_3, \mp 75, 90]_s$	99.65	31.14	2595.98
$[\pm 45, 0, \mp 45, \pm 45, 90]_s$	97.12	28.70	2597.63
$[\pm 45, 0, \mp 75, \mp 45, 90]_s$	90.55	28.60	2626.32
$[\pm 45, 0, \mp 75, \pm 45, 90]_s$	88.74	28.15	2683.10
$[\pm 45, 0, \mp 30, \mp 45, 90]_s$	100.59	29.08	2756.00
$[\pm 45, 0, \mp 60, \mp 30, 90]_s$	100.95	30.63	2843.91
$[\pm 45, 0, \mp 75, \mp 30, 90]_s$	102.65	31.36	2979.26
$[\pm 45, 0, \mp 75, \pm 30, 90]_s$	101.85	31.29	2993.21
$[\pm 45, 0, \pm 60, \mp 15, 90]_s$	109.11	32.17	3041.30
$[\pm 45, 0, \pm 75, \mp 15, 90]_s$	109.94	32.80	3144.41
$[\pm 45, 0, 90_2, \pm 45, 90]_s$	110.25	31.81	3190.66
$[\pm 45, 0, 90_2, \mp 15, 90]_s$	112.32	32.94	3256.19
$[\pm 45, 0, \mp 75, \pm 15, 90]_s$	113.62	34.03	3258.16
$[\pm 45, 0, \mp 75, \mp 15, 90]_s$	113.70	33.92	3265.30
$[\pm 45, 0, \pm 75, \pm 30, 90]_s$	115.43	33.94	3310.74
$[\pm 45, 0, \pm 75, 0_2, 90]_s$	115.61	34.47	3317.23
$[\pm 45, 0, \mp 75, 0_2, 90]_s$	118.28	35.04	3369.77
$[\pm 45, 0, \pm 75, \pm 15, 90]_s$	117.47	34.81	3374.09
$[\pm 45, 0, 90_2, \pm 30, 90]_s$	115.49	33.66	3382.03
$[\pm 45, 0, 90_2, 0_2, 90]_s$	117.01	34.43	3424.96
$[\pm 45, 0, 90_2, \pm 15, 90]_s$	118.03	34.64	3466.92
$[\pm 45, 0, \mp 15_2, 90]_s$	133.06	31.15	3474.88
$[\pm 45, 0_3, \mp 15, 90]_s$	135.48	30.63	3491.55
$[\pm 45, 0, \mp 15, 0_2, 90]_s$	137.78	31.73	3501.87

Table 5.7: Resulting designs from LS-OPT's metamodel optimization using radial-based function neural network.

From the optimizations' predicted optimal solutions from Table 5.7, the cases that improve all three objectives with respect to the tube's baseline design from Table 4.7, are listed in Table 5.8. In Table 5.8, the computed values from LS-DYNA analyses for these tube designs are considered once again the reference to see how well LS-OPT's radial based metamodel optimization has predicted the solutions.

In Table 5.8, the first and last design must be disregarded, as the computed values from LS-DYNA overstep

the constraints that have been imposed upon selection or have a prediction error of over 10%. In other words, the computed values of reference indicate that the tube has a larger peak force, lower mean force, and energy absorbed than it should. Consequently, the estimated crashworthiness values in LS-OPT are not accurate enough, and the design cannot be the final optimum. The mentioned faults are marked in red for further clarity. The remaining designs are drawn in green and numbered in Figure 5.4 and Figure 5.5 to match their points from the graphs to their correspondent layup, which are, from 1 to 4, assigned as: $[\pm45,0,\mp75,\pm15,90]_s$, $[\pm45,0,\mp75,\mp15,90]_s$, $[\pm45,0,\pm75,\pm30,90]_s$ and $[\pm45,0,\pm75,0_2,90]_s$. To choose the optimum amongst these, the trade-off between optimization objectives must be looked at. Figure 5.4 and Figure 5.5 represent the energy absorption versus the peak force and the peak force versus mean force trade-offs, respectively. These present a built Pareto front from LS-OPT predicted solutions (see Table 5.7), just like in the previous section.

Layup	**F_{peak}**			**F_{mean}**			**EA**		
	LS-DYNA value (kN)	LS-OPT value (kN)	|Error| (%)	LS-DYNA value (kN)	LS-OPT value (kN)	|Error| (%)	LS-DYNA value (J)	LS-OPT value (J)	|Error| (%)
$[\pm45,0,90_2,\mp15,90]_s$	120.99	112.32	7.17	33.14	32.94	0.60	3488.86	3256.19	6.67
$[\pm45,0,\mp75,\pm15,90]_s$	113.40	113.62	0.20	32.59	34.03	4.44	3459.20	3258.16	5.81
$[\pm45,0,\mp75,\mp15,90]_s$	116.48	113.70	2.39	32.41	33.92	4.65	3493.44	3265.30	6.53
$[\pm45,0,\pm75,\pm30,90]_s$	108.72	115.43	6.17	31.32	33.94	8.34	3320.91	3310.74	0.31
$[\pm45,0,\pm75,0_2,90]_s$	114.51	115.61	0.97	32.81	34.47	5.06	3539.91	3317.23	6.29
$[\pm45,0,90_2,\pm30,90]_s$	132.26	115.49	12.68	29.04	33.66	15.93	3155.00	3382.03	7.20

Table 5.8: Selected results metrics from the radial-based function neural network optimization and their computed and predicted crashworthiness metrics. The disregarded designs that do not meet the constrained values upon computation are marked in red.

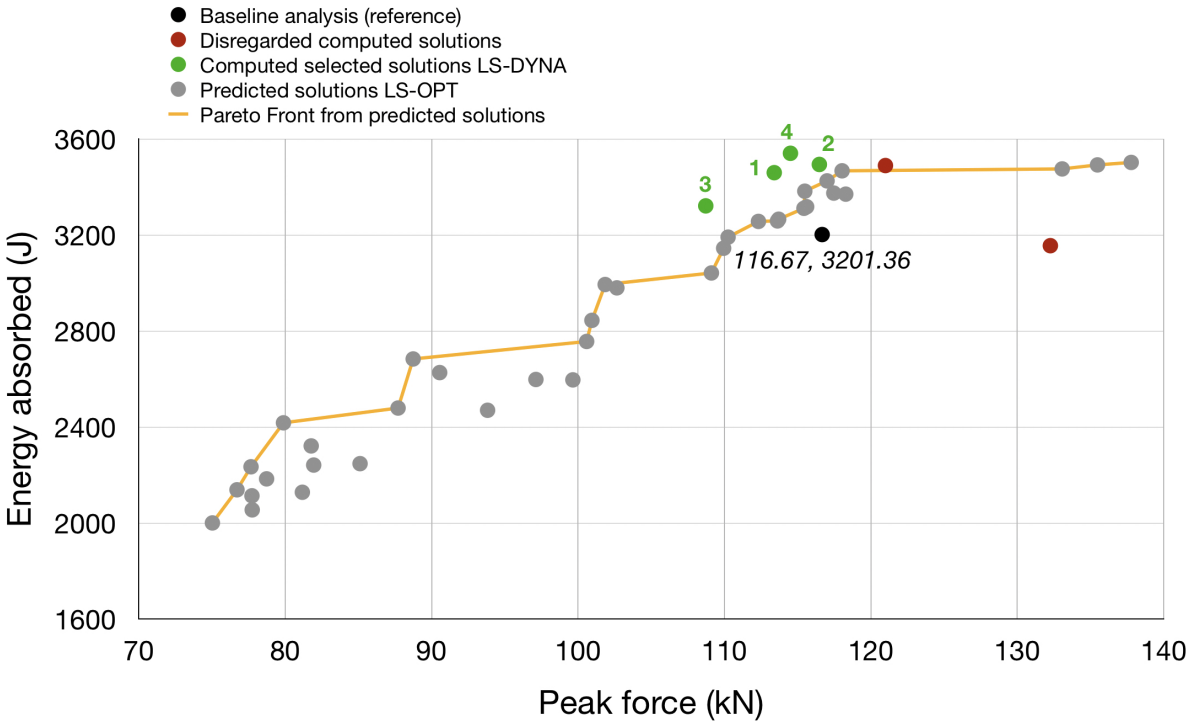

Figure 5.4: EA versus F_{peak} optimization objectives using a feed forward neural network metamodel. The predicted design solutions from LS-OPT build a Pareto front, while including the baseline analysis for reference and the selected and disregarded solutions computed in LS-DYNA.

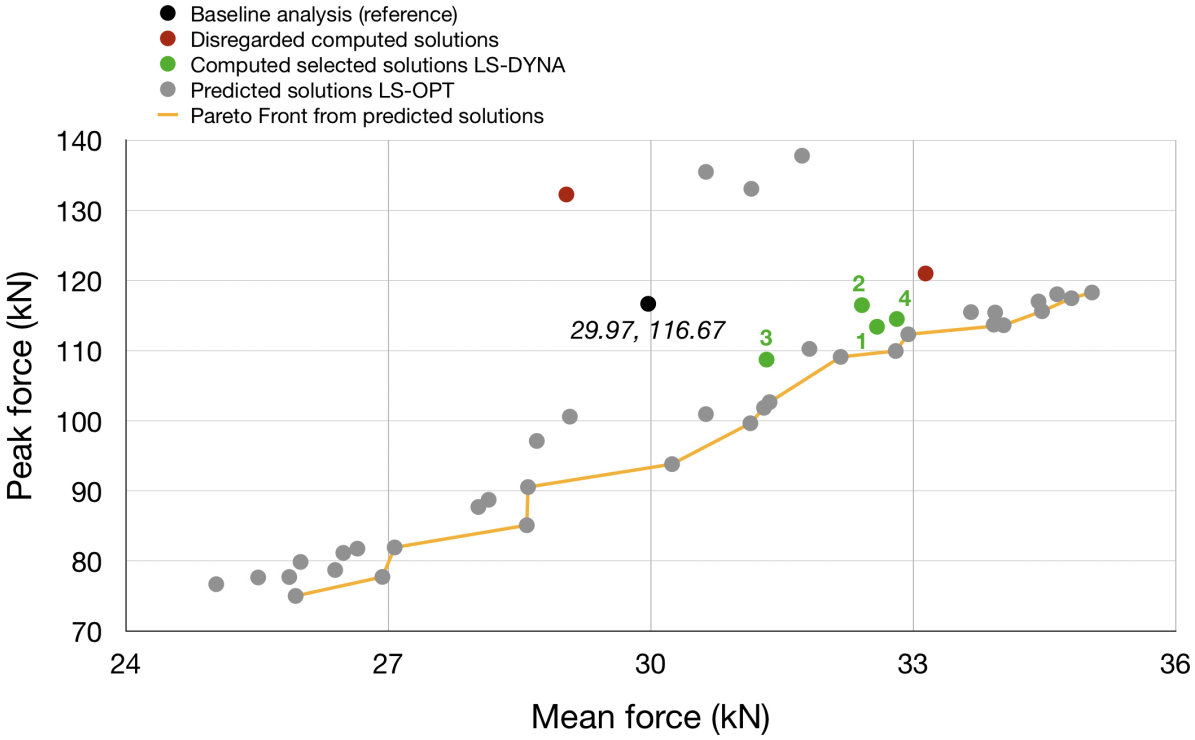

Figure 5.5: F_{peak} versus F_{mean} optimization objectives using a feed forward neural network metamodel. The predicted design solutions from LS-OPT build a Pareto front, while including the baseline analysis for reference and the selected and disregarded solutions computed in LS-DYNA.

The optimum tube design must be above the Pareto front curve from Figure 5.4 and below the one from Figure 5.5. The issue here is that all selected designs (in green) are placed above the Pareto front in both graphs, meaning that the optimum design should be as close to the Pareto front in Figure 5.5 as possible. This can be done by searching for the lowest prediction errors for the peak and mean forces from Table 5.8, which concludes that the optimum tube's design is design number 1 with $[\pm 45, 0, \mp 75, \pm 15, 90]_s$ layup.

5.2.5 Choosing the best metamodel optimization

After both metamodel optimizations are performed in the previous sections, it can be concluded that both of them lead to the same layup for the tube's optimum crashworthiness design. $[\pm 45, 0, \mp 75, \pm 15, 90]_s$ is the final layup. Nonetheless, the setup differs from the feed-forward neural network to the radial-based function neural network. This difference can lead to a difference in prediction, making one of the metamodel optimizations less accurate than the other. Therefore, to know which metamodel is most suitable for this crashworthiness optimization, their computed and predicted metrics for each optimization objective are presented in Table 5.9. Both optimizations were executed on the same PC and under the same conditions. Despite this, the radial-based neural network takes one full iteration longer to converge to an optimal solution, which is 3-4 hours of extra computation time.

Metamodel	**F_{peak}**			**F_{mean}**			**EA**		
	LS-DYNA value (kN)	LS-OPT value (kN)	|Error| (%)	LS-DYNA value (kN)	LS-OPT value (kN)	|Error| (%)	LS-DYNA value (J)	LS-OPT value (J)	|Error| (%)
FFNN	112.89	112.63	0.24	32.88	34.05	3.55	3477.24	3344.22	3.83
RBF NN	113.40	113.62	0.20	32.59	34.03	4.44	3459.20	3258.16	5.81

Table 5.9: Tube's optimum layup and its crashworthiness metrics resulting from both neural network metamodel optimizations.

Table 5.9 presents that feed-forward neural network metamodel optimization has lower relative errors in two out of the three objectives, and the remaining objective's prediction error is not significantly higher than for

the radial based metamodel. Additionally, the feed-forward neural network optimization takes less time to converge to a solution for the tube's crashworthiness problem and provides a slightly better representation of the energy absorption response according to Table 5.4. Hence, the feed-forward neural network can be concluded as the metamodel optimization with the best predictions. This aligns with the already mentioned feature provided by LS-OPT's manual [54], stating that this metamodel is suitable for non-linear problems such as this one.

5.3 Crushing tube comparison: baseline versus the optimized design

This section concludes the chapter by comparing the final baseline analysis from Chapter 4 and the optimum design resulting from the previous section. This comparison is based on how much the three optimization objectives or crashworthiness metrics of EA, F_{peak} and F_{mean}; have improved in comparison to the reference. This difference in values is presented in Table 5.10, using computed values from both LS-DYNA analyses.

Design	**Layup**	$\mathbf{F_{peak}}$ (kN)	Δ (%)	$\mathbf{F_{mean}}$ (kN)	Δ (%)	**EA** (J)	Δ (%)
Baseline	$[0_2, \pm 45_2, 90_2]_s$	116.67	-	29.97	-	3201.36	-
Optimized	$[\pm 45, 0, \mp 75, \pm 15, 90]_s$	112.89	-8.41	32.88	9.47	3477.24	8.53

Table 5.10: Improvement of crashworthiness metrics from the baseline tube design to the final optimized design LS-DYNA analyses.

Table 5.10 proves that the optimized layup improves all three crashworthiness metrics of the tube by a percentage superior to 8% with respect to the baseline. Despite this, the crushing mechanism of the tube might have changed along with the layup, leading to a different force-displacement graph. Therefore, the physical crushing mechanism in each case is shown and evaluated from Figure 5.6, Figure 5.7 and Figure 5.8.

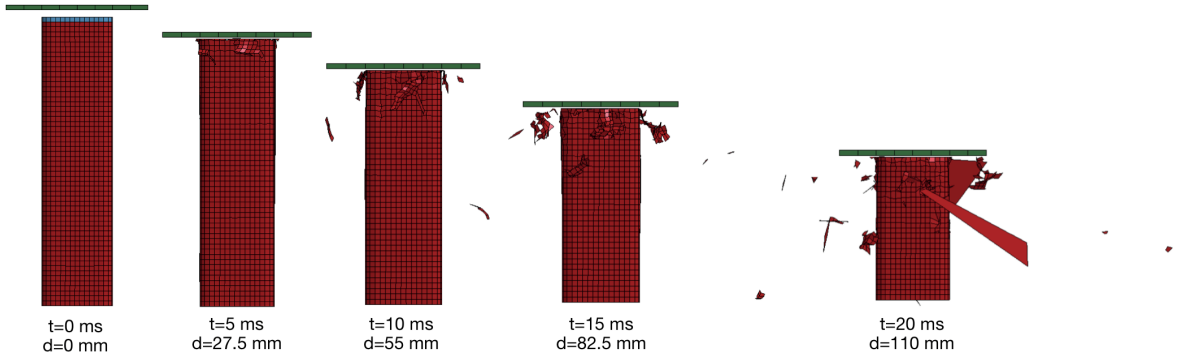

Figure 5.6: Crushing mechanism for the baseline tube design. Caption of the sequence taken every 5ms of simulation with their relative displacements.

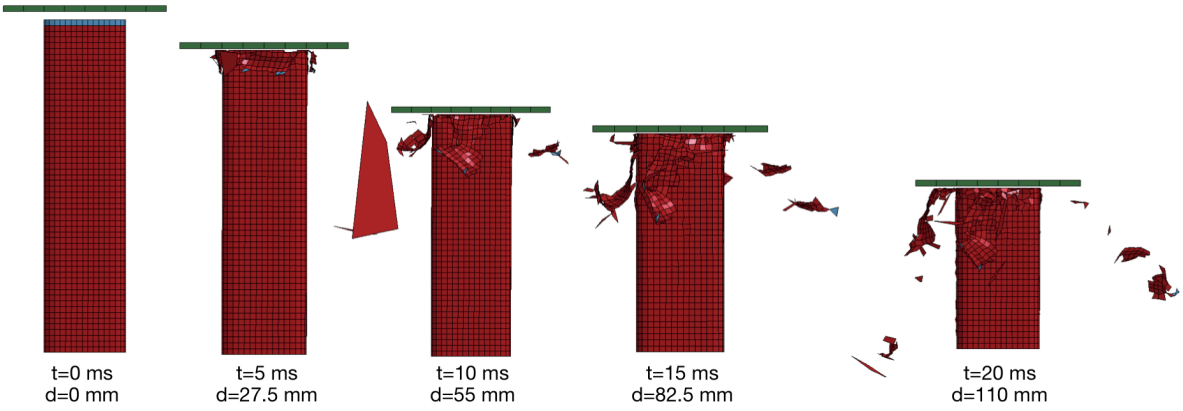

Figure 5.7: Crushing mechanism for the optimized tube design. Caption of the sequence taken every 5ms of simulation with their relative displacements.

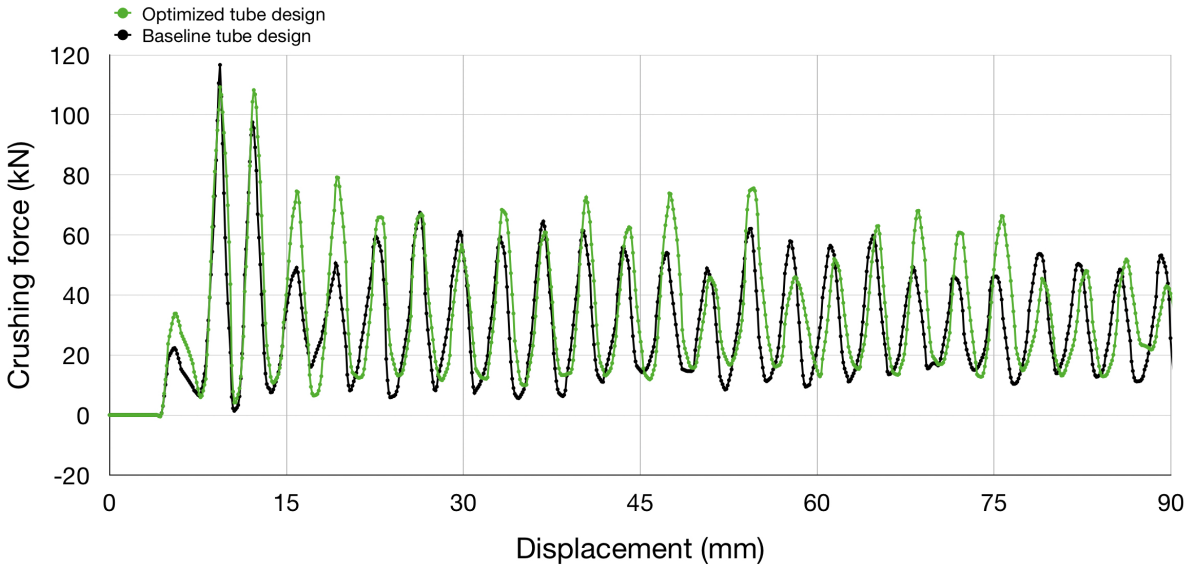

Figure 5.8: Force-displacement graph for both the baseline and the optimized designs of the tube.

The crushing sequences shown in Figure 5.6 and Figure 5.7 share the same deformation mechanisms, yet the sequences differ from one another as expected. The optimized design starts crushing earlier, which is why its progressive damage releases more bits of the tube that detach upon crushing. This crushing mechanism, as explained in Chapter 2, is known as fragmentation. In Figure 5.7, it is also possible to visualize some fiber splaying when the tube crushes in displacements beyond 55 mm. Additionally, the force-displacement curve from the optimized design in Figure 5.8 has an increased area below the curve caused by the increase in oscillations size right after the peak force, causing the tube's fragmentation to start earlier as mentioned for Figure 5.7. This increases the second peak of force, which is unwanted in crashworthiness applications. The increased oscillations also generate a higher mean force, as proven in Table 5.10. Regardless, the highest peak force is lower in the optimized design curve than the baseline, which is one of the optimization objectives.

After the reasoning above and seeing Figure 5.6, Figure 5.7 and Figure 5.8; it can be concluded that the optimized design offers some flaws such as the high second peak force in Figure 5.8. Nonetheless, the positive changes in crashworthiness metrics surpass their negative consequences. Therefore, the optimum stacking sequence design can be implemented in the STUNNING fuselage section in future chapters to verify this one's improving the fuselage's crashworthiness as well.

5.4 Computation time

The optimizations performed in this chapter are performed in LS-OPT at the PC assigned by the aerospace faculty: TUD211793. This makes the optimizations last a bit longer, limited to the PC capacity. For the feed-forward neural network optimization, the fifth iteration is reached when using 10 sampling points in each one. The total time spent in this optimization surpasses the day (about 24-30h) until convergence to provide the optimal results. As for the radial-based function neural network optimization, this one uses the same amount of sampling points per iteration but converges in the sixth iteration. This causes the optimization to last about 40h until convergence.

Both optimizations are calculated simultaneously, which is possible in LS-OPT but limits the PC capacity destined for each computation. In other words, the split capacity for both optimizations makes these take longer to perform. Therefore, the mentioned times spent on each computation could have been slightly reduced when executing one optimization at a time.

Chapter 6

Crash analysis of a fuselage section

The goal of this chapter is to see whether or not the optimized stacking sequence of the tube obtained in Chapter 5 improves the crashworthiness of the STUNNING fuselage. Due to the increased weight of the fuselage file and the extra computational cost that this one brings to LS-DYNA analysis on a PC, the fuselage analyses performed in this chapter are executed locally on the PC, and in the high performance computing cluster *hpc12* from the faculty.

6.1 STUNNING fuselage

The fuselage section to study in this chapter is borrowed from the STUNNING project, which simplifies digitally the Next Generation Multifunctional Fuselage demonstrator from the Clean Sky initiative [3, 4, 5]. The digital version of the fuselage consists of a sub-floor section from below the passenger's cabin, which contains straight and curved beams to keep an arched shell shape in its outer structure. This section represents the central part of the fuselage and has a capacity of six passengers and their luggage in the cargo area [4], but no payload is included yet in the model to represent these or the upper part of the fuselage section. The initial fuselage section design has four C-struts added between the cargo floor and the frames, as shown in Figure 6.1. Those struts have a length of 378 mm, a flange width of 26 mm and a web height of 90 mm. The four of them are fixed from their top to the cargo cross-beam, and their bottom to the fuselage's frame [4]. Consequently, the struts influence how the fuselage frame and the cargo beam crush in a survivable impact of 30 ft/s.

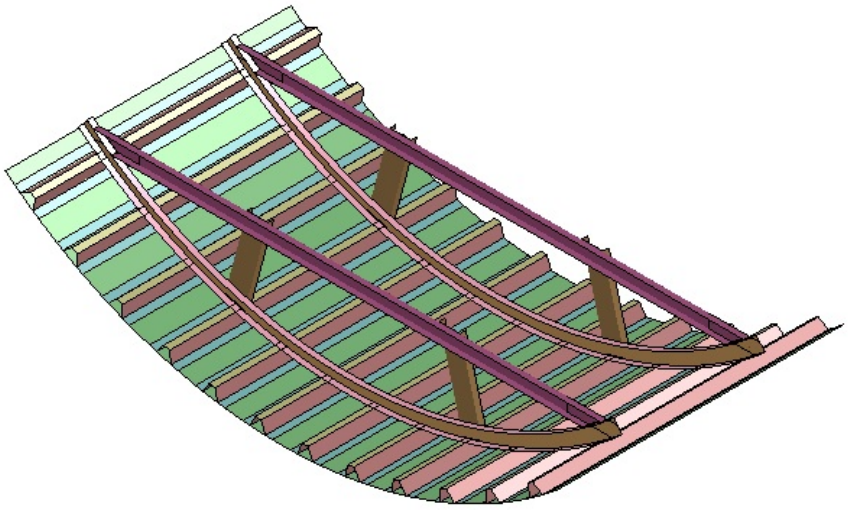

Figure 6.1: STUNNING fuselage section model.

The predominant material of the fuselage's section is the thermoplastic composite Toray Cetex TC1225, whose physical and mechanical properties can be found on Table 6.1. This is part of the Clean Sky initiative to use a thermoplastic fuselage section to make more sustainable aircraft designs and their production [3, 5]. The impactor and the metal plates of 1 mm thick present on the fuselage section are the exception. There are four metal plates on the fuselage section, which are made of aluminum alloy AA6111 T4. The elastic physical and mechanical properties of this one are listed in Table 6.2. Both materials' properties for the thermoplastic composite and the aluminum alloy are inherited from Poorte's work [4].

Property	Value	Units
Density (ρ)	$1.59 \cdot 10^{-6}$	k/mm^3
Ply thickness (t_{ply})	0.184	mm
Longitudinal Young's modulus (E_A)	143	GPa
Transverse Young's modulus (E_B)	8.8	GPa
Longitudinal Shear modulus (G_{AB},G_{CA})	4.3	GPa
Transverse Shear modulus (G_{BC})	3.4	GPa
Longitudinal Poisson ratio (ν_{AB})	0.0185	-
Longitudinal compression strength (X_C)	1.089	GPa
Longitudinal tensile strength (X_T)	2.755	GPa
Transverse compression strength (Y_C)	0.248	GPa
Transverse tensile strength (Y_T)	0.078	GPa
Shear strength (S_C)	0.048	GPa
Maximum longitudinal tensile strain ($\epsilon_{11,T}$)	0.019	mm/mm
Maximum longitudinal compression strain ($\epsilon_{11,C}$)	0.008	mm/mm
Maximum transverse tensile strain ($\epsilon_{22,T}$)	0.009	mm/mm
Maximum transverse compression strain ($\epsilon_{22,C}$)	0.028	mm/mm
Maximum shear strain (GMS)	0.05	mm/mm

Table 6.1: Toray Cetex TC1225 physical and mechanical properties, data obtained from previous work [3, 4].

Property	Value	Units
Density (ρ)	$2.89 \cdot 10^{-6}$	k/mm^3
Young's modulus (E)	70.5	GPa
Poisson ratio (ν)	0.34	-
Yield stress (σ_y)	0.1921	GPa

Table 6.2: AA6111 T4 physical and mechanical properties, data obtained from previous work [3, 4].

6.1.1 Components and material models

The STUNNING fuselage section is represented in LS-DYNA as a finite element model with an impactor to represent the floor where the structure crashes. The model uses the two mentioned materials for the fuselage section, Toray Cetex TC1225 and AA6111 T4, and an additional rigid material model for the impactor plate. The composite material is modeled using MAT_058, which requires additional non-physical properties, as explained in Chapter 3 and Chapter 4. These non-physical properties introduced in LS-DYNA for the fuselage's thermoplastic components are as presented in Table 6.3.

The aluminum alloy is introduced as a transversely anisotropic elastic-plastic material using extended hardening. The material card MAT_TRANSVERSELY_ANISOTROPIC_ELASTIC_PLASTIC uses an anisotropic hardening parameter (R) of 2.214, and an introduced curve to describe the material's behavior within the plastic region. Lastly, the rigid material properties from the inherited model are listed in Table 6.4, which correspond to the theoretical mild steel alloy properties.

The finite element model that represents the fuselage section consists of six different parts: the skin, the stringers, the frames, the cargo crossbeams, the metal plates that join each cargo beam to a frame, and finally, the struts. Some parts are divided into sections to simplify the model. The omega stringers are modeled

in three different parts. First, the stringer top is modeled separately from the sides and the flanges that are joined to the fuselage skin. Therefore, the stringer top is modeled on its own, and so do its sides. As for Part 1010, the stringer and skin junction is considered a unique thicker metal plate. Something similar happens to the frame, which presents a C-shape cross-section. Hence, its web is modeled separately from its flanges and then put together to interact upon crushing. The remaining fuselage components are modeled as a whole, which amounts to a total of nine parts in the fuselage model. Figure 6.2 presents all of them and includes the impactor plate that causes the crushing of the fuselage.

Property	Value	Units
TSIZE	10^{-7}	s
ERODS	-0.55	mm/mm
SLIMT1	0.01	GPa/GPa
SLIMC1	0.6	GPa/GPa
SLIMT2	0.1	GPa/GPa
SLIMC2	1	GPa/GPa
SLIMS	1	GPa/GPa

Table 6.3: LS-DYNA non-physical parameters for *MAT_058_LAMINATED_COMPOSITE_FABRIC* fuselage components. Values taken from Poorte, p.87 [4].

Property	Value	Units
ρ	$7.85{\cdot}10^{-6}$	kg/mm
E	210	GPa
ν	0.3	-

Table 6.4: *MAT_RIGID* properties from the inherited model's impactor.

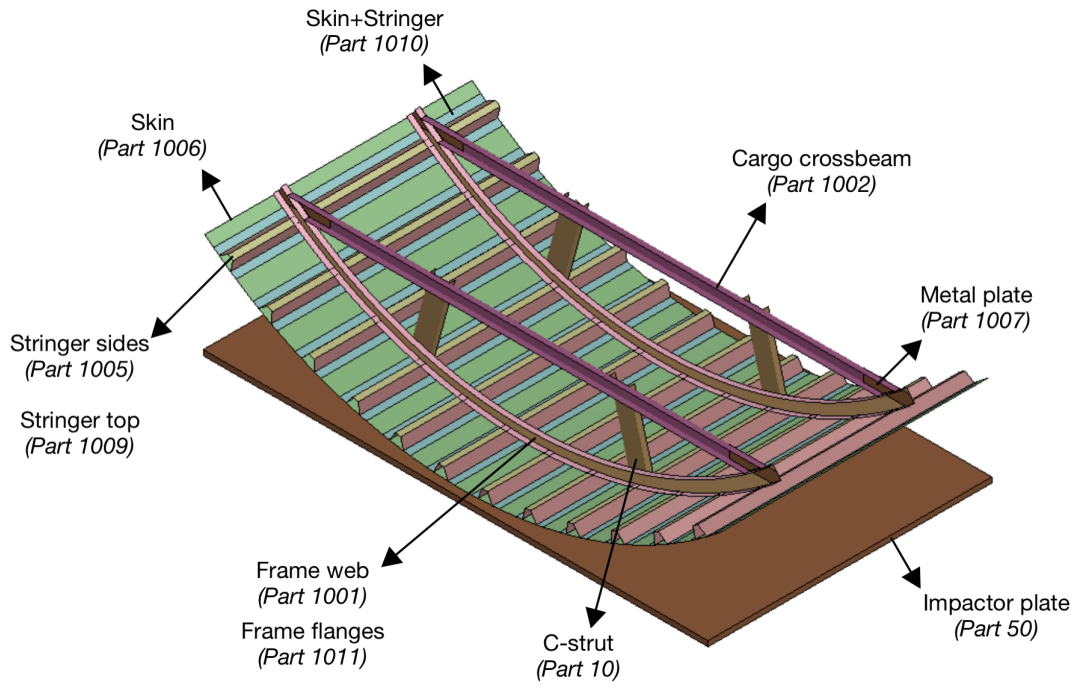

Figure 6.2: Differentiated parts from the STUNNING fuselage section. Model inherited from [3, 4].

The parts from Figure 6.2 that are modeled with Toray Cetex TC1225 material are the fuselage's skin, stringers, frames, struts, and cargo crossbeams. The 1 mm metal thick plates are the only parts of the fuselage modeled with aluminum alloy AA6111-T4 with the extended hardening.

6.1.2 Element formulation

The entire fuselage section gets damaged upon crushing, which requires its components to use shell elements to simplify the model. All the parts using shell elements have the Belytschko-Tsay formulation in them with Reissner-Mindlin kinematics [4]. Among those parts, the struts are the component of interest in this thesis. The struts have a mesh size of 4 mm, which is an acceptable size in terms of analysis accuracy according to Boria et al.'s mesh sensitivity study [58]. The only part from Figure 6.2 that does not use shell elements is the impactor plate. This plate is modeled as a single solid element, whose crushing representation is more subtle than shell elements throughout the whole crushing simulation [8].

6.1.3 Boundary conditions

The fuselage section is clamped from its top corner nodes, which prevents the frame and skin to move upwards upon crushing. The crushing condition in the LS-DYNA model is set through a prescribed motion boundary condition. This prescribed motion introduces a constant velocity curve of 10 mm/ms (30 ft/s) to the impactor plate to follow throughout the simulation. This constant speed curve makes the plate move upwards along the positive Z-axis during the 30 ms of simulation [4].

Finally, there is a boundary condition added to each end of the fuselage section so that the totality of the fuselage's structure is considered. The fuselage length is supposed to go along the X-axis, which means that the ends where the boundaries are set to correspond to Edges L and R, drawn in Figure 6.3. Upon crushing, these edges are blocked from the translation movement in the X-axis to represent the behavior of the entire fuselage structure along that axis. Additionally, the rotation movements in the perpendicular Y and Z axes are also restricted for the section of the study. These boundary conditions are drawn and placed in Figure 6.3.

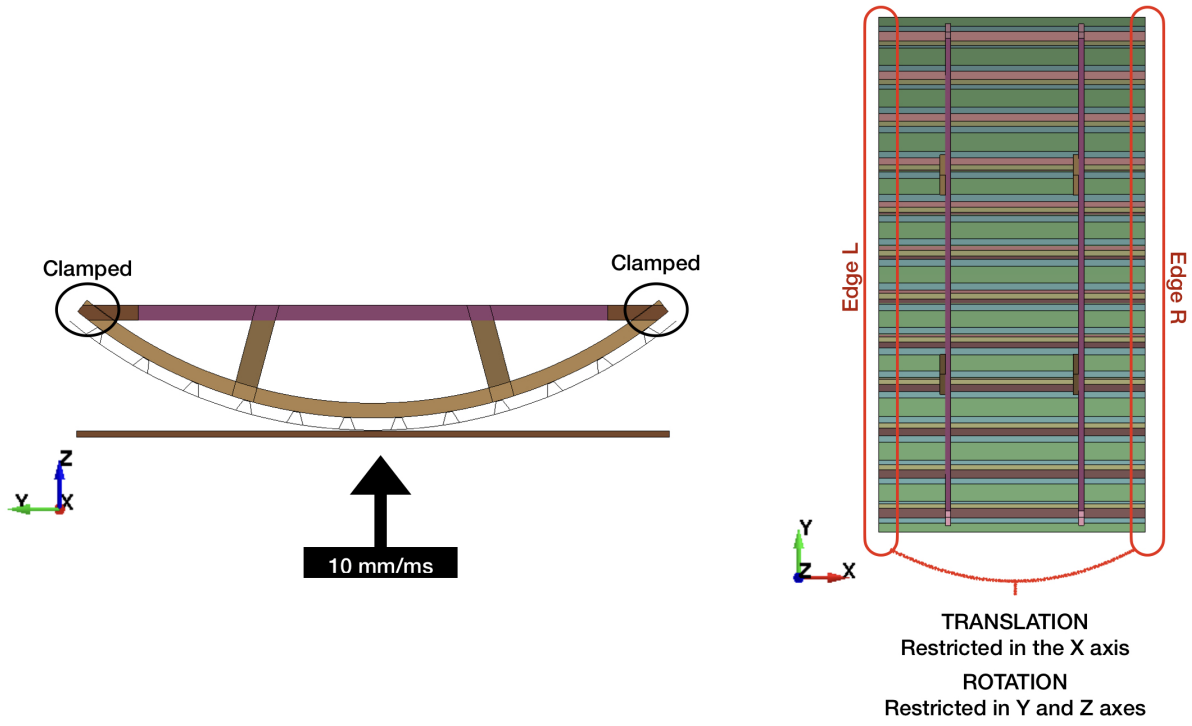

Figure 6.3: Boundary conditions applied to the STUNNING fuselage section. Front view (left) and top view (right) of the fuselage section indicated.

6.1.4 Contacts

To represent the crushing phenomena, the entire model is considered as a single part set so that each component interacts with its surroundings with the assigned keyword CONTACT_AUTOMATIC_GENERAL_ID. When applying these contact conditions, the only coefficients with values different than zero are the static

friction and the viscous damping coefficient in percent critical. The coefficient and percentage are 0.2 and 20, respectively. In addition to this condition, the parts in contact with one another use separate conditions using the keyword CONTACT_TIED_SHELL_EDGE_TO_SURFACE. This contact condition uses a master-slave dynamic among each pair of components, where the master exerts the contact onto the slave. The pairs of components that use this condition are the frame web (master) to the metal plate (slave), the struts' top to the cargo crossbeams, the strut's bottom to the frame, and the cargo crossbeams to the metal plates on their ends. The same contact condition is applied with an offset (keyword CONTACT_TIED_SHELL_EDGE_TO_SURFACE _OFFSET) to the stringers' contact with the frame. See Figure 6.2 for further clarity on the parts' contact.

Lastly, the *CONTACT_FORCE_TRANSDUCER_PENALTY_ID* keyword is assigned to the entire model part set to register the contact forces that the impactor plate exerts onto the fuselage during the crash. This keyword has no physical significance for the model but aids the existent contact conditions to quantify the forces generated upon them. These forces are taken from the impactor plate to generate the force-displacement graphs of the post-processing in future sections, as done in Chapter 4 with the tube analysis.

6.2 STUNNING fuselage analysis

The model described in the previous section is executed in Poorte's thesis using LS-DYNA R7.0.1 [4]. This analysis is reproduced again on the PC locally with the same version of LS-DYNA as a reference since the *hpc* cluster from the faculty does not have the same version available. After the analysis performed on the PC, the crashworthiness behavior of the fuselage is studied by generating a force-displacement and energy graphs. These are generated by filtering the force-displacement graph with a SAE filter and a cut-off frequency of 600 Hz. The energy graph is generated by integrating the force-displacement graph with LS-DYNA's post-processing tools. Figure 6.4 and Figure 6.5 resulting graphs match the orange curves from page 111 in Poorte's thesis [4], which means that both analyses provide the same results as a reference.

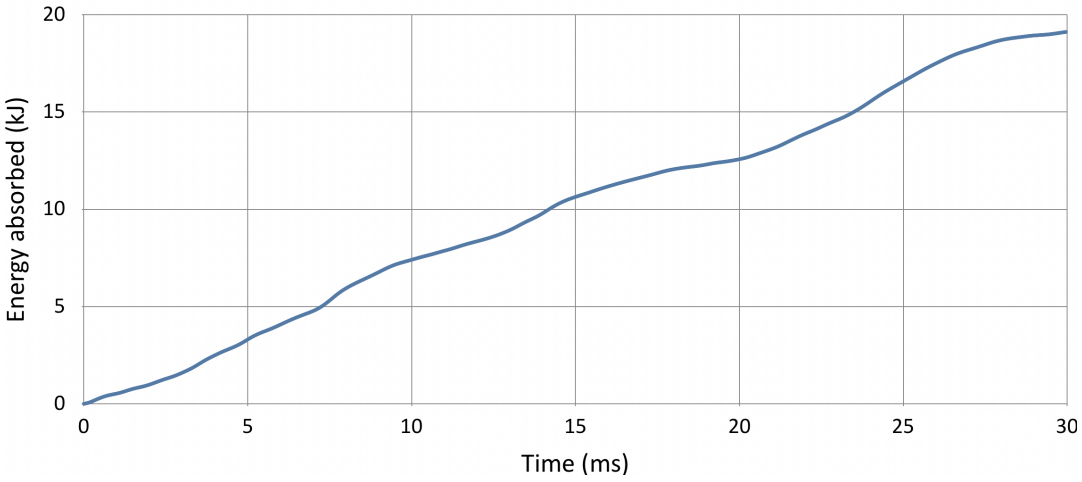

Figure 6.4: Energy absorbed over time in the local analysis of the original STUNNING fuselage configuration.

According to Figure 6.4, the fuselage model described in the previous sections absorbs about 19 kJ of energy during the crash. This energy absorbed is accumulated in the structure along the 30 ms of simulation. The fuselage model also presents less stabilized oscillations in Figure 6.5 than the ones presented in Chapter 4 and Chapter 5 for the tube analyses. For instance, in the force-displacement graph, the first oscillation does not present the highest force experimented by the structure, as this one appears later in the crushing procedure. This happens when the impactor crushes the fuselage section, for a displacement of 70 mm in Figure 6.5, resulting in a peak force of 140 kN. As for the second highest peak, this one occurs by the end of the graph, when the impactor starts crushing the struts for a displacement beyond 240 mm.

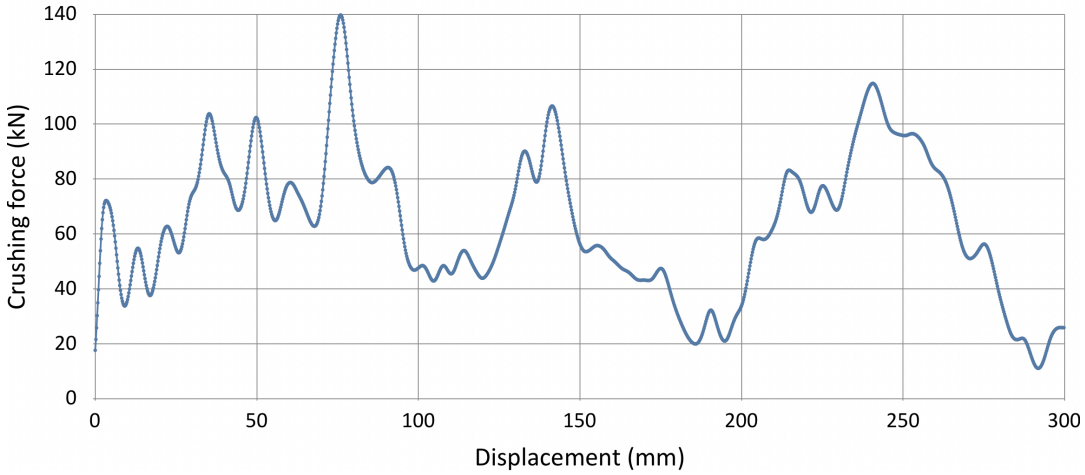

Figure 6.5: Crushing force over time in the local analysis of the original STUNNING fuselage configuration.

The results from the fuselage analysis using LS-DYNA R7.0.1 might change when using the program's cluster version. The *hpc12* faculty cluster has four versions of the program, all more updated than the R7.0.1. The versions available are R9.3.1, R10.0.2, R11.1.0, and R12.0.0. According to LS-DYNA manuals, the more updated the version, the more changes these present in comparison with a prior version of the program [8, 9]. Hence, LS-DYNA R9.3.1. is used for the cluster analyses from this point onward, using a setup of one node with four processors, and four central processing units (CPU). The change in version and environment is assumed to be significant enough to analyze the difference in results between the two fuselage analyses. First, the changes in final energy values are reflected in Table 6.5 between Porte's simulation results (Table E.8, p.159 in Poorte's thesis [4]).

Part	**Total energy (J)**		**Internal energy (J)**		**Kinetic energy (J)**		**Hourglass energy (J)**		**Damage energy (J)**	
	R7.0.1	R9.3.1	R7.0.1	R9.3.1	R7.0.1	R9.3.1	R7.0.1	R9.3.1	R7.0.1	R9.3.1
Part 1001	4241.6	3893.2	3952.4	3681.0	279.9	210.6	133.6	40.1	235.6	251.1
Part 1002	482.1	608.3	373.5	451.1	106.7	155.4	18.8	6.4	0	0
Part 1005	1548.1	1451.7	985.3	862.0	566.1	594.8	14.0	6.7	0	0
Part 1006	3674.0	3680.1	2838.5	2843.2	834.7	835.6	2.8	1.4	0	0
Part 1007	121.4	158.7	117.6	155.2	3.6	2.8	0.1	0.2	0	0
Part 1009	559.4	515.2	402.3	356.8	158.4	158.6	9.1	3.9	0	0
Part 1010	813.8	934.9	206.5	320.4	611.6	615.0	2.4	1.1	0	0
Part 1011	3951.9	3631.7	3624.7	3383.3	322.1	246.0	38.9	96.2	1039.5	301.2
Part 10	9894.6	1753.9	1299.5	1499.7	8580.0	260.5	82.5	37.8	1081.8	1227.9

Table 6.5: Final total, internal, kinetic, hourglass and damage energy values of the STUNNING fuselage section parts. Resulting values from both LS-DYNA versions, using the fully fixed absorbers configuration.

Table 6.5 shows the resulting total, internal, kinetic, hourglass, and damage energies registered at the end of the crushing simulations for each LS-DYNA software version. The table represents the change in results between analyses with the same setup but different software versions. For most parts, the magnitude of the total, internal and kinetic values are kept the same in both R7.0.1 and R9.3.1. The hourglass and damage

(or internal eroded) energies present a larger variance. Considering the internal and kinetic energies to be the main components of the energy absorbed by the fuselage section, the changes presented in Table 6.5 are not large enough to consider a change in the crash dynamics of the structure. This must be checked with Figure 6.6 and Figure 6.7, which present the change in crash kinematics of the cluster's LS-DYNA R9.3.1 simulation against the results obtained on the PC.

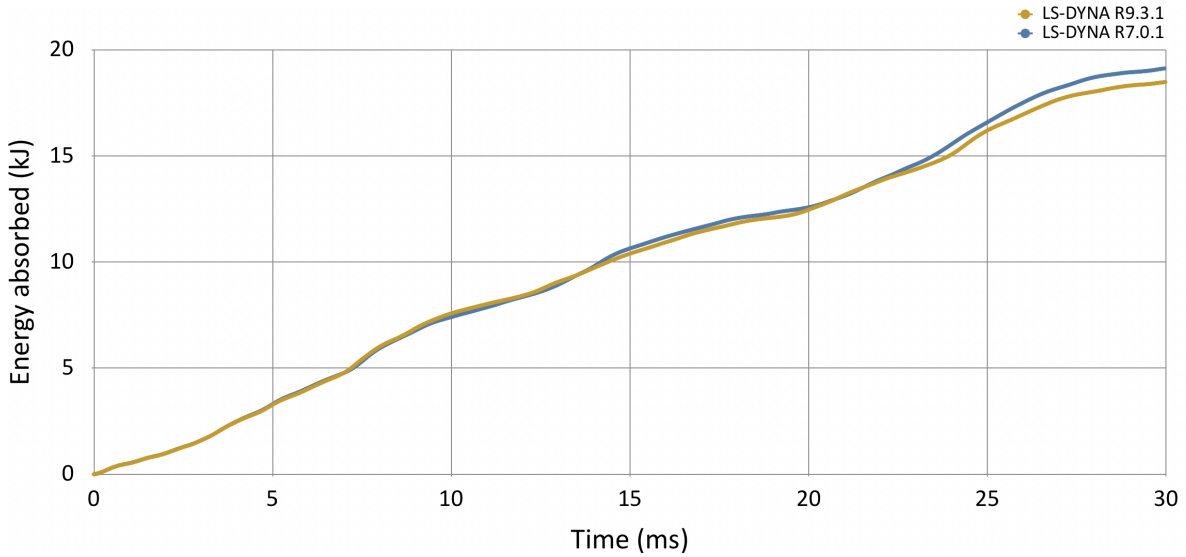

Figure 6.6: Energy absorbed of the original STUNNING fuselage resulting from the two LS-DYNA versions from the PC and *hpc12* cluster. 4 CPUs are considered in both cases.

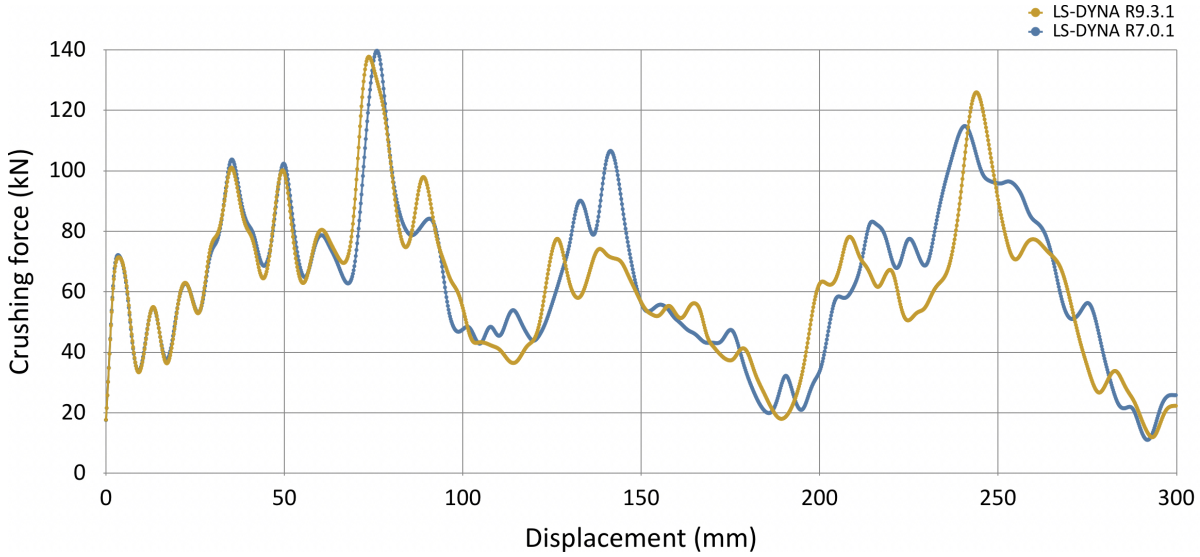

Figure 6.7: Force-displacement graph of the original STUNNING fuselage resulting from the two LS-DYNA versions from the PC and *hpc12* cluster. 4 CPUs are considered in both cases.

Figure 6.6 shows that the fuselage analysis from LS-DYNA R9.3.1 absorbs slightly less energy than the PC LS-DYNA version, yet the difference is not significant (less than 1 kJ). The graph also shows a flatter slope by simulation time 20 ms, which coincides with the region in Figure 6.7 of lowest crushing force and spaced oscillations. In Figure 6.7, the curve provided by the cluster simulation resembles immensely up to the highest peak force. After that, the curve presents lower peaks of force for a displacement over 150 mm and up to the second-highest peak. Nonetheless, the pattern of both curves is quite similar, which confirms the hypothesis that both LS-DYNA versions do not present large differences in terms of crashworthiness metrics. Therefore, LS-DYNA R9.3.1 is chosen as the software version to perform the fuselage analyses for the remaining chapters.

6.3 Fuselage square strut configuration analysis

This section introduces the square struts into the STUNNING fuselage in place of the C-struts. According to Poorte's thesis, out of the four strut configurations studied (C-struts with fixed and free bottom ends and square struts with the same bottom end setups), the one that provides the best crashworthiness behavior is the square strut configuration with free bottom ends [4]. This is supported by literature, where square cross-section composite tubes are said to absorb energy better in crash applications due to their progressive deformation [4, 12, 19, 32]. The difference between the squared free-end strut fuselage and the model presented at the beginning of the chapter is the shape of the strut (from C-shape to square), and the removed contact condition between the strut bottom end and the frame web. This means that the fuselage model from Figure 6.1 has C-strut with fixed bottom ends, while the square strut configuration with free bottom ends is shown in Figure 6.8. The square cross-section of the struts is 36.8 mm per side, has round fillets and $[\pm 45, 0_2, 90, \pm 45, 90, 0_2, \pm 45]$ for layup [4].

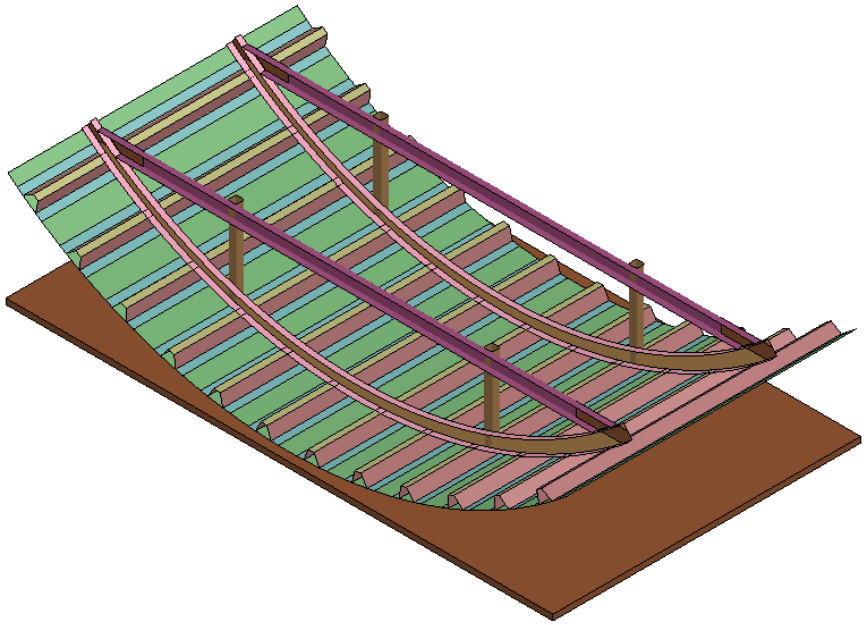

Figure 6.8: Fuselage section with square struts and free bottom ends.

The fuselage model from Figure 6.8 is analyzed in this section using LS-DYNA R9.3.1 from the cluster. This analysis sets the reference when introducing the optimum layup from Chapter 5 into the square struts of the fuselage in the next section. The resulting force-displacement and energy absorption graphs are shown in Figure 6.9 and Figure 6.10 to evaluate this particular model's crashworthiness. Both graphs use a SAE filter with a cut-off frequency of 600 Hz. These show the results of the square strut with free bottom ends' configuration in comparison with the original STUNNING fuselage, whose results have been already presented in Figure 6.4 and Figure 6.5. This is done to set the difference between both fuselage models.

Both Figure 6.9 and Figure 6.10 confirm that the square strut configuration is a slightly better energy absorber than the original fuselage model described above, as shown in Figure 6.9. It is also shown how the slope is relatively constant in the new fuselage configuration, which was not the case for the C-strut configuration, as explained in the previous section. This constant slope comes from Figure 6.10 central part of the graph, which presents higher crushing force values than the C-strut configuration, yet it is bound below 140 kN. This makes the square strut configuration good in terms of crashworthiness, and aligns with Poorte's conclusions [4]. The crushing sequences of both fuselage configurations are shown in Figure 6.11 Figure 6.12 to support this conclusion.

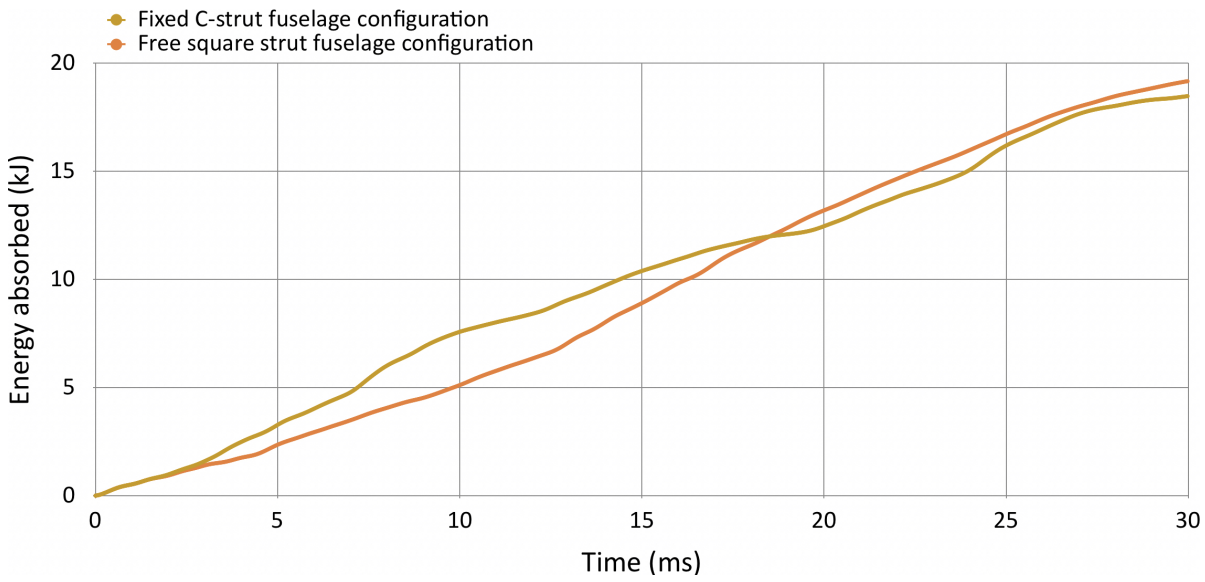

Figure 6.9: Energy absorbed by the fuselage for the square strut with free ends' configuration, and the original STUNNING fuselage.

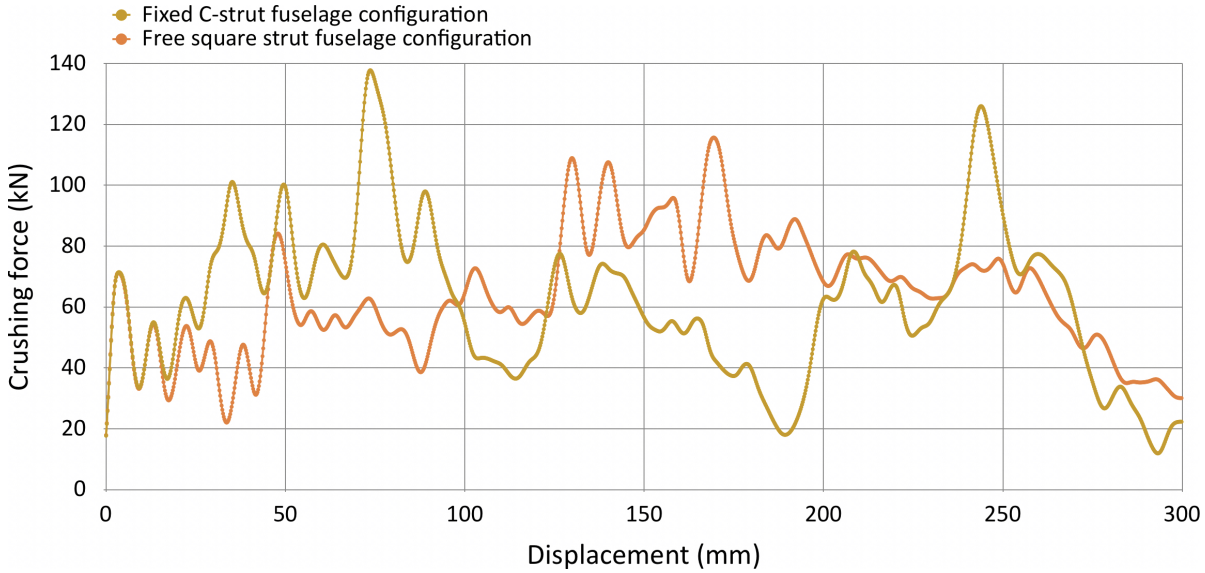

Figure 6.10: Force-displacement curve for the fuselage for the square strut with free ends' configuration, and the original STUNNING fuselage.

The fuselage crushing mechanisms from Figure 6.11 and Figure 6.12 differ from one another as a result of their bottom struts' contact condition removal and their change in geometry. The fully fixed C-strut configuration in Figure 6.11 shows a fuselage that deforms further throughout the crash simulation, which is due to the struts getting damaged earlier on the sequence at 10 ms. The C-struts also end up completely detached from the cargo crossbeam and smashed after the crash. A similar end is met in Figure 6.12 for the square struts, except for these not being as damaged. The square struts limit the crushing initiation at the bottom skin of the fuselage, making the fuselage bend by its central part of the cargo area by 20 ms. The downside of this is that the deformation acts upon the cargo crossbeams and pushes them upwards as the fuselage deforms, which is not presented on the C-struts. Nonetheless, neither Figure 6.11 and Figure 6.12 include a plate or a mass representing the luggage that would go on a commercial flight in the cargo area, nor the weight of the passengers and equipment from the upper part of the fuselage. Hence, the improvement of crashworthiness properties seen in Figure 6.9 and Figure 6.10 is assumed to be good enough to perform future analyses with square struts, despite the crushing sequence from Figure 6.12 lacking real scenario representation.

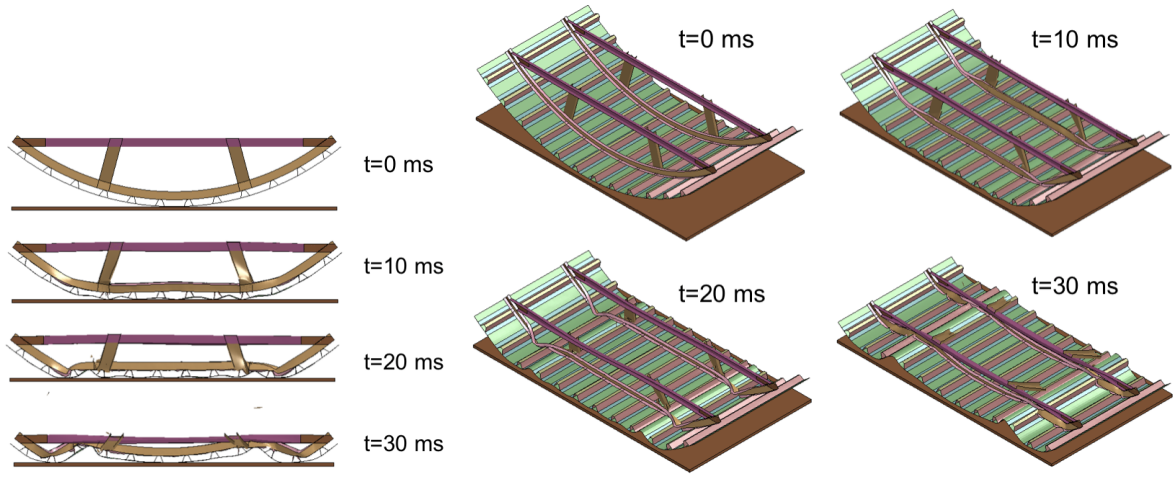

Figure 6.11: Crushing sequence of the fuselage with fully fixed C-struts: front view (left) and isotropic view (right).

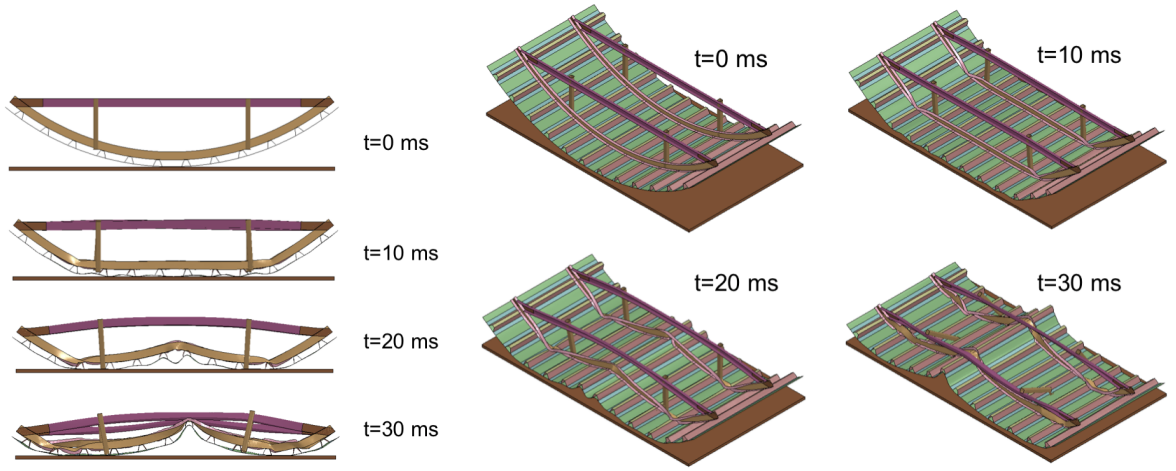

Figure 6.12: Crushing sequence of the fuselage with square struts and free ends at their bottom: front view (left) and isotropic view (right).

6.4 Fuselage analysis with struts' optimized layup

This final section introduces the optimum layup from the square tube in Chapter 5 to the previous square strut fuselage analysis. In the previous section, the square struts were 36.8 mm per side and had per layup $[\pm 45, 0_2, 90, \pm 45, 90, 0_2, \pm 45]$. The new simulation with Chapter 5's optimum layup $[\pm 45, 0, \mp 75, \pm 15, 90]_s$, must have the same mass per strut (179.4 g). Therefore, this analysis has square struts of 28.8 mm per side to compensate for the extra plies present in the introduced layup. The crashworthiness behavior of the fuselage's new configuration is evaluated through force-displacement and energy absorption graphs in Figure 6.13 and Figure 6.14, respectively. The results from the previous analysis are also included to see whether or not the change in layup improves the crashworthiness of the fuselage.

The fuselage design with the new stacking sequence is slightly better at absorbing energy during the crash, according to Figure 6.13. This is due to the peaks of force increasing about 20 kN with respect to the previous analysis (the baseline layup strut design). Especially for displacements beyond 100 mm in Figure 6.14, where peaks are slightly higher but longer, elongating the effects of the crush from reaching upper parts of the fuselage that could cause further structural damage and occupants' injuries. Up until then, both fuselage models absorb energy in a very similar way (see Figure 6.13), which can be attributed to the fact that the

original struts' layup already meets some of the design "rules of thumb" considered in the optimization from Chapter 5 [57]. The original layup already had ±45 outer plies and at least 10% of the plies were oriented to each of the principal layup orientations, which gives strength to the structure [4, 57].

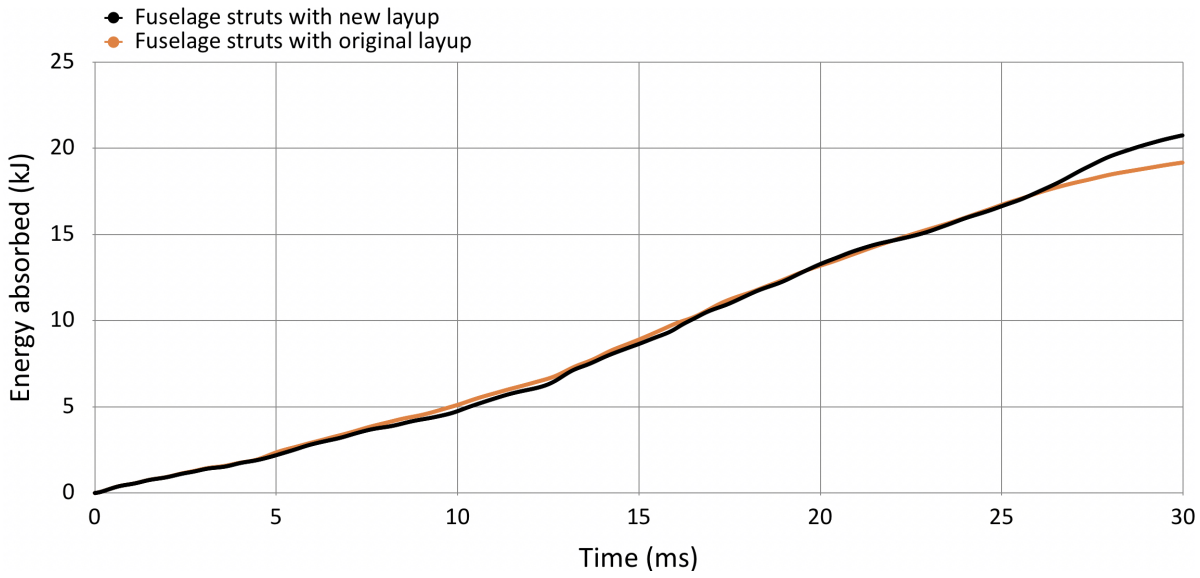

Figure 6.13: Energy absorbed by the fuselage with both square strut layups and modified dimensions to keep the same mass in both designs.

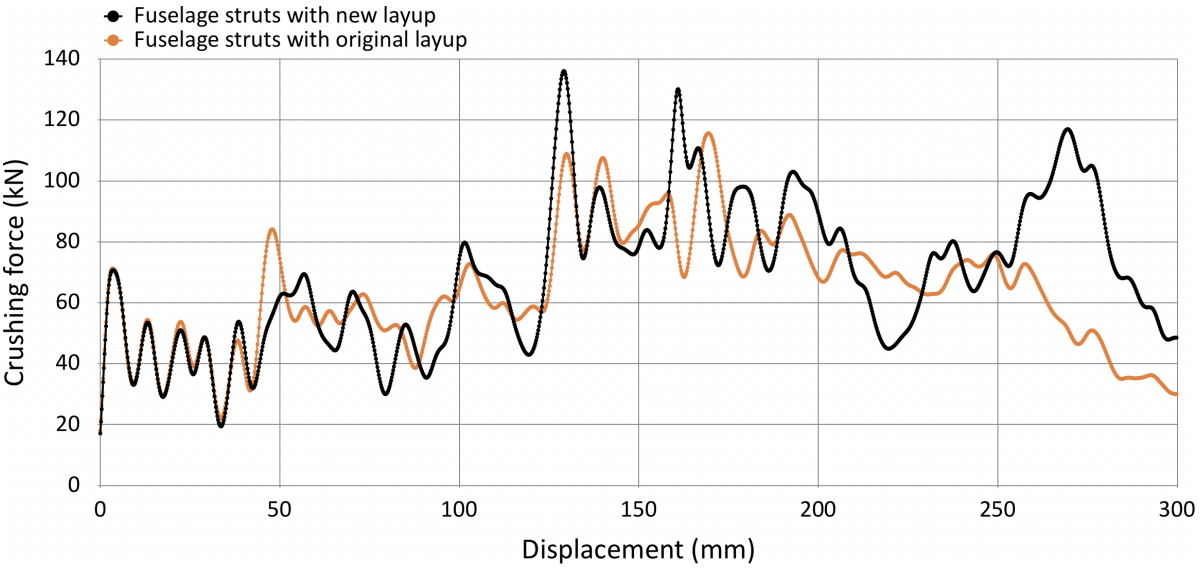

Figure 6.14: Force-displacement graph from the fuselage with both square strut layups and modified dimensions to keep the same mass in both designs.

The new layup presents in Figure 6.14 a reduction of the first peak of force, delaying the higher loads reaching the cabin during the crash. This is desirable for crashworthiness purposes, in addition to the mentioned longer peaks, as explained in Chapter 2. Therefore, it can be concluded that the new layup is kept for the next chapter's fuselage model analyses.

6.5 Computation time

As mentioned at the beginning of this chapter, most of the simulations of this chapter and the next one are run using the cluster *hpc12* from the faculty. This accelerates the amount of time spent on these to run

simultaneously in it, taking a bit less than a day to run each simulation. The time spent in each simulation from this chapter is of 15 to 17 hours, depending on how many simulations are running in parallel. In this chapter, the 15 hours of computation correspond to a single simulation running on the cluster, and 17 when running 3-4 simulations at the same time. The only exception to this is the original STUNNING fuselage with C-struts when this one is run in LS-DYNA R7.0.1, reproducing Poorte's results [4]. This version of the program, as mentioned, is only available on the PC assigned by the faculty. Hence, when running locally, the simulation takes longer to compute: about 24 hours for a single analysis.

Chapter 7

Parametric study of fuselage struts

This chapter aims to find the best strut geometry to improve further the crashworthiness metrics resulting from the last analyses in Chapter 6. The cross-section geometry of the struts, as well as their length and layup, must be kept. The last one being $[\pm 45, 0, \mp 75, \pm 15, 90]_s$. However, their cross-sectional dimensions are modified to perform this parametric study. The new-sized struts are introduced in different fuselage models, and the dimensions range goes from 20 to 70 mm, with a 5 mm span in between and two exceptions. The first exception is the 28.8 mm per side used at the end of the previous chapter. This one is used as a reference to keep in mind the fuselage's behavior and mass before the parametric study. And the second exception is the 36.8 mm side dimension, which was Poorte's square strut dimensions on the STUNNING fuselage model [4]. Before their stacking sequence modification. Struts smaller than 20 mm per side are not considered as they can collapse differently due to their parallel walls being closer to each other. That risks the struts absorbing less energy, or simply crushing abruptly and leading to higher peaks of force. Both consequences are not wanted. Struts larger than 70 mm per side would add too much weight to the fuselage to the original STUNNING fuselage, which is unwanted in aeronautics. In such cases, the improvement of crashworthiness, as high as it could be, would not be worth the extra weight. From the range in between, each dimension is evaluated to provide the best fuselage crash response possible.

7.1 Results from the parametric study

This section presents the results obtained from the different fuselage analyses. There are a total of twelve numerical analyses in this parametric study, as mentioned. From these, the strut mass difference in each analysis is compared to the analysis of reference from the end of Chapter 6. Afterward, the crashworthiness metrics of the fuselage are evaluated for the different strut designs. That helps make an informed decision on what the final strut size should be.

7.1.1 Mass changes in the fuselage model

In this sub-section, the twelve strut sizes inserted in the fuselage analyses are listed in Table 7.1 to present the mass per strut, and the consequent fuselage section mass. This table shows how the change of the strut dimensions affects the fuselage's total mass since a big increase in its mass is not desired.

Figure 7.1 presents the differences in mass from Table 7.1, both for a single strut case and the fuselage model. The graph shows a linear trend in both cases, and the differences in mass are calculated in grams with respect to the 28.8 mm side strut analysis. This analysis presents the original masses per strut (179.45 g) and for the entire STUNNING fuselage sub-floor model from Chapter 6 (27.57 kg). In Figure 7.1, the goal is to show how much more significant the fuselage's change of mass is than the change in a single strut mass. This is due to the fuselage section's mass considering four struts instead of one, and it affects the aircraft's performance.

As shown in Figure 7.1, smaller-sized struts save mass to the fuselage or add a little amount to the model. Hence, these are preferred in aeronautics for operational purposes. Despite this, slightly larger struts may be worth the increase in weight if their crashworthiness properties are significantly improved. Therefore, these metrics of the fuselage models with struts smaller than 60 mm per side are studied in the next section. This

cut is made since struts bigger than that add more than 1 kg of mass to the fuselage section. That amount is considered too large, so any crashworthiness improvement is not worth the penalty in mass.

Strut side dimension (mm)	Single strut mass (g)	Total mass (kg)
20	120.66	27.33
25	155.86	27.47
28.8	182.61	27.58
30	191.06	27.62
36.8	239.30	27.81
40	261.46	27.90
45	296.66	28.04
50	331.86	28.18
55	367.08	28.32
60	402.27	28.46
65	437.48	28.60
70	472.68	28.74

Table 7.1: Mass for a single strut and the total fuselage section in each numerical model.

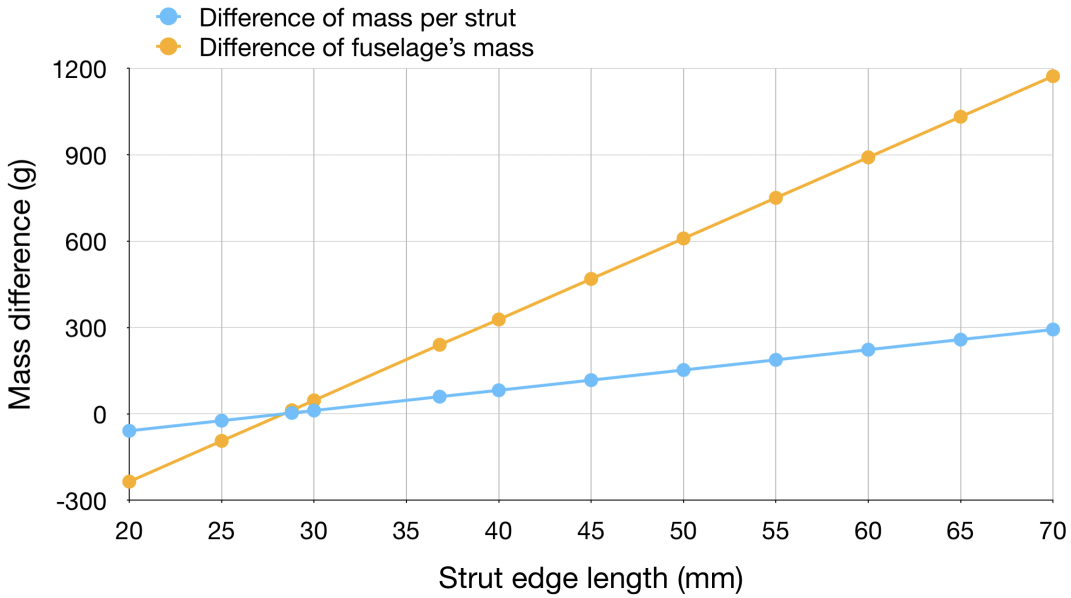

Figure 7.1: Change of mass for a single strut and total mass of the fuselage section of study.

7.1.2 Crashworthiness analysis

This section presents the crashworthiness metric responses to see which strut sizes benefit the fuselage section the most, from 20 mm to 60 mm, as concluded in the previous section. Figure 7.2 and Figure 7.3 show the energy absorption and force-displacement graphs for the different fuselage models. All graphs from this chapter presenting crashworthiness metrics are filtered using a SAE filter with a cut-off frequency of 600 Hz. The filtering brings consistency to the graphs and matches the analyses from Chapter 6 and Poorte's work of reference [4]. At first, Figure 7.2 shows the energy absorbed by all fuselage models within the strut side range. The models of interest are those that present a higher energy absorption capability than the 28.8 mm strut model (drawn in black). The strut dimensions that cause the fuselage to meet this requirement are the ones with 55 mm, 50 mm, 20 mm and 40 mm per side. These four models, including the reference curve in black, are therefore plotted in Figure 7.3 for further analysis.

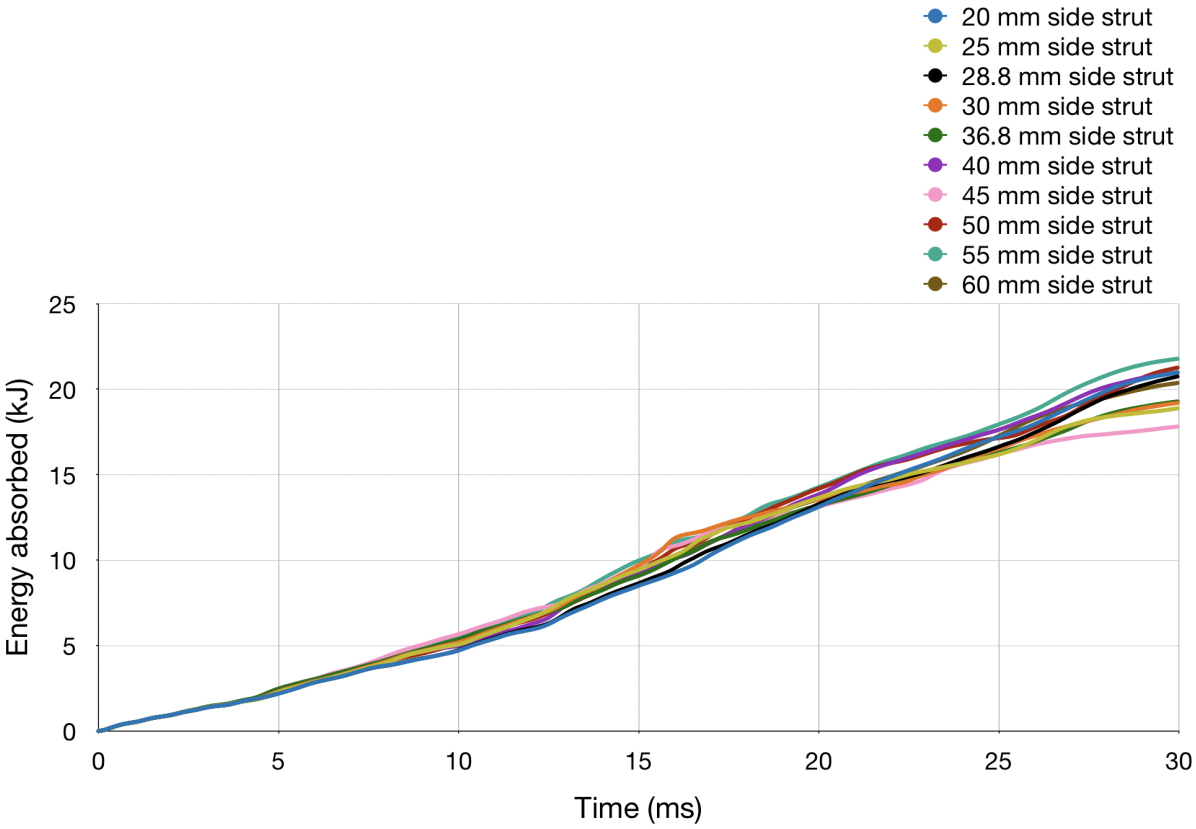

Figure 7.2: Energy absorbed by the fuselage in each simulation, considering ten different strut side dimensions.

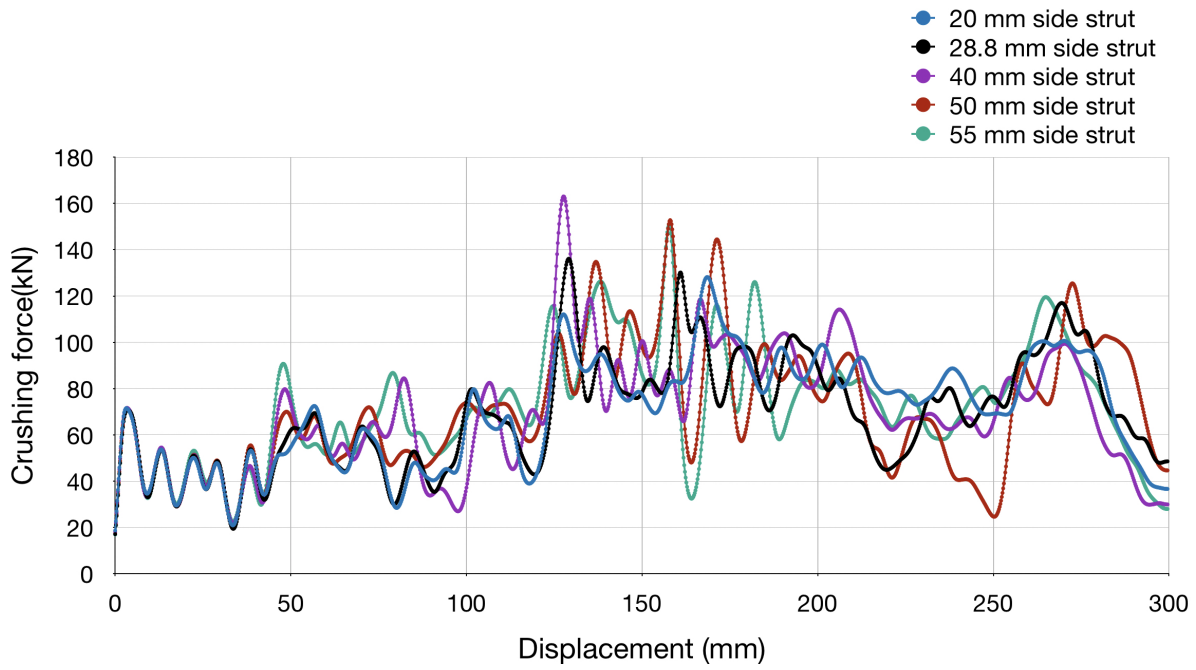

Figure 7.3: Force-displacement graph for fuselage models with strut edge lengths of 55 mm, 50 mm, 20 mm and 40 mm. The reference model with edge length of 28.8 mm is included.

Figure 7.2 presents generally little difference between the fuselages with each strut configuration. This is expected, since the struts are one of the components of the airframe that contribute less to the fuselage's crashworthiness, according to what has been stated in Chapter 2. However, any slight change is considered

an improvement, and the strut designs affecting the force-displacement graph from Figure 7.3 are of importance for their distinction.

The most absorbing fuselage model has a 55 mm strut side and presents a higher first peak force than the 28.8 mm model of reference. However, the remaining peaks of the graph are of the same magnitude. Apart from only improving the energy absorption metric, this strut size adds a big amount of mass to the fuselage model (see Figure 7.1). Hence, the fuselage model with 55 mm side struts is not considered adequate for crashworthiness applications on aircraft. The second most energy-absorbing design is the fuselage model with a 50 mm strut side. This model presents higher peaks of force with respect to the reference model along with the entire force-displacement graph in Figure 7.3. Additionally, the mass increased in the model (see Figure 7.1) makes this strut design also inadequate for the aircraft. The two remaining eligible designs are those with 20 mm and 40 mm strut sides. From these, the only fuselage model that presents lower (and longer) peaks of force than the model of reference is the 20 mm strut side model. Moreover, this one also absorbs more energy in Figure 7.2 than the 40 mm strut design, while saving mass in the fuselage section. If the model with a 40 mm strut side showed better crashworthiness metrics in Figures 7.2 and 7.3, the addition of mass would have been acceptable in this case, according to Figure 7.1. Since this is not the case, the fuselage model with a strut side of 20 mm is chosen as the final fuselage strut configuration.

7.2 Final fuselage design

The final fuselage design resulting from this and the previous chapter has square struts of 20 mm per side, round fillets of 6.4 mm radius, and $[\pm 45, 0, \mp 75, \pm 15, 90]_s$ per layup. This configuration has improved the crashworthiness metrics presented in the original C-strut STUNNING fuselage model. Hence, the goal of the thesis has been met and the fuselage's section mass has been reduced, which is beneficial for the thermoplastic aircraft design. The last step of this thesis is to represent the crushing of this final fuselage model more realistically. Up until now, the fuselage analyses have been crushing with no payload mass on top, as shown in Figure 7.4. This causes a large intrusion of the fuselage's bottom skin, which moves upwards upon crushing and pushes the cargo crossbeams in the same direction. This phenomenon can compromise the cabin floor eventually and infringe the crashworthiness standards for composite aircraft established in Chapter 2 [18, 21, 28]. Therefore, a payload mass is introduced on top of the fuselage section to see whether or not the crushing is better represented in the structure.

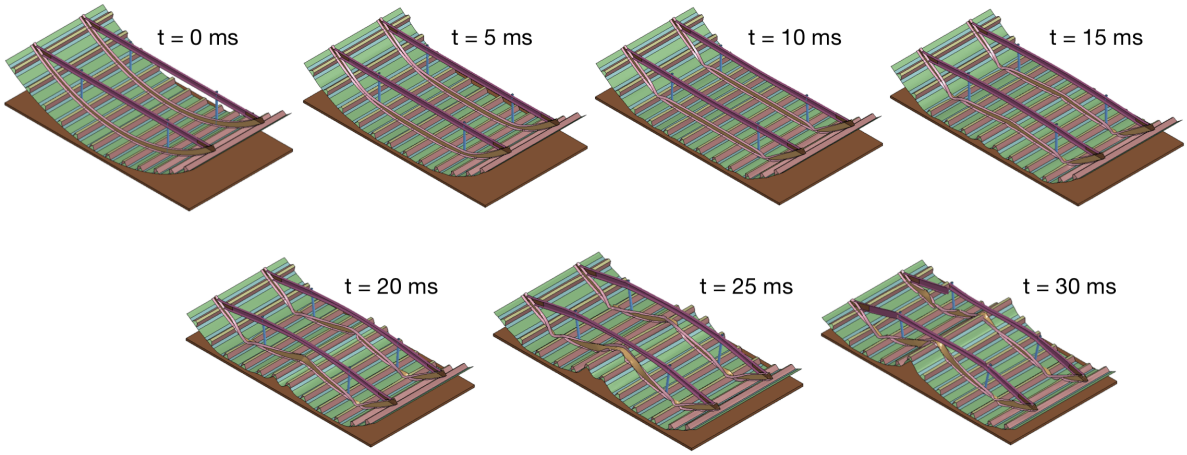

Figure 7.4: Crushing sequence for the final strut's design with 20 mm of edge length and without a payload mass on top.

7.2.1 Fuselage crushing sequence including payload

In a commercial aircraft, the payload mass from the cabin and cargo areas (luggage and passengers) and the mass of the upper half structure can change the way a fuselage crushes [4, 35]. Adding this payload mass from cargo, passengers, and the fuselage's upper structure reduces the intrusion of the bottom skin upwards from Figure 7.4. To simulate these conditions, a dark pink mass plate of 120 kg is added on top of

the fuselage section as shown in Figure 7.5. The plate is in contact with the cargo crossbeams' top and has arbitrary dimensions to cover at least the struts of the fuselage section, plus 10 mm per side to notice the effect of the payload on these. The additional mass is assumed from Poorte's thesis, representing the cargo mass corresponding to the six passengers that would fit in the fuselage section [4]. The payload mass shows how in Figure 7.6, the fuselage fosters progressive strut crushing, which is wanted for survivable crash applications (see Chapter 2).

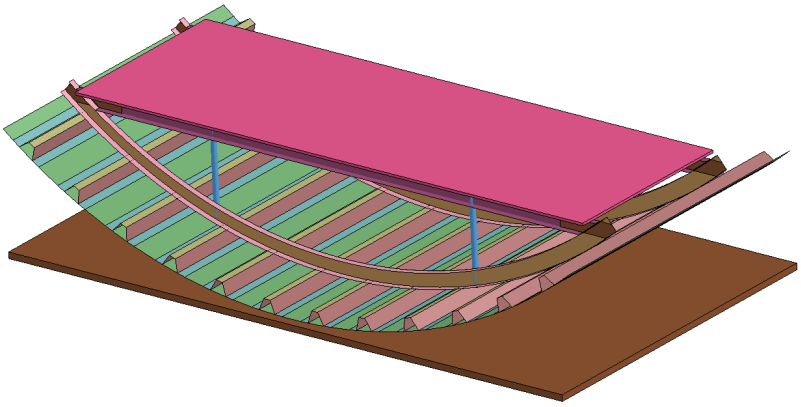

Figure 7.5: Payload mass added to the final fuselage design. The mass is modeled as a dark pink rigid plate.

The payload mass from Figure 7.5 represents only the passengers' masses as a whole rigid plate, which is loaded uniformly. The reason why only the luggage's weight is considered is that the upper part of the fuselage structure is out of the scope of this thesis, and therefore, not included. In addition to this, the passengers' mass would act upon the cabin floor of the fuselage, which is not included in this fuselage section either. Hence, to add the passengers' mass, the structure from the sub-floor to the cabin would have to be included in the section model, altogether with the upper frame of the fuselage.

With the newly added payload mass, the crushing kinematics of the fuselage change as shown in Figure 7.6, and leads to a variation in its crashworthiness metrics. These are then compared to the final fuselage model with no payload mass on top.

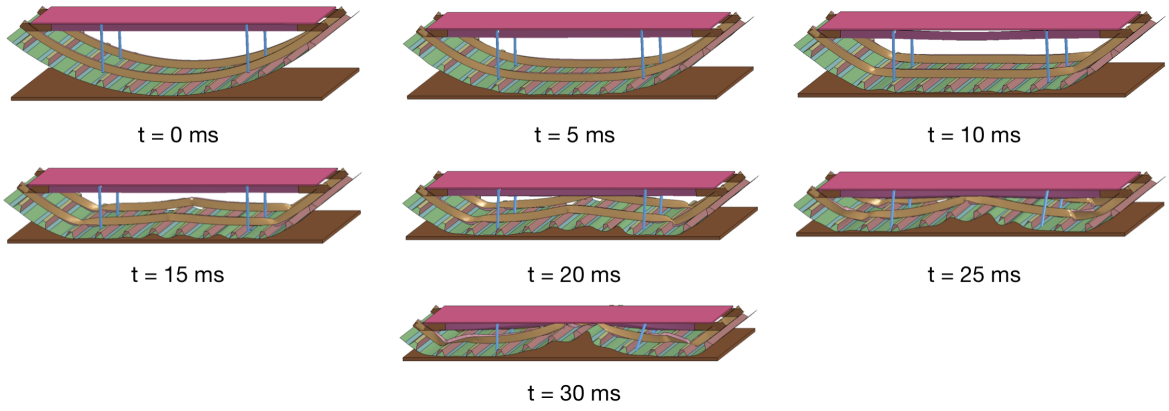

Figure 7.6: Crushing sequence of the final fuselage design with the payload mass on top.

7.2.2 Comparison of results with and without simplified mass

To study the effect of including a payload mass in the fuselage, the energy absorption and force-displacement graphs for both designs are presented in Figure 7.7 and Figure 7.8. These graphs compare the two models of the final fuselage design, with and without considering the additional payload mass.

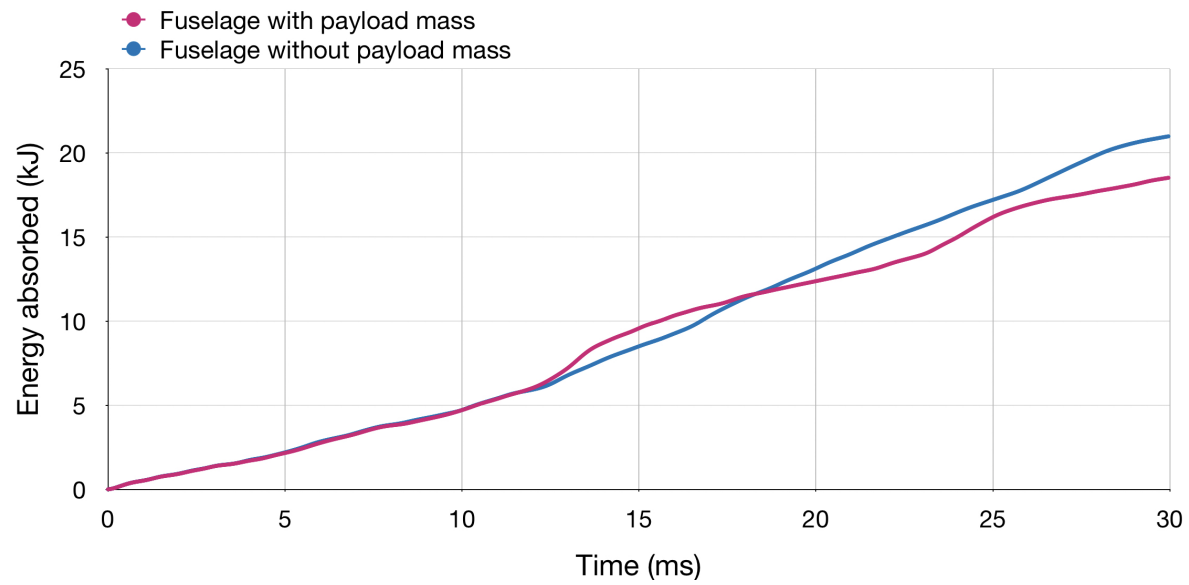

Figure 7.7: Energy absorption graph from the fuselage final design, with and without the implemented payload mass.

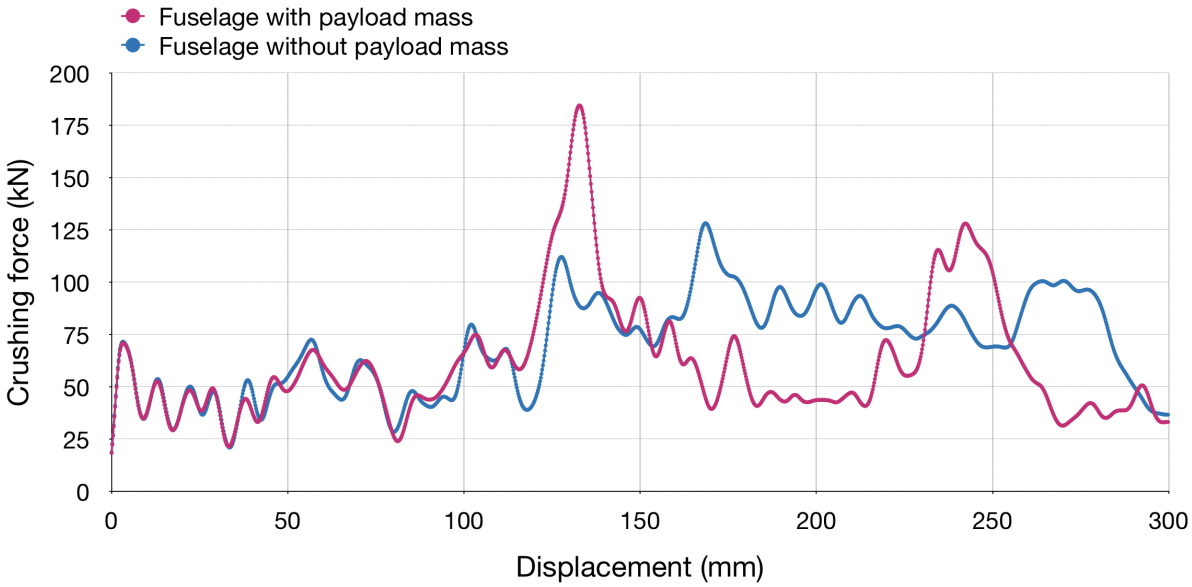

Figure 7.8: Force-displacement graph from the fuselage final design, with and without the implemented payload mass.

As expected, the model with the payload mass presents the crash kinematics from Figure 7.6 and reduces the intrusion from the skin moving upwards. In the crushing sequence from this model, the frame and cargo crossbeam do not tear apart as they did in Figure 7.4 when they had no restrictions of movement upwards. Nonetheless, these still get damaged, as the payload mass limits their room for movement, which makes the first crushing contact with the impactor plate very abrupt. This generates a very large increase in the first peak of force, which is delayed and longer than in previous fuselage scenarios. The placement of the payload plate being in direct contact with the cargo crossbeams' top, can cause initial penetration in the nodes at the start of the simulation [4]. Consequently, this penetration generates an increase in the first peak as well.

The struts crash when adding the payload mass, as it is intended for crashworthiness purposes. This translates into a higher second long peak force in Figure 7.8 resulting from their crash initiation onto the plate. Between the first and second increased crushing peak loads, the relaxation presented in the blue force-displacement curve causes the fuselage with payload to not absorb as much energy as the previous design (see Figure 7.7). Hence, the ideal conditions (no payload) simulated on the fuselage for the past two chapters

overestimate the amount of energy that the fuselage absorbs, which misleads the real fuselage crushing behavior by not being representative enough.

Additional features should be included in the fuselage model that considers the payload mass to further improve its crashworthiness metrics. By doing so, not only the energy absorption would be increased, but the peak forces experienced in it would be reduced. These additional features could include the implementation of bevels at the bottom of the struts to trigger the crushing initiation, just as Chapter 4 and Chapter 5 did with the tube models [10]. However, adding mass to the fuselage would not be in its best interest for flight performance, so instead, a study of the strut's positioning could be done to take advantage of the current fuselage structure and use the corners of the stringers as triggers for the struts' crushing [4]. By doing so, the struts could start crushing earlier, and reduce the peak force when they get in contact with the impactor. The mentioned alternatives are worth an entire research topic since there are several ways to improve these crushing conditions, such as oblique strut positioning, or an indentation at the struts' bottom to generate a more progressive crushing. Moreover, the changes and optimization can also be done to other parts of the fuselage sub-floor. Ideally, the optimization can be done to such components as the frame or the cargo crossbeams of the fuselage section. These contribute more to the crashworthiness behavior of the fuselage and their crashworthiness metrics optimization might have a larger impact on the structure's performance. When doing so, however, the fuselage should be as representative as possible to aim for a more determining and conclusive work. For better representation, the initial step is to distance a bit the payload plate from the cargo crossbeams of the sub-floor model. That way it can be confirmed whether or not the initial penetration of the nodes contributed to the first peak of force. For further representation, the upper airframe and passengers' mass on the cabin floor should be included afterward to reevaluate the crashworthiness performance of the fuselage more accurately.

7.3 Computation time

The previously defined fuselage models are all performed using LS-DYNA R9.3.1 in the faculty's cluster. Most of them are run simultaneously in two sets of 6 simulations at a time to occupy less space from the cluster's disk. This causes the simulations to take between 17 to 20 hours, which is less than what could take running individually on a local PC. The fuselage model with the luggage additional payload for six passengers is run alone and takes slightly less time to compute (15 hours approximately), as it happened occasionally with the fuselage analyses from Chapter 6.

Chapter 8

Conclusions and recommendations

This master thesis topic contributes to the Clean Sky STUNNING project in the design optimization of the thermoplastic struts from the Next Generation Multifunctional Fuselage demonstrator, which requires using new software and learning new methodologies. These include the finite element modeling of composites in LS-DYNA, which works using keywords to set up numerical simulations. The keywords are not as graphically intuitive as an Abaqus setup, which was the program used for this type of analysis during the master courses. Hence, there were setbacks when adjusting to LS-DYNA's analyses' setup. Something similar happened with the optimization setup on LS-OPT. This one was chosen to integrate both numerical crushing analyses and optimization in one software. The current state-of-the-art of structural tools is expanding, and software like LS-OPT or LS-TaSC allow the optimization of LS-DYNA numerical analyses' parameters, even topological, that enable a better and faster optimization through this integration. Therefore, the new software added a certain efficiency and reliability to this thesis results, disregarding the amount of time invested in using these. With the aid of LS-DYNA and LS-OPT manuals, the numerical analyses and optimizations from the previous chapters have been successfully performed. These chapters are structured so that each one presents a consecutive stage of this thesis research, increasing the complexity of the numerical models as their computational time increases as well.

First, Chapter 2 introduces the state-of-the-art of the term crashworthiness, its aeronautics and composite applications and what to look for in these structures to meet the crash requirements, how these are modeled in LS-DYNA's numerical software; and what changes can be done to the structure to get a better crashworthy behavior. This chapter introduces and justifies the methodology of the following chapters, as well as the multiple objectives and constraints for the optimization procedures in Chapter 5. Crashworthiness in structures is defined as their capability to dissipate or absorb the energy of the crash through deformation or damage while protecting the occupants inside the structure. In this thesis, the crashworthiness of the STUNNING fuselage section is studied. There are several crashworthiness metrics to evaluate the structure's performance under crash requirements, and from the most relevant ones, EA (or SEA) and F_{peak} are used to evaluate the numerical models of the following chapters. In the aeronautics sector, Chapter 2 states the struts to not be as contributing to the crashworthiness of a fuselage as the frame or cargo floor. However, these modify the second peak of force, bounding the accelerations that reach the cabin during a crash to protect the passengers from severe injuries or even death.

Chapter 3 presents the first analyses modeled in LS-DYNA to get familiar with it and understand how to model finite element analyses using the software keywords. Due to the learning curve that comes with this software, this chapter's analyses, alongside the analyses from Chapter 4 and the LS-OPT optimization of Chapter 5, were the longest stages of the thesis to be completed. Chapter 3 presents the aluminum and composite plates with an applied tension load on one end, and a fixed boundary condition on the opposite one. From these, the element formulation and composite material modeling using *MAT_058_LAMINATED_COMPOSITE_FABRIC* are applied in the following chapter. Chapter 4 changes the 2D scenario from a plate to a three-dimensional tube that is crushed with a rigid plate. This analysis setup and results are performed and checked with literature for validation purposes. The post-processing is what took the longest in this tube analysis because it required learning where to get the correct data to calculate the crashworthiness metrics and evaluate the model. The post-processing provided the metrics of EA, F_{peak} and F_{mean} for the tube's crushing,

which were 3201.36 J, 116.67 kN and 29.97 kN, respectively. These values are the result of the tube's original layup $[0_2, \pm 45_2, 90_2]_s$, and act as a reference for the following chapter's optimization. Chapter 5 tries to find the optimal tube's layup by applying design rules for this one for crashworthiness purposes, such as adding ±45 plies on the outside, and ensuring that the directions 0 and 90° are also present in it. After that, the variables to optimize in LS-OPT are two active plies and their dependent ones, which have the same orientation but opposite signs. LS-OPT aimed to find a good trade-off between the three optimization objectives mentioned (energy absorbed, peak, and mean forces) and improve these values from the results from Chapter 4. While doing so, the number of plies is unchanged from the original layup to maintain the tube's mass while improving its crashworthy capabilities. Chapter 5 took quite some time, not because LS-OPT is a hard software to use, but because there was extensive research through LS-OPT's manual to decide on the most adequate metamodel optimization setup. That included considering the program's limitations, which has some metamodels under construction, such as Kriging. The final optimization uses the feed-forward neural network metamodel since it is proven to be the most suitable one amongst the available ones for the tube's non-linear analysis. This metamodel is also proved to predict better solutions than the radial-based function neural network, which has a linear nature that does not work in this non-linear crushing case. The resulting layup $[\pm 45, 0, \mp 75, \pm 15, 90]_s$ predicts this tube's new design to further improve beyond 8.41% the tube's crashworthiness metrics from Chapter 4: 3477.24 J for EA, 112.89 kN for F_{peak} and a 32.88 kN F_{mean} value. Their prediction relative errors found in the optimization process are 3.83%, 0.24%, and 3.55%, respectively. This resulting layup design is chosen based on a pre-selection process, choosing the designs that predict an improvement in the three design objectives: higher energy absorption and mean force values, and a lower peak force. After doing so, the generation of a Pareto front is done to show the EA and F_{peak} objectives' trade-off, as well as the F_{peak} versus F_{mean}. The resulting design is chosen based on how much it maximizes both objectives, being above or below the Pareto front accordingly in each graph.

Once the tube is optimized, the idea to implement this one into the STUNNING fuselage is made based on Poorte's thesis conclusions. This one states that the squared struts are better energy absorbers than the C-struts and provide a better crashworthy behavior with the bottom free ends as contact condition. Additionally, the LS-DYNA analyses of the fuselage section using the updated version R9.3.1 are proven to provide similar results as Poorte's, which makes his conclusion valid for this thesis as well. Therefore, the introduction of the tube's optimum layup from Chapter 5 is done to aid the square struts absorb a slightly higher amount of energy during the crash. While doing so, the struts' new layup has more plies than the previous one, so the dimensions of the struts are reduced from 36.8 mm to 28.8 mm per side to keep the same fuselage's mass. In the end, the change in layup provides a slight improvement on the fuselage crashworthiness behavior, which is why in Chapter 7, the same layup is used on struts to find their best dimensions when using a square cross-section. The purpose of this last chapter is similar to Chapter 5: increase the energy absorbed by the structure, reduce the force peaks in the fuselage's force-displacement graph, and improve the crushing sequence of the fuselage as much as possible. By altering the mass of the struts, Chapter 7 alters the mass per strut and consequently, the fuselage's. The first intention in Chapter 7 was to parametrize the geometry of the struts and send the model to LS-OPT for a simple topology optimization run. This was not possible because, during the sampling, when the struts' size is modified, their mesh changes, and the nodes rearrange. This causes LS-OPT to take values from a node that has changed its location, providing a misleading outcome. This can be further explained with an example. For a given node ID that exists in the original struts of the STUNNING fuselage model, when the struts' size is reduced, this node may not exist anymore due to the struts' rearranged mesh, which numbers the nodes differently. In that case, LS-OPT sees that the node indicated does not exist and stops the optimization with an error message, since it cannot retrieve sampled data from it. Therefore, strut sizes are introduced in the numerical analyses of the fuselage instead. By doing so, the crashworthiness of each fuselage is evaluated and compared amongst strut configurations. To make an informed decision on which strut size provides a better outcome, the more strut dimensions studied, the better. In this case, there are at first a total of twelve fuselage analyses with different strut dimensions, which go from 20 to 70 mm and narrow down as mass and crashworthiness metrics are evaluated. The last two strut dimensions considered are disregarded by the amount of mass they add to the fuselage (beyond 1 kg). After that, when comparing the crashworthiness abilities provided by the different fuselage models with their respective strut configurations, it is concluded that the fuselage with strut dimension of 20 mm per side improves the crashworthiness metrics of energy absorption and peak force. The crushing sequence is improved as well in this case while leading to a reduction in the fuselage's mass, which aids the aircraft's flight performance. Hence, this is chosen as the final fuselage model. This outcome is a good solution for this thesis, but the mentioned limitations

in the methodology must be taken into account in future work since there is a chance that a better strut design configuration exists. Additionally, future work needs a better representation of the fuselage section by considering the remaining part of the airframe at its top and the full payload mass including the passengers on the cabin floor. At the end of Chapter 7, it is seen that when adding a payload mass to simulate the passengers' luggage, the fuselage crash kinematics changes and provides a lower amount of energy absorption by the end of the crash and increased peaks of force in Figure 7.7 and Figure 7.8. While the initial peaking can be reduced by placing the payload mass plate at a small distance from the fuselage model to avoid the nodes' initial penetration, the outcoming metrics should be further improved. This can be done by changing the layup and cross-sectional geometry of the struts or any other part of the fuselage sub-section that contributes more to its crashworthiness. Some of these parts can be the frame or the cargo floor, which are the main contributors to the energy absorption of a fuselage section, as explained in Chapter 2. Another alternative to this can include the study of the struts' position and location change, to see if this induces lower peak forces for the fuselage upon crushing. Another option is to add a cut that works as a bevel to the struts and triggers them to crash earlier. Further research should be conducted on these crushing triggers while considering a more complete representation of the fuselage crash conditions, including the passengers and upper airframe to verify how the combination of these regulates the studied crashworthiness metrics.

In conclusion, each chapter of this thesis uses previous work and improves the existing structure in terms of crashworthiness. Sometimes each chapter even implements the features of an already studied structure into a more complex model, which causes this last one to take longer to compute. The plates' tests eased into the composite modeling of the crushing tube simulation, and then this tube was optimized and able to be implemented in the STUNNING fuselage. However, the limitations on the fuselage strut dimensions' introduction to LS-OPT have eluded the topology optimization in Chapter 7, leading to a parametric study instead. This implies that future studies should use more suitable software for the geometrical optimization of the struts. Software like LS-TaSC, if available, can be done to do so, which might consider more cross-section geometries and dimensions than what has been done manually in this thesis so far. Hence, this kind of software can be efficient in terms of computation, but also provide reliable optimum solutions. For a better representation of the fuselage, more components can be topologically optimized to provide even better crashworthiness metrics. Despite this, after the topology optimization of a fuselage component, its layup should be analyzed to verify if this one is the one that provides the best crashworthiness to the whole model when new geometries are implemented. This can be done using first LS-TaSC for topology optimization and LS-OPT for the stacking sequence optimization, as done in this thesis. Or by conducting shape and stacking sequence optimizations at once in LS-TaSC, if possible.

With the previous recommendations, future research can lead to a fuselage optimal strut design regardless of the approach one may take: single output for the optimization process, or using a Pareto front to consider objective trade-offs like in this thesis. Regardless of the approach, the final fuselage design can be evaluated and eventually, manufactured. At that point, the fuselage design would prove to be the best for its survivable crash requirements, due to the reliable procedure behind its outcome.

Bibliography

[1] I. Savage. "Comparing the fatality risks in United States transportation across modes and over time". In: *Research in Transportation Economics* 43 (1 2013). p.9-22. ISSN: 07398859. DOI: 10.1016/j.retrec.2012.12.011.

[2] EASA. *Certification Specifications and Acceptable Means of Compliance for Large Aeroplanes*. Tech. rep. Amendment 21. 2018.

[3] *Airframe | Clean Sky*. English. https://www.cleansky.eu/airframe.

[4] V.K. Poorte. *Design of a crash energy absorber for a composite aircraft fuselage using a combined analytical-numerical approach*. Apr. 2021. URL: repository.tudelft.nl/islandora/object/uuid:937cb0b2-3f81-42f2-a3c3-d0ffe3370760?collection=education.

[5] S.L. Veldman, P. Kortbeek, P.C. Wölcken, R. Herrmann, J. Kos, and I. Fernandez Villegas. "Development of a multifunctional fuselage demonstrator". In: Published on-line at TU Delft repository, p.1-8. 2020.

[6] R. Vignjevic and M. Meo. "Simulation of helicopter under-floor structure impact on water". In: *International Journal of Crashworthiness* 6 (3 2001). p.425-443. ISSN: 17542111. DOI: 10.1533/cras.2001.0188.

[7] S. Boria, G. Belingardi, D. Fiumarella, and A. Scattina. "Experimental crushing analysis of thermoplastic and hybrid composites". In: *Composite Structures* 226 (2019). Published on-line, p.1-11. ISSN: 02638223. DOI: 10.1016/j.compstruct.2019.111241.

[8] LSTC. *LS-DYNA R9.0®KEYWORD USER'S MANUAL VOLUME I*. Tech. rep. 2016. URL: www.lstc.com.

[9] LSTC. *LS-DYNA R9.0 ® KEYWORD USER'S MANUAL VOLUME II*. Tech. rep. 2016. URL: www.lstc.com.

[10] A. Cherniaev, C. Butcher, and J. Montesano. "Predicting the axial crush response of CFRP tubes using three damage-based constitutive models". In: *Thin-Walled Structures* 129 (2018). p.349-364. ISSN: 02638231. DOI: 10.1016/j.tws.2018.05.003.

[11] A. Li. *Optimization of Composite Structures for Crashworthiness*. Tech. rep. 2019. URL: http://repository.tudelft.nl/.

[12] C.W. Isaac and C. Ezekwem. "A review of the crashworthiness performance of energy absorbing composite structure within the context of materials, manufacturing and maintenance for sustainability". In: *Composite Structures* (2020). Published on-line, p.1-32. ISSN: 02638223. DOI: 10.1016/j.compstruct.2020.113081.

[13] T.J. Reddy, Y.V.D. Rao, and V. Narayanamurthy. "Thin-walled structural configurations for enhanced crashworthiness". In: *International Journal of Crashworthiness* 23 (1 2018). p.57-73. ISSN: 17542111. DOI: 10.1080/13588265.2017.1306824.

[14] A. Elmarakbi. *Advanced Composite Materials for Automotive Applications : Structural Integrity and Crashworthiness*. Hoboken: Wiley, 2013.

[15] W. Guan, Y. Yu, and G. Gao. "Crashworthiness performance and multiobjective optimization of a combined splitting circular tube energy absorber under eccentric impact for subway vehicles". In: *International Journal of Impact Engineering* 158 (2021). Published on-line, p.1-17. ISSN: 0734743X. DOI: 10.1016/j.ijimpeng.2021.104006.

[16] Y. Zhang, P. Ge, M. Lu, and X. Lai. "Crashworthiness study for multi-cell composite filling structures". In: *International Journal of Crashworthiness* 23 (1 2018). p.32-46. ISSN: 17542111. DOI: 10.1080/13588265.2017.1304169.

[17] L. Di Palma, F. Di Caprio, A. Chiariello, M. Ignarra, S. Russo, A. Riccio, A. De Luca, and F. Caputo. “Vertical drop test of composite fuselage section of a regional aircraft”. In: *AIAA Journal* 58 (1 2020). p.474-487. ISSN: 00011452. DOI: 10.2514/1.J058517.

[18] Transport Aircraft Crashworthiness and Ditching Working Group. *Transport Aircraft Crashworthiness and Ditching Working Group: Report to FAA*. Tech. rep.

[19] P. Xue, M.L. Ding, C.F. Qiao, and T.X. Yu. “Crashworthiness study of a civil aircraft fuselage section”. In: *Latin American Journal of Solids and Structures* 11 (9 2014). Published on-line, p.1-13. ISSN: 16797825. DOI: 10.1590/S1679-78252014000900007.

[20] J. Paz Mendez, J. Díaz Garcia, L.E. Romera Rodriguez, and F. Teixeira-Dias. “Crashworthiness study on hybrid energy absorbers as vertical struts in civil aircraft fuselage designs”. In: *International Journal of Crashworthiness* 25 (4 2020). p.430-446. ISSN: 17542111. DOI: 10.1080/13588265.2019.1605723.

[21] J.E. Duven. “Rules and Regulations Authority: 49 U.S.C. 106(g), 40113, 44701, 44702, 44704”. In: *Federal Register* (143).

[22] K.E. Jackson. “Impact testing and simulation of a crashworthy composite fuselage concept”. In: *International Journal of Crashworthiness* 6 (1 2001). p.107-122. ISSN: 17542111. DOI: 10.1533/cras.2001.0166.

[23] A. Riccio, S. Saputo, A. Sellitto, and F. Di Caprio. “On the crashworthiness behaviour of a composite fuselage Sub-floor component”. In: *Composite Structures* 234 (2020). Published on-line, p.1-14. ISSN: 02638223. DOI: 10.1016/j.compstruct.2019.111662.

[24] A. Riccio, A. Raimondo, F. Di Caprio, M. Fusco, and P. Sanità. “Experimental and numerical investigation on the crashworthiness of a composite fuselage sub-floor support system”. In: *Composites Part B: Engineering* 150 (2018). p.93-103. ISSN: 13598368. DOI: 10.1016/j.compositesb.2018.05.044.

[25] C.M. Kindervater, D. Kohlgruber, and A. Johnson. “Composite vehicle structural crashworthiness – A status of design methodology and numerical simulation techniques”. In: *International Journal of Crashworthiness* 4 (2 1999). p.213-230. ISSN: 17542111. DOI: 10.1533/cras.1999.0101.

[26] P. Schatrow and M. Waimer. “Investigation of a crash concept for CFRP transport aircraft based on tension absorption”. In: *International Journal of Crashworthiness* 19 (5 2014). p.524-539. ISSN: 17542111. DOI: 10.1080/13588265.2014.917498.

[27] A.G. Mamalis, M. Robinson, D.E. Manolakos, G.A. Demosthenous, M.B. Ioannidis, and J. Carruthers. “Crashworthy capability of composite material structures”. In: *Composite Structures* 37 (2 1997). p.109-134. ISSN: 02638223. DOI: 10.1016/S0263-8223(97)80005-0.

[28] US Department of Transportation and Federal Aviation Administration. *Advisory Circular - Change 1 to Composite Aircraft Structure*. Tech. rep.

[29] EASA. *Proposed Special Condition on "Crash Survivability for CFRP Fuselage". Applicable to Airbus A350-941 (SC C-01)*. Tech. rep.

[30] D.B. Schwinn. “Parametrised fuselage modelling to evaluate aircraft crash behaviour in early design stages”. In: *International Journal of Crashworthiness* 20 (5 2015). p.413-430. ISSN: 17542111. DOI: 10.1080/13588265.2015.1022435.

[31] D.H. Kim, H.G. Kim, and H.S. Kim. “Design optimization and manufacture of hybrid glass/carbon fiber reinforced composite bumper beam for automobile vehicle”. In: *Composite Structures* 131 (2015). p.742-752. ISSN: 02638223. DOI: 10.1016/j.compstruct.2015.06.028.

[32] S. Boria and G. Belingardi. “Numerical investigation of energy absorbers in composite materials for automotive applications”. In: *International Journal of Crashworthiness* 17 (4 2012). p.345-356. ISSN: 13588265. DOI: 10.1080/13588265.2011.648516.

[33] F. X. Meng, Q. Zhou, and J. L. Yang. “Improvement of crashworthiness behaviour for simplified structural models of aircraft fuselage”. In: *International Journal of Crashworthiness* 14 (1 2009). p.83-97. ISSN: 13588265. DOI: 10.1080/13588260802517360.

[34] S. Heimbs, M. Hoffmann, M. Waimer, S. Schmeer, and J. Blaurock. “Dynamic testing and modelling of composite fuselage frames and fasteners for aircraft crash simulations”. In: *International Journal of Crashworthiness* 18 (4 2013). p.406-422. ISSN: 13588265. DOI: 10.1080/13588265.2013.801294.

[35] Z. Xianfei, F. Yunwen, X. Xiaofeng, and Q. Qiang. “Evaluate the crashworthiness response of an aircraft fuselage section with luggage contained in the cargo hold”. In: *International Journal of Crashworthiness* 22 (4 2017). p.347-364. ISSN: 17542111. DOI: 10.1080/13588265.2016.1258957.

[36] C. Bisagni, G. Di Pietro, L. Fraschini, and D. Terletti. “Progressive crushing of fiber-reinforced composite structural components of a Formula One racing car”. In: *Composite Structures* 68 (4 2005). p.491-503. ISSN: 02638223. DOI: 10.1016/j.compstruct.2004.04.015.

[37] C. Bisagni. “Experimental investigation of the collapse modes and energy absorption characteristics of composite tubes”. In: *International Journal of Crashworthiness* 14 (4 2009). p.365-378. ISSN: 13588265. DOI: 10.1080/13588260902792954.

[38] M.B. Woodson, E.R. Johnson, and R.T. Haftka. “Optimal design of composite fuselage frames for crashworthiness”. In: *International Journal of Crashworthiness* 1 (4 1996). p.369-380. ISSN: 17542111. DOI: 10.1533/cras.1996.0027.

[39] H.G. Kim, S.C. Kim, and S.J. Kim. “Optimisation of rotorcraft fuel tank for crashworthiness based on a neural network”. In: *International Journal of Crashworthiness* 21 (3 2016). p.242-251. ISSN: 17542111. DOI: 10.1080/13588265.2016.1165447.

[40] L. Lanzi, C. Bisagni, and S. Ricci. “Neural network systems to reproduce crash behavior of structural components”. In: *Computers and Structures* 82 (1 2004). p.93-108. ISSN: 00457949. DOI: 10.1016/j.compstruc.2003.06.001.

[41] C. Bisagni, L. Lanzi, and S. Ricci. “Optimization of helicopter subfloor components under crashworthiness requirements using neural networks”. In: *Journal of Aircraft* 39 (2 2002). p.296-304. ISSN: 15333868. DOI: 10.2514/2.2927.

[42] J. Zheng, J. Xiang, Z. Luo, and Y. Ren. “Crashworthiness design of transport aircraft subfloor using polymer foams”. In: *International Journal of Crashworthiness* 16 (4 2011). p.375-383. ISSN: 13588265. DOI: 10.1080/13588265.2011.593979.

[43] Y. Ren, J. Xiang, J. Zheng, and Z. Luo. “Crashworthiness analysis of aircraft fuselage with sine-wave beam structure”. In: *Chinese Journal of Aeronautics* 29 (2 2016). p.403-410. ISSN: 10009361. DOI: 10.1016/j.cja.2016.02.002.

[44] C. Bisagni and R. Vescovini. “Fast tool for buckling analysis and optimization of stiffened panels”. In: *Journal of Aircraft* 46 (6 2009). p.2041-2053. ISSN: 15333868. DOI: 10.2514/1.43396.

[45] R. Vescovini and C. Bisagni. “Buckling analysis and optimization of stiffened composite flat and curved panels”. In: *AIAA Journal* 50 (4 2012). p.904-915. ISSN: 00011452. DOI: 10.2514/1.J051356.

[46] S.F. Pitton, S. Ricci, and C. Bisagni. “Buckling optimization of variable stiffness cylindrical shells through artificial intelligence techniques”. In: *Composite Structures* 230 (2019). p.1-9. ISSN: 02638223. DOI: 10.1016/j.compstruct.2019.111513.

[47] L. Lanzi and C. Bisagni. “Minimum weight optimization of composite stiffened panels using neural networks”. In: p.1-11. 2003.

[48] C.A. Soto. “Structural topology optimization for crashworthiness”. In: *International Journal of Crashworthiness* 9 (3 2004). p.277-283. ISSN: 13588265. DOI: 10.1533/ijcr.2004.0288.

[49] *Standard Test Method for Tensile Properties of Polymer Matrix Composite Materials 1*. p.1-13. ASTM International, 2008. URL: www.astm.org,.

[50] Aalco Metals Ltd. *Aluminium Alloy 6061-T6 Extrusions, Datasheet*. Tech. rep. Published on-line. 2020.

[51] Oak Ridge National Laboratory. *Crashworthiness of carbon fiber composites: University of Utah’s 46B and 47B tests published data*. https://energy.ornl.gov/CFCrush/rate_tests/rate_tests.cgi.

[52] “Stainless Steel Grade Datasheets”. In: *Atlas Steels - Technical Department* (2013). p.1-57.

[53] A. Matzenmiller, J. Lubliner, and R. L. Taylor. “A constitutive model for anisotropic damage in fiber-composites”. In: *Mechanics of Materials* 20 (2 1995). p.125-152. ISSN: 01676636. DOI: 10.1016/0167-6636(94)00053-0.

[54] N. Stander, A. Basudhar, W. Roux, K. Liebold, Dipl-Math T. Eggleston, T. Goel, and K. Craig. *LS-OPT ® User’s Manual: A DESIGN OPTIMIZATION AND PROBABILISTIC ANALYSIS TOOL FOR THE ENGINEERING ANALYST*. Tech. rep. 2020. URL: www.lstc.com.

[55] E.G. Baquela and A.C. Olivera. “A novel hybrid multi-objective metamodel-based evolutionary optimization algorithm”. In: *Operations Research Perspectives* 6 (2019). Published on-line, p.1-14. ISSN: 22147160. DOI: 10.1016/j.orp.2019.100098.

[56] A. Basudhar. *Efficient Global Optimization Using LS-OPT and its Parallelization*. 2017.

[57] C. Kassapoglou. *Design and Analysis of Composite Structures: With Applications to Aerospace Structures: Second Edition*. DOI: 10.1002/9781118536933.

[58] S. Boria, J. Obradovic, and G. Belingardi. “Experimental and numerical investigations of the impact behaviour of composite frontal crash structures”. In: *Composites Part B: Engineering* 79 (2015). p.20-27. ISSN: 13598368. DOI: 10.1016/j.compositesb.2015.04.016.